



HAL
open science

Gaussian-state approaches to quantum spin systems away from equilibrium

Raphaël Menu

► **To cite this version:**

Raphaël Menu. Gaussian-state approaches to quantum spin systems away from equilibrium. Condensed Matter [cond-mat]. Université de Lyon, 2020. English. NNT : 2020LYSEN036 . tel-03099280

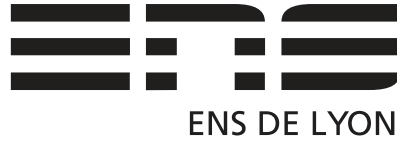
HAL Id: tel-03099280

<https://theses.hal.science/tel-03099280>

Submitted on 6 Jan 2021

HAL is a multi-disciplinary open access archive for the deposit and dissemination of scientific research documents, whether they are published or not. The documents may come from teaching and research institutions in France or abroad, or from public or private research centers.

L'archive ouverte pluridisciplinaire **HAL**, est destinée au dépôt et à la diffusion de documents scientifiques de niveau recherche, publiés ou non, émanant des établissements d'enseignement et de recherche français ou étrangers, des laboratoires publics ou privés.



Numéro National de Thèse : 2020LYSEN036

THÈSE DE DOCTORAT DE L'UNIVERSITÉ DE LYON

opérée par

l'École Normale Supérieure de Lyon

**École Doctorale N°52
École Doctorale de Physique et Astrophysique de Lyon**

Discipline : Physique

Soutenue publiquement le 07/09/2020 par :

Raphaël MENU

**Gaussian-state approaches to quantum spin
systems away from equilibrium**

**Approches gaussiennes aux systèmes de spins quantiques
hors-équilibre**

Devant le jury composé de :

GAMBASSI, Andrea	Professeur des universités	SISSA	Rapporteur
LAHAYE, Thierry	CR CNRS	Institut d'Optique	Examinateur
ROSCILDE, Tommaso	Maître de conférences	ENS de Lyon	Directeur
SANCHEZ-PALENCIA, Laurent	DR CNRS	École Polytechnique	Rapporteur
SANTOS, Luis	Professeur des universités	Leibniz Universität	Examinateur
SAVARY, Lucile	CR CNRS	ENS de Lyon	Examinatrice
VIGNOLO, Patrizia	Professeure des universités	Université Côte d'Azur	Examinatrice

*” Chaque soir, espérant des lendemains épiques,
L’azur phosphorescent de la mer des Tropiques
Enchantait leur sommeil d’un mirage doré ;*

*Ou, penchés à l’avant des blanches caravelles,
Ils regardaient monter en un ciel ignoré
Du fond de l’Océan des étoiles nouvelles.”*

José Maria de Heredia, ”Les Conquérrants”, *Les Trophés*

Résumé

Approches gaussiennes aux systèmes de spins quantiques hors-équilibre.

Que se passe-t-il quand un système quantique à N corps est brutalement amené loin de son état d'équilibre ? Vers quelle sorte d'état relaxe-t-il et quelle information peut-on extraire de sa dynamique ? Fournir des réponses à ces questions est un problème difficile qui a suscité l'intérêt de toute une communauté de physiciens. Cependant, le coût numérique important requis pour étudier le comportement de ces systèmes, en particulier pour de grandes tailles, a motivé le développement de méthodes numériques et théoriques de pointe.

Cette thèse s'inscrit dans la continuité de ces efforts en proposant un ensemble de méthodes basées sur une représentation en termes d'une théorie de champs Gaussiens afin d'étudier l'évolution des systèmes de spins. Plus particulièrement, ces méthodes sont appliquées à plusieurs modèles inspirés par les expériences d'atomes froids simulant le comportement de systèmes de spins avec un accent particulier sur l'étude des phénomènes de localisation. Cette thèse présente donc des résultats mettant en évidence l'émergence de la localisation dans des systèmes sans désordre par un effet d'interférence appelé cage d'Aharonov-Bohm; ainsi qu'une dynamique explorant un riche spectre allant de la diffusion balistique à la localisation, en passant par la diffusion anormale, cela dans un modèle d'Ising quantique avec désordre géométrique — ce dernier exemple présente un scénario bien plus riche que celui offert par la dynamique des particules libres dans un milieu désordonné. Enfin, nous avons exploré la possibilité pour les approches gaussiennes de décrire la dynamique de systèmes interagissant et leur relaxation vers des états thermiques.

Mots-clés : Dynamique de spin, intrication, localisation, atomes de Rydberg .

Abstract

Gaussian-state approaches to quantum spin systems away from equilibrium

What happens when a quantum many-body system is brutally driven away from equilibrium ? Toward which kind of states does it relax and what information can one extract from the resulting dynamics ? Providing answers to these questions is a challenging problem that spurred the interest of a whole community of physicists. However, the numerical cost required to investigate the behaviour of these systems, particularly for large system sizes, motivated the development of cutting-edge numerical and theoretical techniques.

This thesis aims at contributing to these efforts by proposing a set of methods based on a representation of the systems in terms of a Gaussian field theory, with the purpose of studying the evolution of spin systems. More specifically, these methods are applied to several models inspired by cold-atoms experiments simulating the behaviour of spin systems, with a stress on the study of localization phenomena. Therefore, this thesis highlights the emergence of localization in systems devoid of disorder due to an interference effect, the so-called Aharonov-Bohm caging; as well as a geometrically disordered quantum Ising model displaying a dynamics exploring a rich spectrum ranging from ballistic diffusion to anomalous diffusion, and then localization - this last example offers a scenario richer than the one exhibited by the dynamics of free particles in a disordered medium. Finally, we explored the possibility for Gaussian approaches to describe the dynamics of interacting systems and their relaxation toward thermal states.

Keywords: Spin dynamics, entanglement, localization, Rydberg atoms.

Acknowledgments

*"De ces biens passagers que l'on goûte à demi,
Le meilleur qui nous reste est un ancien ami.*

Alfred de Musset, "À M. V.H.", *Poésies nouvelles*

On attribue à Bernard de Chartres la maxime selon laquelle tout penseur, philosophe ou scientifique n'est rien de plus qu'un nain perché sur les épaules de géants, qu'il est tributaire des travaux de ses prédécesseurs et doit en éprouver une certaine humilité. Ce que la métaphore omet de dire en revanche, c'est comment le nain s'est retrouvé là-haut. Les nains les moins modestes affirmeront qu'il s'y sont hissé seuls, mon opinion sur la question est qu'on les a aidé. Avant d'assommer le lecteur à grands coups d'équations et de considérations physiques, le nabot que je suis aimerait donc remercier comme il se doit toutes les personnes qui lui ont fait la courte échelle et lui ont permis de voir un peu plus loin que son étroit horizon.

Mes remerciements vont en premier lieux au géant sur les épaules duquel je me tiens directement (même s'il déclinera sans doute le titre de géant), à savoir mon directeur de thèse, Tommaso Roscilde. Merci infiniment d'avoir été aussi présent pendant ces trois années, mais aussi pour avoir été d'un enthousiasme et d'une énergie à toute épreuve, et -on ne va pas se le cacher- d'avoir été parfois optimiste pour deux. J'ai énormément appris grâce à toi, aussi bien sur la physique des systèmes à N -corps que ce que cela signifie d'être physicien. Je ne pouvais rêver d'avoir un meilleur mentor.

De manière moins directe, mais tout aussi significative, je souhaiterais remercier les autres membres, passés ou présents, de notre petite équipe ; tous ont largement nourri cette thèse par leurs discussions stimulantes. Pêle-mêle, merci donc à Fabio Mezzacapo, Tommaso Comparin, Leonardo Benini, Piero Naldesi, Irénée Frérot et Jérôme Thibaut. Un grand merci également aux différents chercheurs avec qui j'ai eu la chance de discuter de mes travaux, que ce soit à Lyon, aux Houches ou ailleurs : Jean Decamp, Titus Franz, Philipp Hauke, Louis-Paul Henry, Jennifer Koch, Bruno Laburthe-Tolra, Nicolas Macé, Giovanna Morigi,

Adam Rançon, Johannes Schachenmayer, Shraddha Sharma, Hugo Théveniaut, Steven Thomson, Laurent Vernac, Wouter Verstraelen, Louis Villa et Yong Xia.

Et bien évidemment, je remercie chaleureusement tous les membres du jury pour avoir assisté à cette soutenance très spéciale : Thierry Lahaye, Luis Santos, Lucile Savary et Patrizia Vignolo et en particulier Andrea Gambassi et Laurent Sanchez-Palencia pour avoir relu ce manuscrit et l'avoir enrichi de leurs suggestions. Un grand merci également à Thierry Dauxois et Jean-Christophe Géminard pour avoir contribué à faire du Laboratoire de Physique de l'ENS Lyon un environnement accueillant et propice à la recherche. Merci aussi à l'équipe de choc des secrétaires du laboratoire, toujours disponibles et toujours au top.

La vie d'un doctorant, hélas -ou heureusement, c'est à l'appréciation de chacune se résume pas seulement à la science. Et si j'ai pu mener cette thèse à bien, c'est en grande partie grâce au soutien de mes proches et collègues. J'en profite donc pour remercier mes collègues de bureau, à commencer par l'inénarrable Jérôme Thibaut. En un peu plus d'un an et demie de bureau commun, on a eu plus que le temps de refaire le monde, commenter l'actualité, philosopher sur l'existence, et à l'occasion parler de physique. Pour ces excellents moments, je ne peux qu'être reconnaissant. J'en profite également pour m'excuser platement auprès de Lavi Upreti, Dario Lucente et Thibaut Louvet qui ont subi nos élucubrations avec un stoïcisme qui force l'admiration, et les remercier de leur patience. Je remercie également Léo Mangeolle qui s'est avéré être un voisin de bureau très compatissant face aux misères de la correction de copies. Puisqu'il était question d'importuner d'honnêtes doctorants durant leur travail, je m'excuse également auprès des collègues de bureau de Barbara ; les pauvres ont dû subir plus d'une fois mes visites intempestives. Quant à Barbara, elle a tous mes remerciements pour m'avoir initié à la dégustation du thé, et pour en avoir bu des litres en ma compagnie.

La solidarité entre doctorants étant la pierre angulaire d'une rédaction qui se passe bien, je rends hommage à mes camarades galériens Laura et Lucas qui ont partagé avec moi la joie de rédiger durant le confinement. Merci également à Richard, l'homme qui murmure à l'oreille de L^AT_EX, pour ses coups de pouce à l'occasion, mais aussi pour les compliments dont il n'est jamais avare. Enfin, on ne peut dignement faire une thèse au Laboratoire de Physique de l'ENS Lyon sans remercier tous les membres du groupe "40 c'est 40" ainsi que les indémodables buveurs de cafés, qu'ils soient passés et présents. Ainsi donc, merci à Alex, Alizée, Ariane, Arnaud, Bastien, Charles-Édouard, David, Éric, Géraldine, Hélène, Jérémie, Lauren, Pauline, Samuel, Simon, Thomas, Timothée, Valentin, Vincent, Yannick, ainsi qu'à son Altesse Thibaut, à l'occasion.

Mais puisqu'il y a aussi une vie hors de l'ENS, je dois aussi remercier ceux qui évoluent (principalement) par-delà ses murs. Je commencerai donc par exprimer ma gratitude envers tous les membres de France Shotokan Lyon, et en particulier Anne-Laure et Helen qui m'ont transmis le virus du karaté, une maladie qui dure toute la vie. Merci pour les katas, kions et kumites, je ne pense pas qu'on ait inventé à ce jour meilleur moyen de se vider la tête, et merci d'avoir été un précieux soutien lors de la dernière ligne droite de la rédaction.

J'en profite aussi pour faire un clin d'œil à tous mes proches qui n'ont pas pu se déplacer pour assister à ma soutenance pour les raisons que tout le monde connaît, mais qui ne se sont pas privé pour autant d'abondamment la commenter en aparté.

Enfin pour conclure ces très longs remerciements, je tiens à exprimer toute ma gratitude et mon affection à ma famille, qui bien que n'ayant jamais rien compris à ce que je faisais de ma vie n'a jamais cessé de me soutenir. Et si je peux me permettre, je tiens à remercier en particulier ma mère d'avoir eu la bonne idée de me mettre devant "C'est pas Sorcier" sur France 3 quand j'étais petit. Je crois que c'est là que tout a commencé.

Contents

Résumé	iii
Abstract	v
Acknowledgments	vii
Introduction	1
1 Quantum systems out of equilibrium	5
1.1 Of entanglement in many-body physics	5
1.1.1 A brief history of entanglement	5
1.1.2 Many-body dynamics and correlations	8
1.1.3 Thermalization of quantum systems	11
1.1.4 Rydberg atom simulators	14
1.2 The challenge of quantum complexity	18
1.2.1 Exact diagonalization and beyond	19
1.2.2 Variational approaches	20
1.2.3 Semi-classical methods	22
2 Gaussian approaches for quantum spin systems	25
2.1 Linear spin-wave theory	25
2.1.1 Quantum-field corrections to mean-field	25
2.1.2 Spin-boson projection	26
2.1.3 Bogoliubov transformation	28
2.1.4 Bosonic Gaussian states	30
2.2 The treatment of non-linearity : the Gaussian Ansätze	33
2.2.1 Modified spin-wave theory	33
2.2.2 Dynamical Gaussian Ansatz	35
2.3 Fermionic Gaussian states	37
2.3.1 Spin-fermion projection	37
2.3.2 Fermionic Gaussian Ansatz	38
2.4 Conclusion	40
3 Dynamics of flat-band systems	41
3.1 Flat-bands of excitations	41
3.1.1 Band flatness and Aharonov-Bohm caging	41
3.1.2 From models to experiments	43
3.2 Geometric frustration : the triangular lattice	44

3.2.1	Ground-state degeneracy	44
3.2.2	Spectral properties	47
3.2.3	Quench dynamics	50
3.2.4	Quench spectroscopy	53
3.3	Aharonov-Bohm caging : Lieb and Kagome lattices	55
3.3.1	High-energy quench protocols	55
3.3.2	Emergence of caged states	57
3.3.3	Effects of van der Waals interactions	59
3.4	Conclusions	60
4	Anomalous diffusion in positionally disordered quantum spin systems	63
4.1	Disordered spin systems	63
4.1.1	Ground-state localization and localization of the excitations	63
4.1.2	Positionally disordered atoms arrays	64
4.1.3	Ground-state properties : dirty ferromagnetism	66
4.1.4	Probability distribution of the disordered couplings	67
4.2	Spectral properties and localization	69
4.2.1	Inverse participation ratio	69
4.2.2	Scaling of the inverse participation ratio	70
4.2.3	Dynamical structure factor	71
4.2.4	Multifractal eigenmodes	72
4.3	Anomalous dynamics and localization	74
4.3.1	Entanglement entropy	74
4.3.2	Correlation functions	76
4.3.3	Probing multifractality via quench dynamics	78
4.4	Conclusions	80
5	Gaussian Ansatz approaches to non-linear spin dynamics	81
5.1	Interacting spin systems	81
5.1.1	Motivations	81
5.1.2	Non-linear spin-wave Hamiltonian	82
5.2	Transverse-field Ising chain	83
5.2.1	Fermionic and bosonic images of dynamics	83
5.2.2	Quench dynamics of the transverse magnetization	84
5.2.3	Spin-spin correlation functions	87
5.2.4	Entanglement entropy	88
5.3	Transverse-field Ising model on the square lattice	89
5.3.1	From the chain to the square lattice	89
5.3.2	Quenching from the field-polarized state	91
5.3.3	Quenching from the ferromagnetic state	93
6	Conclusions and outlooks	97
	Bibliography	103
A	Linear spin-wave theory of the transverse field Ising model	113

B	Modified spin-wave theory	115
C	Quench spectroscopy	119
D	Gaussian Ansatz approach of the transverse field Ising model	123
	D.1 Quenching from the field-polarized state	123
	D.2 Quenching from the ferromagnetic state	124

Introduction

*”Nous voulons, tant ce feu nous brûle le cerveau,
Plonger au fond du gouffre, Enfer ou Ciel, qu’importe ?
Au fond de l’Inconnu pour trouver du nouveau !”*

Charles Baudelaire, ”Le Voyage”, *Les Fleurs du Mal*

Studying and understanding the behaviour of quantum many-body systems is a challenging problem of prime interest, both for expanding the fundamental knowledge of this domain of physics where complex and exotic states of matter often emerge, but also to open new perspectives in technological development. However, gaining insights onto the behaviour of these systems requires formidable efforts, as said theoretical approaches are often missing to get quantitative predictions for quantum many-body systems. A general strategy in modern physics amounts to rely on numerical methods, but the quantum nature of the models at hand and the calculation capacities of classical computer limit fundamentally these approaches to small systems. Quantum simulation aim at overcoming these difficulties by implementing many-body quantum physics directly into the hardware of a quantum machine [36].

During the past few decades, the development of experimental techniques in atomic physics enabled the cooling and trapping of atoms in order to simulate the physics of bosonic or fermionic particle lattice models. More recently quantum simulation transcended the area of atomic physics to inspire the engineering of simulators in photonic and polaritonic platforms, in superconducting circuits etc [40]. In particular, progress in the individual trapping of particles and the coupling of their internal degrees of freedom led to implementation of spin systems in controlled geometries, thus offering new possibilities for the simulation of quantum magnetism.

This thesis proposes an approximate numerical approach to many-body dynamics based on a Gaussian Ansatz for the many-body state, and applies it to several implementations of quantum spin Hamiltonians in different geometries and dimensions, all relevant for a realization in a class of quantum simulators

for spin systems. We also propose realistic tools to probe the exotic dynamical properties exhibited by these models. Our discussion will be structured in six chapters :

1. In the first chapter, we will review the specificities and phenomenology of quantum many-body dynamics, how it leads to the production of entanglement and the establishment of correlations between subparts of the whole system. The characterization of the asymptotic state after relaxation will also be discussed, distinguishing between the generic situation in which such a state has the same local features as those of a thermal equilibrium ensemble, and the special cases in which thermalization is instead escaped. After reviewing the different experimental approaches available in atomic physics for the description of many-body physics (with a special focus on Rydberg-atom simulators), we will delve into the spectrum of possible numerical methods developed for the study of many-body dynamics and discuss briefly their capabilities and limitations.
2. The second chapter is dedicated to present the theoretical framework of the Gaussian Ansatz, first in its linearized bosonic formulation to spin-wave theory, before extending it to cases where non-linearities play a more prominent role. We shall discuss the application of these approaches both to thermal equilibrium as well as to out-of-equilibrium physics. We will conclude this chapter by also providing a complementary image of Gaussian states, namely the fermionic formulation of the Gaussian Ansatz.
3. The third chapter focuses on the application of linear spin-wave theory to the physics of flat-band systems realized on quantum spin models relevant for Rydberg-atom simulators [63]. In particular, we propose two protocols for preparing the quantum state away from equilibrium, each providing a different perspective on the dynamics of elementary excitations, their spectral properties and spatial structure. We used these protocols to highlight localization effects in systems with flat bands of excitations, and discriminate between the different mechanisms resulting into band flatness.
4. A second application of linear spin-wave theory is presented in the fourth chapter, where we will discuss of the widely different effects of disorder on the low-temperature thermodynamics and dynamics of a positionally disordered spin system [64]. We offer a scaling analysis suggesting that the spectrum experiences at finite disorder a transition to localization that is decoupled from the ground-state properties and we offer evidence that, at intermediate values of disorder the eigenmodes in the band center possess a multifractal structure, resulting in anomalous diffusion in the non-equilibrium dynamics. Moreover, we show that the multifractal properties of these eigenmodes can be directly probed by analyzing the magnetization profile of the system at long times.
5. The fifth chapter of this thesis tackles the question of the extension of the Gaussian Ansatz to systems where non-linearities and interactions become more prominent. We will benchmark this approach in the case of

the transverse-field Ising chain, which has the two-fold advantage of being integrable and relevant for an experimental implementation in different quantum simulation platforms. We will then lead this same study in the two-dimensional case of the square lattice, for which a description in terms of an integrable model is not available, and we will compare these results with quantum Monte Carlo simulations for the steady-state regime, and with other numerical approaches for the transient dynamics.

6. Finally, the sixth chapter will conclude this thesis by summarizing our findings and discussing further applications of the Gaussian-state approaches to dynamics, both to answer questions left open in the previous chapters and to explore new models and physical effects.

Quantum systems out of equilibrium

*”One foot he centered, and the other turned
Round through the vast profundity obscure
And said, thus farr extend, thus farr thy bounds,
This be thy just Circumference, O World.”*

John Milton, *Paradise Lost*

1.1 Of entanglement in many-body physics

1.1.1 A brief history of entanglement

The early 20th century was a pivotal moment in the history of modern physics as it witnessed two major breakthroughs in the understanding of Nature: one was Einstein’s theories of relativity, the other was quantum mechanics. The birth of this second theory results from the joint efforts of several physicists trying to provide answers to unsolved questions such as the origins of black-body radiation or the stability of matter. Their work led to the development of a very powerful and predictive theoretical framework, which succesfully answered the questions left open by classical physics, but also unveiled counterintuitive behaviours of matter at microscopic scales. Indeed, quantum theory in general cannot predict the outcome of measurements with certainty: contrarily to the classical view on the game of head or tail, where the outcome is decided before the measurement due to an underlying deterministic dynamics, for quantum mechanics the result would be left undecided until a measurement is performed on the coin. Therefore, the state of the coin prior to measurement is described as a superposition of both head and tail, and this description holds the actual nature of the state, leaving no room for any deterministic picture.

Unconvinced by this interpretation as it deeply mismatched with his philosophical beliefs, Einstein, along with Podolsky and Rosen (EPR), tried to demon-

strate in a now famous article [32] that the quantum theory in its standard (Copenhagen) interpretation was incomplete. For this purpose, EPR designed a thought experiment where two particles are simultaneously emitted and possess special correlations such that from measuring the state of one of the particles, one can instantaneously deduce the state of the other, regardless of the distance separating the two particles. An example of a state exhibiting this property is the singlet state of two spins- $\frac{1}{2}$,

$$|\psi\rangle = \frac{1}{\sqrt{2}} (|\uparrow\rangle_1 \otimes |\downarrow\rangle_2 - |\downarrow\rangle_1 \otimes |\uparrow\rangle_2). \quad (1.1)$$

The measurement of the spin labeled as 1 then leads to two outcomes: either it is up-oriented and then the partner spin is down-oriented, or the contrary happens.

According to EPR, the perfect correlations among measurements of different spin components of spins 1 and 2 contradict the fact that such components are incompatible observables in quantum mechanics, because EPR assume the property of *local realism*, namely the fact that a measurement on spin 1 cannot affect the state of spin 2. Indeed, according to this point of view, predicting with certainty e.g. the x - or y -components of spin 1 by measurement the same components of spin 2 attributes to the latter two *elements of reality* which are nonetheless incompatible with quantum mechanics. The conclusion of EPR is that the quantum mechanical description of many-particle systems is incomplete, and it requires the introduction of further *hidden variables* to be compatible with local realism.

The objections raised by EPR to the Copenhagen interpretation remained confined to the philosophical ground until Bell showed that the expectation values of a quantum theory with local hidden variables are bounded and obey inequalities, therefore offering the possibility to experimentally test the existence of hidden variables. Though the experimental demonstration of the violation of Bell's inequalities by Aspect [7] ultimately proved wrong the hidden variables argument, the work of EPR was pioneering in the sense that it outlined a remarkable property of quantum physics, namely the possibility for a collection of quantum objects to develop correlations escaping any classical description. In other words, quantum many-body systems cannot be described as the sum of all their parts, but instead as whole coherent entities which remain as such however distant their components may be from each other. Therefore, measuring the state of a subpart impacts the system as a whole. This concept was dubbed *entanglement* by Erwin Schrödinger in a seminal article of 1935 [84], where he described it as the most intrinsically quantum feature a many-body system can exhibit.

Entanglement of pure states can be defined mathematically by stating that, for a bipartite system $S = A + B$, an entangled state cannot be decomposed as a tensor product $|\Psi\rangle \neq |\psi_A\rangle \otimes |\psi_B\rangle$, where A and B label the two subparts of the system. Consequently, entangled states admit a more general expression, this time in terms of a coherent superposition of factorized states

$$|\Psi\rangle = \sum_n \sqrt{p_n} |\psi_A^{(n)}\rangle \otimes |\psi_B^{(n)}\rangle, \quad (1.2)$$

where $\{|\psi_i^{(n)}\rangle\}$ are orthonormal vectors from the Hilbert space of subsystem $i = A, B$, while $\sqrt{p_n}$ are positive real numbers. The formula given in Eq. (1.2) is the so-called Schmidt decomposition of the state, indicating the presence of entanglement if at least two of the Schmidt coefficients p_n are non-zero.

A way to quantify entanglement is to probe the Shannon entropy of the distribution of the normalized probabilities p_n , $E[|\Psi\rangle] = -\sum_n p_n \ln p_n$, called entanglement entropy. The latter admits an upper bound $\ln D_{\min}$, where $D_{\min} = \min(D_A, D_B)$, D_i being the Hilbert space dimension of subsystem i . Let us consider an arbitrary state of the $(D_A \times D_B)$ -dimensional joint Hilbert space for the whole system - namely

$$|\Psi\rangle = \sum_{n=1}^{D_A} \sum_{m=1}^{D_B} c_{nm} |\alpha^{(n)}\rangle \otimes |\beta^{(m)}\rangle \quad (1.3)$$

where $\{|\alpha^{(n)}\rangle\}$ and $\{|\beta^{(m)}\rangle\}$ are orthonormal bases for respectively subsystems A and B , while c_{nm} are arbitrary complex coefficients. It has been shown by Page [72] that such a state exhibits on average an entanglement entropy very close to its upper bound $\ln D_{\min}$. This points to a fundamental difference between factorized and entangled states: while the former are described by $D_A + D_B$ coefficients, specifying the states of the subparts $|\psi_A\rangle$ and $|\psi_B\rangle$, the characterization of the latter generically requires $D_A \times D_B$ coefficients, which must be statistically independent for the subsystems to be arbitrarily entangled.

Extending the previous discussion on the structure of bipartite states to $N > 2$ parties, the description of factorized states

$$|\Psi\rangle = \bigotimes_{i=1}^N |\psi_i\rangle \quad (1.4)$$

requires ND coefficients, where D is the Hilbert space dimension for each of the parties (assumed to be uniform for the sake of simplicity). On the other hand, a generic state of the D^N dimensional joint Hilbert space can always be written in the form given by Eq. (1.3), where $\{|\alpha^{(n)}\rangle\}$ are for instance the states of the first $N/2$ parties and $\{|\beta^{(m)}\rangle\}$ specify the states of the $N/2$ remaining ones. In this case $D_A = D_B = D^{N/2}$, and the state is parametrized by $D_A \times D_B = D^N$ coefficients, namely it contains an amount of information scaling exponentially with the system size. This difference in the quantity of information encoded in the state suggests that factorized states live in a restricted area of the Hilbert space, while entangled ones are free to span it in its entirety, leading to the conclusion that quantum many-body states hold more generality and exhibit richer variety of behaviours than factorized states could possibly grasp. Solid-state physics offer several examples of entangled states, such as Fermi liquids, superconductors or quantum spin liquids, yet the degree of entanglement of these states does

not compare with the highly entangled ones that can be produced by artificial quantum many-body systems (quantum computers, quantum simulators) away from equilibrium, as we will discuss in the following.

1.1.2 Many-body dynamics and correlations

Placing entanglement at the heart of the physics of quantum many-body systems naturally gives rise to new questions regarding its behaviour at and away from equilibrium: given an initial state and a many-body Hamiltonian \mathcal{H} governing its unitary evolution, how does its entanglement evolve in time? Does it relax toward an equilibrium value and, if so, how can it be characterized?

The choice of the initial state fundamentally dictates the portion of the Hamiltonian spectrum which will be relevant for the subsequent dynamics; however for the moment we will only assume that the initial state $|\Psi_0\rangle$ is not an eigenstate of the Hamiltonian, namely $\hat{\mathcal{H}}|\Psi_0\rangle \neq \lambda|\Psi_0\rangle$. Indeed, under the assumption that the initial state is actually an eigenstate of the Hamiltonian, the unitary dynamics only results in the state picking up a global phase which leaves the expectation value of observables untouched. An alternative point of view consists in treating the initial state as an eigenstate of some Hamiltonian $\hat{\mathcal{H}}_i$, and imagining that at time $t = 0^+$ some parameters of the Hamiltonian are suddenly shifted in order to bring $\hat{\mathcal{H}}_i$ toward $\hat{\mathcal{H}}_f = \hat{\mathcal{H}}$ for which $|\Psi_0\rangle$ is no longer an eigenstate, with the aforementioned consequences on dynamics. Systems pushed away from their equilibrium states in such a manner are said to undergo a *quantum quench*.

We shall now provide some insights on the dynamical behaviour one should expect to observe. The joint work of Lieb and Robinson [58] in 1972 disclosed that, in systems with short-ranged interactions, the propagation of information, namely the reorganization of correlations in the quantum state under the effect of the Hamiltonian dynamics, is constrained by the so-called Lieb-Robinson bounds [19]. For two observables \hat{A} and \hat{B} with a finite norm and acting on two finite disconnected spatial regions of the system, taken at two different times, the norm $\|\cdot\|$ of their commutator is bounded as

$$\|[\hat{A}(t), \hat{B}(0)]\| \leq c \|\hat{A}\| \|\hat{B}\| \min(|\hat{A}|, |\hat{B}|) e^{-(d(A,B) - v_{\text{LR}}|t|)/\xi}, \quad (1.5)$$

where $d(A, B)$ stands for the distance between the supports of \hat{A} and \hat{B} , while $|\hat{A}|$ and $|\hat{B}|$ are the size of their respective supports, and c , ξ and v_{LR} are positive constants. In other words, the Lieb-Robinson bound states that the propagation of information is exponentially suppressed outside of the boundaries of a *light cone*, whose aperture is dictated by a characteristic velocity v_{LR} named Lieb-Robinson velocity. As the emergent causality enforced by the Lieb-Robinson bounds constraints the dynamics of any form of correlation between two points of a system, one should expect the appearance of light-cone structures in microscopic systems when one looks at correlation functions, as shown in Fig. 1.1 (a) for the correlations among the z -spin components in a spin chain described by the XX model,

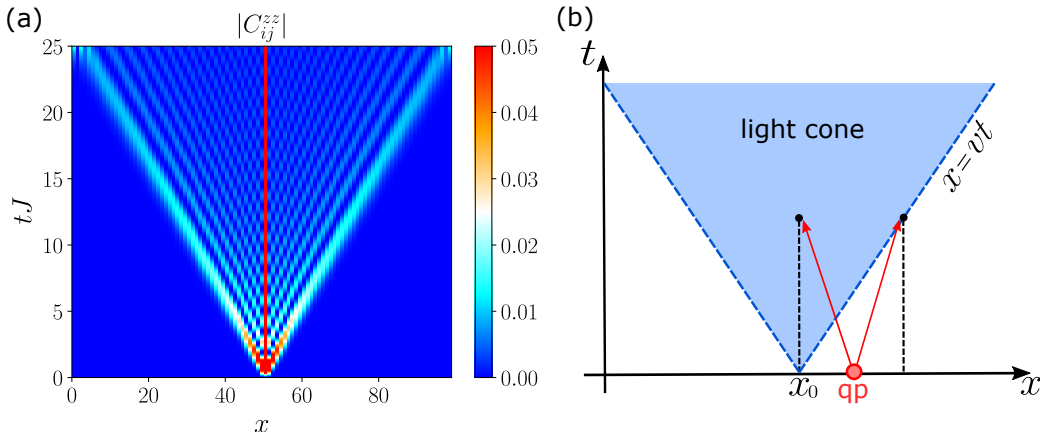


Figure 1.1: Light cone effect - (a) shows the time evolution of $\langle S_{x_0}^z S_{x_0+x}^z \rangle$ correlation function of an XX spin chain of $L = 100$ following a quench from the Néel state along the z axis $|\uparrow\downarrow\uparrow\downarrow\dots\rangle$. (b) shows in a schematic way the emergence of the light-cone effect from the Cardy-Calabrese image.

$$\hat{\mathcal{H}} = -J \sum_i [\hat{S}_i^x \hat{S}_{i+1}^x + \hat{S}_i^y \hat{S}_{i+1}^y], \quad (1.6)$$

where \hat{S}_i^α ($\alpha = x, y, z$) are $S = 1/2$ spin operators at site i , mappable onto free fermions (quasiparticles) [56]. The observation of light-cone structures of correlations motivated some seminal experimental studies, highlighting the light-cone effect in cold-atom simulation of the Bose-Hubbard model [25] or trapped-ions realizations of spin systems [53].

Precious insights into the physical origin of this emerging causality were provided by the work of Calabrese and Cardy [21]. Their interpretation of the light-cone effect relies on a representation of the initial quenched state as a gas of correlated pairs of quasiparticles; their ballistic propagation during the dynamics then results in the linear spreading of correlations as the particles carry information in their wake, as shown in Fig. 1.1(b). The quasiparticle image also enables to make sense of the Lieb-Robinson velocity by relating it to the maximal group velocity of the quasiparticles themselves

$$v_{\text{LR}} = 2 \max_{\mathbf{k} \in \text{BZ}} |\nabla_{\mathbf{k}} \omega_{\mathbf{k}}|, \quad (1.7)$$

where $\omega_{\mathbf{k}}$ is the quasiparticle dispersion relation. The factor of 2 in this expression is due to the fact that correlations between two points are established when they are reached by the fastest quasiparticles emitted at the mid point.

The quasiparticle picture provided by Calabrese and Cardy also offers some insights into the behaviour one can expect for the dynamics of entanglement. Provided that quasiparticles act as messengers carrying information and establishing correlations, their propagation should participate to the build-up of entanglement between the different subparts they cross. Therefore, the evolution of entanglement estimators should reflect the dynamics of the quasiparticles that underlies

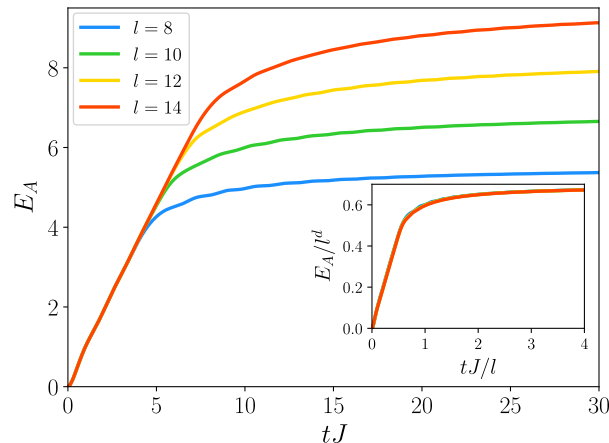


Figure 1.2: Time-evolution and scaling of the entanglement entropy of XX spin chains initialized in the Néel state - the considered subsystems are sections of length l of chains of $L = 10 \times l$ sites. The inset shows the volume-law scaling of entanglement entropy as all curves collapse on a universal one. All calculations are performed with a free fermions approach.

their evolution. For instance the von Neumann entanglement entropy defined for a subsystem A in terms of the reduced density matrix (see previous section)

$$E_A = -\text{Tr} [\hat{\rho}_A \ln \hat{\rho}_A] \quad (1.8)$$

grows linearly with time until it reaches saturation once the quasiparticles have explored the entirety of the subsystem A , and established correlations between all sites. The entanglement entropy dynamics displays therefore a characteristic time which scales linearly with the linear size l_A of the subsystem of interest, namely $t^* = l_A/(2v_{\text{LR}})$, corresponding to the time necessary for the light cone to spread from the center of A to its boundary, covering a distance $l_A/2$. The quasiparticle picture also unravels a second meaningful scaling law : as every site of the subsystem A participate into the correlations with its complement B , the equilibrium entropy scales like the size l_A^d of the considered subsystem, namely it exhibits a so-called *volume law* scaling. These different behaviours and scaling relations are illustrated by Fig. 1.2 in a one-dimensional case ($d = 1$).

The dynamical features that we reviewed up to this point do not survive the introduction of strong disorder and the appearance of Anderson localization [6] in the absence of interactions between quasiparticles. The light-cone structure of correlations for instance breaks down as the propagation of excitations - and consequently information - is suppressed. A direct consequence of localization is then that the amount of entanglement generated by dynamics is much weaker compared to what is observed in clean systems. Moreover, localization also has the more dramatic effect of preventing the system from relaxing towards a state with volume-law scaling of the entanglement entropy. Instead, it exhibits a subextensive growth with the subsystem size l_A , as the only sites able to participate to the exchange of information between the subsystem A and its complement are

localized at their interface. The equilibrium entropy of a subsystem A then scales linearly in the size of its boundaries, and it obeys a so-called *area law* such that $E_A \propto l_A^{d-1}$.

1.1.3 Thermalization of quantum systems

In generic quantum many-body dynamics (not admitting a description in terms of free quasiparticles), at long times the entanglement entropy acquires an extensive nature reminiscent of the extensive character of the thermodynamic entropy of thermal equilibrium. This indeed suggests that individual quantum states may equilibrate so as to admit a local description in terms of the Gibbs ensemble

$$\lim_{t \rightarrow +\infty} \hat{\rho}_A(t) \simeq \frac{1}{Z} e^{-\beta \hat{\mathcal{H}}_A}, \quad (1.9)$$

where the inverse temperature β depends on the energy initially injected in the system by the quench, namely $\langle \Psi_0 | \hat{\mathcal{H}}_A | \Psi_0 \rangle$ and $\hat{\mathcal{H}}_A$ is the Hamiltonian for the degrees of freedom of A only. If indeed such a condition is met, the system is said to have *thermalized*. Indeed if the considered subsystem is small enough compared to the overall system, and yet sufficiently large so that the coupling energy between A and B can be considered as a small term compared to the energy of A , then an effective image consists of viewing the complement B as a thermal bath weakly coupled to A , and establishing thermal equilibrium in A once the correlations between the subsystem and its complement have finally settled.

The description of equilibration in terms of thermalization is however only possible under some general assumptions on the nature of the Hamiltonian eigenstates. In the following, we will explicitly state sufficient conditions essential to a statistical description of equilibrium states, and situations in which these conditions are not met. Let us decompose the initial state of the evolution on the eigenbasis of the evolution Hamiltonian $|\Psi_0\rangle = \sum_n c_n |\psi_n\rangle$, so that the evolved state $|\Psi(t)\rangle$ obtained by the action of the unitary evolution operator $\hat{U}(t) = e^{-it\hat{\mathcal{H}}}$ admits a very simple expression, where the coefficients c_n only acquire a rotating phase factor

$$|\Psi(t)\rangle = \sum_n c_n e^{-i\omega_n t} |\psi_n\rangle, \quad (1.10)$$

with $\omega_n = E_n/\hbar$ and E_n is the eigenenergy corresponding to eigenstate $|\psi_n\rangle$. From the above result, we obtain the expression for the time-evolution of the expectation of any observable \hat{A}

$$\langle \hat{A} \rangle(t) = \sum_{m,n} c_m^* c_n e^{-it(\omega_n - \omega_m)} \langle \psi_m | \hat{A} | \psi_n \rangle. \quad (1.11)$$

The form provided by Equation (1.11) for the expectation value in terms of a sum of oscillating functions suggests a persistent dynamics at all times. Yet the equilibrium value of the observable can be extracted by time averaging the evolution, thus eliminating the oscillations

$$\langle \hat{A} \rangle_{\text{eq}} = \lim_{T \rightarrow +\infty} \frac{1}{T} \int_0^T \langle \hat{A} \rangle(t) dt \quad (1.12)$$

$$= \sum_n |c_n|^2 A_{nn}. \quad (1.13)$$

If indeed $\langle \hat{A} \rangle(t \rightarrow \infty) \simeq \langle \hat{A} \rangle_{\text{eq}}$, then equilibration is the result of dephasing between the different oscillating terms in Eq. (1.11), only leaving the diagonal contributions (Eq. (1.13)) to the observable. The statistical ensemble with weights $|c_n|^2$ is dubbed *diagonal ensemble*. Such an ensemble is in principle dictated by the specific choice of the initial state of the evolution through the coefficients c_n . Hence it is not at all obvious how it can provide expectation values for local observables that would correspond to those of a Gibbs ensemble, Eq. (1.9), given that the latter depends on $|\Psi_0\rangle$ only through its energy and not through its full structure. How can one lose memory of the initial state and therefore achieve ergodicity in a quantum evolution ?

Sufficient conditions to recover ergodicity are provided by a set of assumptions forming the framework of the *Eigenstate Thermalization Hypothesis* (ETH) [75]. This hypothesis states that consecutive eigenstates of Hamiltonians that lead to thermalizing evolutions have very similar physical properties, namely that, for any local observable \hat{A} , $A_{n,n} = \langle \psi_n | \hat{A} | \psi_n \rangle$ and $A_{n+1,n+1} = \langle \psi_{n+1} | \hat{A} | \psi_{n+1} \rangle$ differ by an amount which scales exponentially to zero with the system size, similarly to the energy difference $E_{n+1} - E_n$; namely the limit $(A_{n+1,n+1} - A_{n,n}) / (E_{n+1} - E_n) \rightarrow_{E_{n+1} - E_n \rightarrow 0} f(E_n)$ is well defined, and therefore the expectation values of the local observables are smooth functions of the eigenstate energies, $A_{nn} \simeq A(E_n)$. Moreover, for a generic initial state $|\Psi_0\rangle$ of energy E_0 and a Hamiltonian composed of local terms $\hat{\mathcal{H}} = \sum_i \hat{\mathcal{H}}_i$ (where $\hat{\mathcal{H}}_i$ is an operator acting on a finite support around site i of a lattice) the energy is a self-averaging quantity, namely

$$\frac{\delta E}{E_0} = \frac{\sqrt{\langle \hat{\mathcal{H}}^2 \rangle - \langle \hat{\mathcal{H}} \rangle^2}}{E_0} = \frac{\sqrt{\sum_{ij} \langle (\mathcal{H}_i - \langle \mathcal{H}_i \rangle) (\mathcal{H}_j - \langle \mathcal{H}_j \rangle) \rangle}}{E_0} \sim \frac{1}{\sqrt{N}}, \quad (1.14)$$

where we have used the fact that $E_0 = O(N)$, and that for generic quantum states the correlation function $\langle (\mathcal{H}_i - \langle \mathcal{H}_i \rangle) (\mathcal{H}_j - \langle \mathcal{H}_j \rangle) \rangle$ is exponentially decaying, so that its double integral is extensive.

As a consequence the sum over eigenstates in Eq. (1.13) has support on an energy window whose relative width scales to zero with the system size. This aspect, added to the fact that the A_{nn} are smooth functions of the energy, implies that for $N \gg 1$ the diagonal ensemble average for generic initial states coincides in practice with a microcanonical average over an energy window $\delta E = O(\sqrt{N})$

$$\langle \hat{A} \rangle_{\text{eq}}(E_0) = \lim_{N \rightarrow \infty} \frac{1}{N_{E_0, \delta E}} \sum_{n: |E_n - E_0| \leq \delta E} A_{nn}, \quad (1.15)$$

regardless of the (generic) initial state. In order for Eq. (1.15) to represent the asymptotic value of observables, a further condition must be imposed on the off-diagonal matrix elements A_{nm} ($n \neq m$). We shall not discuss this condition here, and we refer the reader to Ref. [27] for an in-depth review.

In classical systems, the validity of statistical mechanics hinges upon the ergodicity of the considered system, and in particular it breaks down in cases where the model displays integrability, as the system evolves on closed orbits of phase space [27]. Similarly, the ETH may fail to describe the relaxation of quantum systems if the system is characterized by an extensive number of integrals of motion [89]. Indeed, the ETH leads to a description of quantum states in terms of a Gibbs ensemble which only accounts for the conservation of energy, and therefore it should be generalized so as to include the conservation of further integrals of motion. A complete statistical image of integrable systems is then provided by a new statistical ensemble dubbed as *Generalized Gibbs Ensemble* (GGE) [76] described by a distribution of the form,

$$\hat{\rho}_{\text{GGE}} = \frac{1}{Z_{\text{GGE}}} e^{-\sum_j \lambda_j I_j}, \quad (1.16)$$

where each λ_j is a Lagrange multiplier attached to a different integral of motion I_j . Approximating a non-integrable quantum system (verifying ETH) with an integrable one - for instance via a harmonic approximation, as we shall discuss at length in Chap. 2 - is often a practical way to get a theoretical handle on the behaviour of many-body systems. Yet clearly through such an approximation one is missing fundamental aspects of the original system. In several cases, though, integrable many-body systems are "close" to integrable ones - at least in some specific energy range- in the sense that integrability-breaking terms (such as non-linearities beyond the harmonic approximation) can be considered as weak perturbations. Under this assumption there is a separation of time-scales between:

1. a short-time dynamics, governed by the integrable part of the Hamiltonian and leading the system to relax to a transient state with properties compatible with a GGE;
2. a long-time dynamics in which the integrability-breaking terms eventually start playing a role, driving the system toward a state compatible with an ordinary Gibbs ensemble. In this scenario the nearly-integrable system is said to display *pre-thermalization* to a GGE before thermalizing to a standard GE.

The introduction of strong disorder, on the other hand, causes the complete breakdown of the ETH framework as it violates its cornerstone assumption: namely the hypothesis that eigenstates in the same energy window are sufficiently alike for the expectation value of local observables to be almost identical. The possibility that disorder contradicts this fundamental assumption of the ETH can be understood in the context of non-interacting quantum systems, where, by

means of destructive interference effects, disorder induces Anderson localization of the eigenstates. As a consequence, energetically close localized wavefunctions may actually be localized in widely different regions of the system and give different expectation values for a same local observable. A similar phenomenon occurs at the many-body level when the so-called *many-body localization* [2, 70] takes place: in many-body localized systems consecutive energy eigenstates may be radically different - e.g in the spatial distribution of particles, which adjust differently to an external disordered potential, yet with very similar energies. If disorder is very strong, the kinetic part of the Hamiltonian may fail to hybridize such quasi-degenerate spatial distributions, which result then in quasi-degenerate eigenstates with very different expectation values of local observables. As a result of the breakdown of ergodicity, the dynamics of many-body localized systems is unable to fully erase the memory of the initial state, and the localization dynamics does not admit a Gibbs ensemble description.

1.1.4 Rydberg atom simulators

The latest decades witnessed a leap forward in the study of cold atomic gases. Since the first experimental realization of a Bose-Einstein condensate in 1995 by Cornell and Wieman [5] and Ketterle [28], several cold-atom experiments were designed in order to mimic and study the properties of condensed matter systems, giving access to regimes which are inaccessible in the condensed-matter realm; as well as to novel ways to diagnose their behaviour [17].

An example commonly used to illustrate this research program is the experimental study of the superfluid-Mott insulator transition using a gas of cold bosonic atoms trapped in an optical lattice [43]. Let us consider a gas of laser-cooled bosonic atoms placed at the intersection of several coherent laser beams, thus creating a periodic interference pattern realizing a periodic potential for the atoms. In an effective description, the bosons can tunnel from one site of the lattice to a neighbouring one, despite the repulsive interactions penalizing multiple occupancy of a single site. If the tunneling prevails on the repulsion, the atoms can delocalize over the whole lattice and form a coherent superfluid condensate; on the other hand if interactions are predominant, they induce a Mott insulator phase where atoms are localized.

In the case of the implementation of the Bose-Hubbard model in cold atoms, the interplay between hopping and repulsion can be continuously tuned by modulating the intensity of the laser trap which controls the depth of the optical lattice. The transition between a superfluid and an insulating phase can then be directly studied by means of absorption images after time of flight of the interference pattern formed after the release of the atomic cloud from the trap. As it can be seen in Fig. 1.3 for small depths of the optical lattice - when tunneling is dominating - the interference pattern exhibits sharp peaks manifesting the phase coherence of a superfluid phase. However, as the lattice depth increases the peaks progressively start to blur and ultimately become rounded maxima, thus heralding the loss of coherence and the emergence of the Mott insulator.

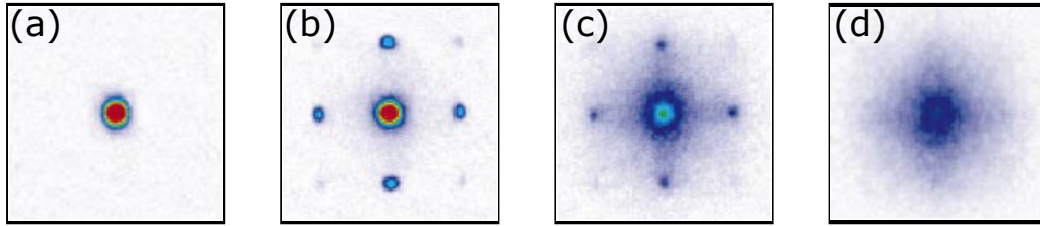


Figure 1.3: Quantum simulation of the superfluid-Mott insulator transition - examples of absorption image obtained of the interference pattern obtained after releasing the particles from the trap : (a) $V_0 = 0E_r$, (b) $V_0 = 3E_r$, (c) $V_0 = 14E_r$, (d) $V_0 = 16E_r$, where V_0 is the lattice depth and E_r the recoil energy (pictures adapted from [43]).

Another fundamental field of interest for quantum simulation is the study of quantum magnetism of localized spins. If a Mott insulator is realized using spinful atoms (either bosonic or fermionic), the residual motion of the atoms around the site at which they are pinned leads to effective exchange interactions between the spins [31]; this mechanism is at the basis of e.g. antiferromagnetism in magnetic insulators [8]. Yet observing antiferromagnetic spin correlations in atomic Mott insulators, while achieved in some remarkable experiments [62], remains a challenge because of the very low entropies required for the spin ensemble to develop ordering. An alternative route for the study of quantum magnetism in atomic physics is offered by Rydberg atoms [20].

Rydberg atoms are atoms in which an electron got promoted to a high-energy state ($n = 50$, for instance). They are characterized by their long lifetime (generically of the order of $100\mu\text{s}$ for $n = 50$) that scales with the principal quantum number like $\tau \propto n^3$. Besides, as the excited electron lies in a highly excited orbital, the electric dipole moment of Rydberg atoms is also especially large and scales like $d \propto n^2$. This property is particularly interesting as it stands at the origin of the so-called *Rydberg blockade*. Indeed, below a distance R_b called the blockade radius, the energetic cost of the dipole-dipole interactions (in the form of van der Waals interactions decaying as $1/R^6$ with R the interatomic distance) prevents two atoms from being simultaneously driven to the same Rydberg state. As a result the transition to the doubly excited state becomes off-resonant in favour of an entangled state $|\psi\rangle = (|gr\rangle + |rg\rangle)/\sqrt{2}$, where $|g\rangle$ stands for the ground state of the atom and $|r\rangle$ for the driven Rydberg state.

Further progress in the trapping and manipulation of individual atoms using arrays of optical tweezers has opened the way to the realization of *Rydberg-atom simulators*, offering an ideal platform for the quantum simulation of magnetism, as we shall describe in the following paragraphs.

Rydberg atoms are mappable in an effective manner onto $S = \frac{1}{2}$ spins, by associating the Rydberg state to spin-up state ($|r\rangle = |\downarrow\rangle$) and ground state to spin-down state ($|g\rangle = |\uparrow\rangle$) [80]. Considering a set of laser-cooled atoms pinned on the sites of a regular lattice and exposed to an external laser driving the transition $|g\rangle \rightarrow |r\rangle$, their interactions are described by the atomic Hamiltonian,

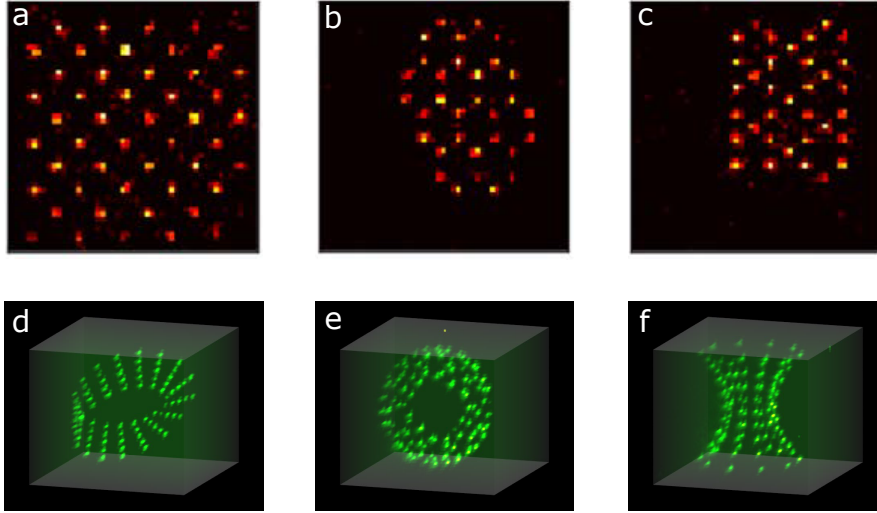


Figure 1.4: Examples of 2d and 3d arrays of trapped atoms - the upper row shows two-dimensional realization of atom arrays : (a) a square lattice, (b) a honeycomb lattice, (c) a kagomé lattice (pictures from [12]). On the other hand, the lower row shows three-dimensional atomic structures : (d) a Möbius stripe, (e) a torus and (f) a hyperboloid (pictures from [11])

$$\hat{\mathcal{H}} = \frac{\Omega}{2} \sum_i (\hat{\sigma}_i^{rg} + \hat{\sigma}_i^{gr}) - \Delta \sum_i \hat{\sigma}_i^{rr} + \frac{1}{2} \sum_{i \neq j} V_{ij} \hat{\sigma}_i^{rr} \hat{\sigma}_j^{rr}, \quad (1.17)$$

with $\hat{\sigma}_i^{rg} = |g\rangle_i \langle r|_i$ and $\hat{\sigma}_i^{gr} = |r\rangle_i \langle g|_i$. While the first term describes the Rabi coupling of amplitude Ω between the ground state and the Rydberg state induced by the driving laser, the second accounts for the detuning $\Delta = \omega - \omega_{g \rightarrow r}$ between the laser frequency and the actual atomic transition frequency. As for the third term, it contains the dipole-dipole interactions between the Rydberg states, with $V_{ij} = C_6/|\mathbf{r}_i - \mathbf{r}_j|^6$ taking the form of a van der Waals interaction.

The atomic Hamiltonian can then be recast as a spin system by using the aforementioned identification between atomic and spin states. Indeed, according to this prescription $|g\rangle_i \langle r|_i = |\downarrow\rangle_i \langle \uparrow|_i$ accounts for spin-flip operator at site i , while $|r\rangle_i \langle g|_i = |\uparrow\rangle_i \langle \downarrow|_i$ counts the population of up-oriented spins at this same site. Besides, by using the identities $\hat{S}_i^x = (|\uparrow\rangle_i \langle \downarrow|_i + |\downarrow\rangle_i \langle \uparrow|_i)/2$ and $|\uparrow\rangle_i \langle \uparrow|_i = \hat{S}_i^z + 1/2$, the Hamiltonian can be rewritten as an Ising model immersed in transverse and longitudinal magnetic fields,

$$\hat{\mathcal{H}} = \Omega \sum_i \hat{S}_i^x + \sum_i (\kappa_i - \Delta) \hat{S}_i^z + \frac{1}{2} \sum_{i \neq j} V_{ij} \hat{S}_i^z \hat{S}_j^z, \quad (1.18)$$

where $\kappa_i = \frac{1}{2} \sum_{j, i \neq j} V_{ij}$. Therefore, Rydberg atoms offer an experimental platform for the exploration of the physics of quantum Ising models.

In addition to their suitability to mimic the physics of antiferromagnetic spin systems, Rydberg simulators also demonstrated the ability to arrange the atoms into complex crystalline structures in dimensions $d = 1, 2$ or 3 [11, 12], thus opening

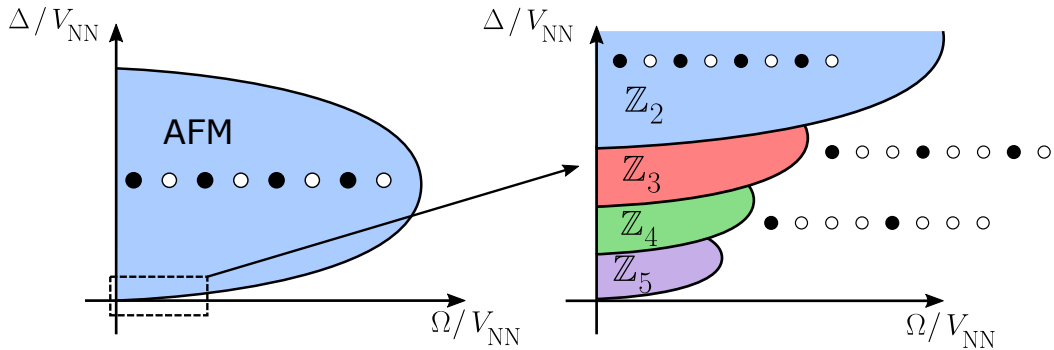


Figure 1.5: Phase diagram of a one-dimensional Rydberg-atom simulator on the plane defined by the ratios between Rabi driving Ω , detuning Δ and nearest-neighbour coupling $V_{\text{NN}} = C_6/a^6$, where a stands for the lattice spacing. Rydberg blockade leads to the emergence of a Néel state (Rydberg states are represented as black dots and ground states a white ones), however for strong nearest neighbours interactions \mathbb{Z}_n -symmetric phases appear.

the way to the experimental study of systems where the interplay of antiferromagnetism and geometry is especially determinant, such as in frustrated systems. This high tunability of the system geometry is reached by trapping each atom in an individual dipole trap called optical tweezer; the ensemble of tweezers can then be arranged in a controlled manner in order to reproduce translational invariance and symmetries. A few examples of atom arrays that can be produced using this technique are shown in Fig. 1.4.

Seminal experiments have demonstrated the appearance of spin-spin correlations induced by the above many-body Hamiltonian between Rydberg atoms, either via a quench protocol from an initially factorized state [14, 54], or via an adiabatic protocol [45, 59] aiming at reproducing the ground-state correlations of the quantum Ising model in its long-range ordered phase. In either case, these experiments explored a rich phase diagram shown in Fig. 1.5, where one can observe that interactions among Rydberg atoms compete with the Rabi driving and the detuning to lead to a quantum phase transition between a \mathbb{Z}_2 -ordered phase (with a finite staggered magnetization) and a disordered state. Moreover, more complex states with \mathbb{Z}_n -order appear when interactions beyond nearest neighbours become important.

The Ising model is actually only one of the spin models that can possibly be simulated by Rydberg atoms. Another regime accessible to the experimental set-ups of trapped atoms enables to implement dipolar XX spin models. This model relies on two types of Rydberg states coupled by a microwave electromagnetic field, both with the same principal quantum number n but differing by their orbital quantum number, for instance the pair $|n, s\rangle$ and $|n, p\rangle$. In that case the dipole-dipole interactions induce a state exchange between two atoms $|n, s\rangle_1 |n, p\rangle_2 \leftrightarrow |n, p\rangle_1 |n, s\rangle_2$, with an exchange rate directly related to the dipolar

interactions $V_{ij} = C_3(1 - 3 \cos^2 \theta)/|\mathbf{r}_i - \mathbf{r}_j|^3$, where θ is the angle between the quantization axis and the internuclear axis. By identifying the Rydberg states as spin states in the following manner $|n, s\rangle = |\downarrow\rangle$ and $|n, p\rangle = |\uparrow\rangle$, the Hamiltonian can be written as

$$\hat{\mathcal{H}} = \Omega \sum_i \hat{S}_i^x - \Delta \sum_i \hat{S}_i^z + \sum_{i \neq j} V_{ij} \left(\hat{S}_i^+ \hat{S}_j^- + \hat{S}_i^- \hat{S}_j^+ \right). \quad (1.19)$$

This model can be mapped onto a model of hardcore bosons with dipolar hopping, and it has been used to investigate transport and the emergence of edge states in an interacting version of the Su-Schrieffer-Heeger model (SSH) [60].

Rydberg simulators, due to the high control they offer on the lattice geometry and to the richness of possible models they exhibit, offer a precious springboard for the study of models relevant for condensed matter physics, and they already proved their ability to explore a very wide spectrum of phenomena. In the following we will mainly focus on the transverse-field Ising model and the possibilities it offers for the exploration of exotic quantum dynamics.

Individually trapped Rydberg atoms are not the only quantum simulators that offer the possibility to investigate the physics of quantum spin systems; another popular platform for the quantum simulation of quantum magnetism is offered by trapped ions [82]. The internal states of the ions encoding $S = 1/2$ spins are coupled via virtual phonons of the Coulomb crystal induced by external lasers. The laser frequency selects the phonon modes involved in the process, thereby controlling the spatial structure of the couplings. The setup realizes a long-range Ising model in a transverse field with the Hamiltonian

$$\hat{\mathcal{H}} = \frac{1}{2} \sum_{i \neq j} \frac{J_0}{|\mathbf{r}_i - \mathbf{r}_j|^\alpha} \hat{S}_i^z \hat{S}_j^z - \Omega \sum_i \hat{S}_i^x, \quad (1.20)$$

where the exponent α can be varied in the interval $0 < \alpha < 3$.

Finally, we can summarize the different spin Hamiltonians accessible to quantum simulation on Rydberg-atom and trapped-ion set-ups by the α - XXZ model in longitudinal and transverse magnetic fields, whose Hamiltonian reads:

$$\begin{aligned} \hat{\mathcal{H}}_{\alpha-XXZ} = & \frac{1}{2} \sum_{i \neq j} \frac{1}{|\mathbf{r}_i - \mathbf{r}_j|^\alpha} \left[\frac{J}{2} \left(\hat{S}_i^+ \hat{S}_j^- + \hat{S}_i^- \hat{S}_j^+ \right) + J_z \hat{S}_i^z \hat{S}_j^z \right] \\ & - \sum_i \left[\Omega \hat{S}_i^x + H \hat{S}_i^z \right]. \end{aligned} \quad (1.21)$$

1.2 The challenge of quantum complexity

As we have discussed in the previous section, quantum many-body systems feature a rich phenomenology of dynamical effects related to fundamental aspects of relaxation and thermalization. Experimentally, dynamics following the perturbation of a system is also used to extract information on its properties by analyzing

how it responds to the perturbation in question. For these reasons, the study of dynamics motivates the development of experimental platforms offering possibilities for quantum simulation, but also numerical approaches that can tackle the problem of many-body dynamics. However, apart from some very specific models which exhibit explicit solutions to their equations of motion, the study of the dynamics in quantum many-body physics is a challenging problem that can only be addressed by means of cutting-edge numerical approaches. In the following, we will review some of the strategies developed to provide predictions on the dynamics of many-body systems.

1.2.1 Exact diagonalization and beyond

Considering an assembly of N quantum objects described by local Hilbert spaces \mathfrak{h}_i of arbitrary dimension D , the ensemble of possible states that the whole system can explore is a Hilbert space $\mathfrak{H} = \otimes_i \mathfrak{h}_i$ of dimension D^N . As a result, the exponentially growing number of independent variables to handle puts large systems out of reach for exact diagonalization schemes, mainly as a matter of memory storage. However, the use of clever numerical methods can help reduce the complexity of the calculations compared to a naive, brute-force approach. One of the most celebrated examples of such numerical methods is the Lanczos algorithm [55] designed to reconstruct a portion of the spectrum of large matrices. Given an arbitrary state $|\psi\rangle$, the algorithm consists in projecting the Hermitian matrix \mathcal{H} on the m -th order Krylov space $\mathcal{K}_m(|\psi\rangle) = \text{Span}\{|\psi\rangle, \mathcal{H}|\psi\rangle, \mathcal{H}^2|\psi\rangle, \dots, \mathcal{H}^{m-1}|\psi\rangle\}$, where it can be written in term of a $m \times m$ tridiagonal matrix which can be diagonalized with a much smaller numerical cost.

In order to explore the physics and dynamics of quantum many-body systems for sizes beyond the reach of exact diagonalization, we need to renounce to exactly reconstructing the many-body state. A general strategy is to find an Ansatz (a guess of the state's form) that captures enough of its physical properties so as to provide a faithful description in terms of a smaller amount of independent parameters, ideally scaling polynomially with system size N . The starting point of this quest should be the most basic level of understanding we can grasp of the physics at hand, and this level is generically offered by the mean-field approximation which amounts to approximating the quantum state with a factorized form (Eq. (1.4)). Although this description proves to be effective in the treatment of many-body phenomena such as superconductivity (within the celebrated Ginzburg-Landau theory), it totally neglects the existence of entanglement, hence the need to complete the mean-field approach with quantum correlations. This aim can be achieved in two main ways:

1. One can make an educated guess (Ansatz) of the wavefunction which entangles the degrees of freedom in the manner most appropriate to the physics of the system under investigation, and then adjust the parameters according to a variational principle valid either for the search of ground state or of Hamiltonian evolutions. This strategy represents the basis of the variational approaches.

2. The other strategy is based on developing so-called semi-classical methods, in which quantum mechanical corrections to a mean-field description (or to a fully classical description) are taken into account only partially in order to make the problem tractable. Semi-classical approaches may consist in refining the mean-field image in order to take into account quantum correlations, by building a linearized quantum field theory on top of the mean-field picture (as done e.g. in Bogoliubov theory); or by introducing quantum noise in the initial state of a classical evolution dynamics of classical spins (as done in the so-called Truncated Wigner Approximation).

In the following, we will discuss these two approaches, the possibilities they offer and their limitations.

1.2.2 Variational approaches

The principle of the variational method consists in finding a relevant representation for the quantum state parametrized by a set of adjustable parameters that need to be optimized in order to minimize some functional of the state, namely the expectation value of the Hamiltonian when searching for the ground state, or the action if our interest is focused on dynamics [13].

Let us start from the assumption that the many-body state is faithfully described by a variational state parametrized by a vector $\mathbf{a}(t) \in \mathbb{C}^m$ of time-dependent variational parameters whose number is assumed to scale polynomially with system size N : $m \sim N^k$,

$$|\Psi(\mathbf{a})\rangle = \sum_{\boldsymbol{\sigma}} c_{\boldsymbol{\sigma}}(\mathbf{a}) |\boldsymbol{\sigma}\rangle, \quad (1.22)$$

where the sum runs over an orthonormal factorized basis $|\boldsymbol{\sigma}\rangle = |\sigma_1\rangle \otimes \cdots \otimes |\sigma_N\rangle$ of the Hilbert space.

At this point it is important to stress that for the same problem several possible variational Ansätze are possible and may give similar results, while on the contrary some others are inefficient for the considered class of systems and would fail at providing a satisfactory description. Knowing the limits of a variational approach is then essential in order to determine its relevance and efficiency in exploring the physics of a system. In the following, we will shortly review two major classes of variational states: Tensor Network States (TNS) and correlated variational states treated with time-dependent variational Monte Carlo algorithms (tVMC)

Matrix Product States The Matrix Product States (MPS) [83] belong to the wide family of TNS Ansätze which also encompass Projected Entangled Pairs State (PEPS) [85]. Let us consider a chain of N sites: a matrix product state has coefficients $c_{\boldsymbol{\sigma}}$ parametrized as the trace of a matrix product,

$$|\Psi\rangle = \sum_{\boldsymbol{\sigma}} \text{Tr} [A_1^{\sigma_1} \cdots A_N^{\sigma_N}] |\sigma_1 \cdots \sigma_N\rangle \quad (1.23)$$

where the $A_i^{(\sigma_i)}$ are a set of $\chi \times \chi$ matrices, one for each state of the local Hilbert space (of dimension D). As a result, MPS states are described by a linearly growing number of free parameters $m = ND\chi^2$, χ being called the bond dimension.

Though very efficient in the investigation of ground-state properties, MPSs suffer from a limitation linked to entanglement, restricting their efficiency for the study of quantum dynamics. First and foremost, the amount of entanglement that can be encoded in MPS states depends logarithmically on the bond dimension $E_A = \ln \chi$, meaning that we need an exponentially growing bond dimension in order to faithfully reproduce states with volume-law entanglement scaling. MPS states provide a very good description of the dynamics for short times, when the amount of entanglement remains limited, but ultimately fail to provide insights on the equilibration of quantum systems. These limitations are common to further TNS, such as PEPS extending MPS construction to approximate weakly entangled many-body states at dimension $d > 1$.

Artificial Neural Network states A valuable alternative to TNS is offered by a class of states in which coefficients c_σ are given an explicit functional form. An example thereof are so-called entangled plaquette states (EPS) [65] or correlator product states (CPS) [24], for which

$$c_\sigma = \prod_{ij} f_{ij}(\sigma_i, \sigma_j), \quad (1.24)$$

where f_{ij} are functions of the spin configuration of a pair of lattice sites, introducing correlations among them. A most general parametrization of such functions for $S = 1/2$ systems is in the form

$$f_{ij}(\sigma_i, \sigma_j) = \exp(a_i \sigma_i + a_j \sigma_j + b_{ij} \sigma_i \sigma_j). \quad (1.25)$$

Another popular example of such functions, hinging upon the representation of N -argument functions via neural networks, is offered by the so-called neural network quantum states, such as the one built upon a restricted Boltzmann machine [22]

$$|\Psi\rangle = \sum_{\sigma} e^{\sum_i a_i \sigma_i} \prod_{j=1}^M 2 \cosh \left[b_j + \sum_{i=1}^N W_{ji} \sigma_i \right] |\sigma_1 \dots \sigma_N\rangle, \quad (1.26)$$

where $\{a_i\}$, $\{b_j\}$ and $\{W_{ji}\}$ are complex variational parameters for the Ansatz. All these states can be optimized or time evolved by Monte Carlo sampling of their average energy (and gradients thereof, calculated with respect to the variational parameters); therefore their use to study many-body physics at equilibrium or away from it goes generally under the name of variational Monte Carlo (VMC).

Unlike TNS, the above states can exhibit volume-law scaling of entanglement entropy. Yet, also unlike TNS, it is difficult to efficiently extend their parameters so as to progressively span the whole Hilbert space. Therefore their use may often lead to results that cannot be systematically improved.

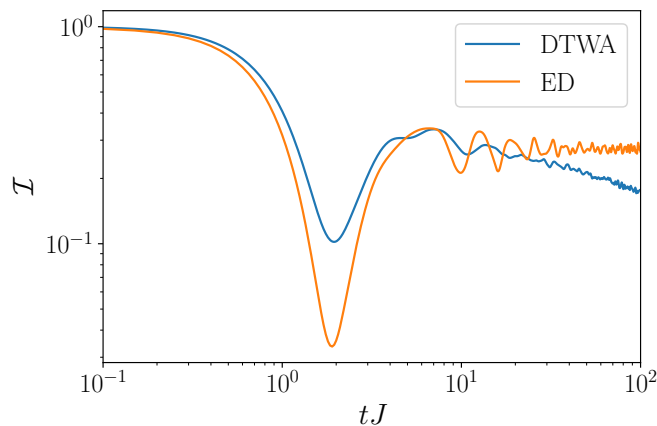


Figure 1.6: Dynamics of spin imbalance for an XX spin chain of length $L = 50$ in a random z -oriented magnetic field. The dynamics was computed both using the DTWA approach and exact diagonalization using Jordan-Wigner transformation and averaged over 50 realization of disorder.

1.2.3 Semi-classical methods

As we outlined earlier, an alternative to variational Ansätze for the study of many-body physics is offered by semi-classical approaches. This thesis will fundamentally rely upon the idea of building a linearized quantum-field theory on top of the mean-field approximation, as it will be fully explained in the next chapter. As already mentioned above, an alternative to this approach is offered by the Truncated Wigner Approximation (TWA).

The TWA method is built upon the formalism of the Wigner transform which represents a wavefunction as a function defined on the classical phase space of the problem [102], thus establishing a correspondence between the Hilbert space of quantum states and configurations of an equivalent classical system. The phase-space representation of the quantum state, the so-called Wigner function, is a pseudo-probability distribution of classical configurations accounting for the noise inherent in the quantum nature of the state. When the Wigner function is non-negative, the TWA approach consists of using it as a probability distribution to sample initial conditions of the dynamics, which are subsequently evolved using classical equations of motion. Classical observables average over different classical trajectories generated in this way can then be used to reconstruct the evolution of quantum operators. This approximation has been recently specialized to discrete quantum systems (DTWA) such as spins [79], where the classical equations of motion amount to a precession dynamics, reading

$$\frac{d}{dt}\mathbf{S}_i = \boldsymbol{\Omega}(\{\mathbf{S}\}) \times \mathbf{S}_i, \quad (1.27)$$

where \mathbf{S}_i is a classical vector on a sphere, and $\boldsymbol{\Omega}(\{\mathbf{S}\})$ is the sum of an external magnetic field and of the field instantaneously induced by the other spins on the i -th spin.

Despite showing good agreement with exact results on short time scales, the DTWA has fundamental limitations in describing accurately the relaxation of quantum many-body states. Indeed, at long times, the classical nature of the equations of motion brings the system towards a classical thermal state, as ergodicity generically loses memory of the quantum origin of the initial conditions. The DTWA is bound to fail to account for quantum interference effects, especially in cases where these effects are dominant as in the case of Anderson localization. This effect is illustrated in Fig. 1.6, where the time evolution of the spin imbalance, or staggered magnetization, defined as

$$\mathcal{I} = \frac{1}{N} \sum_i (-1)^i \langle S_i^z \rangle, \quad (1.28)$$

is represented for a XX spin chain initialized in a Néel state $|\uparrow\downarrow\uparrow\downarrow\dots\rangle$, and exposed to a random magnetic field $-\sum_i h_i S_i^z$, where h_i is uniformly distributed over the window $[-W, W]$, with $W = 2$. In this case, the spin model can be reformulated in terms of free fermions in a random potential, realizing Anderson localization. While the exact calculation of the spin imbalance reaches a plateau at long times, the DTWA calculations, after agreeing at short times with the exact solution, show at longer times a slow relaxation towards 0, the failure to reproduce localization.

The conclusion of this brief review of the different approaches to dynamics is that, beyond the exact diagonalization algorithms, there is no universal method which equals in any case the same level of accuracy as exact solutions. The method we will present in the next chapter is not an exception, although it offers several advantages, compared to the methods discussed so far, in terms of the simplicity of the approach, as well as of the showcase of quantum phenomena that it can describe.

Gaussian approaches for quantum spin systems

*"L'ange qui descend et qui monte
Sur l'escalier d'or voltigeant ;
La cloche mêlant dans sa fonte
La voix d'airain, la voix d'argent ;"*

Théophile Gautier, "Contralto", *Emaux et Camées*

2.1 Linear spin-wave theory

2.1.1 Quantum-field corrections to mean-field

In this chapter we will discuss the theoretical approach which is at the heart of the original results presented in this thesis, namely the semiclassical approach based on adding quantum corrections to the mean-field solution of the many-body problem, either at equilibrium or away from it.

This approach is widespread in the context of many-body physics, and it is the basis of seminal theoretical approaches for quantum fluids and lattice models:

1. In the context of bosonic fluids, quantum corrections to the mean-field solution are described by Bogoliubov theory, which, in its modern formulation [35], represents the correction to Gross-Pitaevskii (GP) theory, namely to the solution of the many-body problem assuming the existence of a perfect condensate with a macroscopic wavefunction satisfying the nonlinear Gross-Pitaevskii equation. Bogoliubov theory describes the particles pushed outside of the condensate by the interactions as a gas of non-interacting quasi-particles, obtained by the diagonalization of the Hamiltonian approximated to a *quadratic* form around the GP solution.
2. A similar construction in the context of fermionic fluids is that of Bardeen-Cooper-Schrieffer (BCS) theory, which, on its most general formulation, can

be viewed as a description in terms of a quadratic fermionic Hamiltonian of the elementary excitations on top of a condensate of Coopers pairs – which, unlike in Bogoliubov theory, is self-consistently calculated from the solution of the quadratic Hamiltonian.

Finally in the context of spin systems, most relevant for this thesis, the above approach is embodied by spin-wave theory, which consists in the search for the ground state of the Hamiltonian in the classical limit of infinite spins ($S \rightarrow \infty$); and to the calculation of the first quantum correction to such a picture via a spin-to-boson mapping of the Hamiltonian; and to a description of the deviations of the spins from this classical ground-state orientation as a gas of non-interacting bosonic quasi-particles, in a very similar manner to what is done in Bogoliubov theory.

In the following, we shall discuss in details linear spin-wave theory in the specific case of the quantum Ising model, inspired by the capabilities of Rydberg-atom simulators.

2.1.2 Spin-boson projection

In order to conduct our study, we shall give ourselves a general framework fitting the description of any spin systems described by the tranverse field Ising model, under the unique assumption that the ground state displays long-range order, either spontaneous or induced by an external field. So let us consider N spins arranged on a lattice: the magnetic structure of the ordered ground state usually defines a unit cell containing n distinct elements (e.g. $n = 2$ in the case of the antiferromagnetic square lattice). We shall consider Ising spins coupled according to a distance-dependent function $J(r)$ and immersed in a magnetic field $\mathbf{B} = (\Omega, 0, \Delta)$ in the $x - z$ plane. The Hamiltonian then reads

$$\hat{\mathcal{H}} = \frac{1}{2} \sum_{lp, l'p'} J_{pp'}^{ll'} \hat{S}_{lp}^z \hat{S}_{l'p'}^z - \Omega \sum_{lp} \hat{S}_{lp}^x - \Delta \sum_{lp} \hat{S}_{lp}^z, \quad (2.1)$$

where the pair of indices (l, p) labels the unit cell and the site on the unit cell, respectively. The matrix we previously used to encode the couplings between spins can be rewritten as $J_{pp'}^{ll'}$, a $N \times N$ matrix of $n \times n$ blocks, each describing the couplings between the unit cells l and l' .

Mean-field approximation – The linear spin-wave theory approach starts from the construction of a reference state displaying long-range order, which in general corresponds to the ground-state of the model in the classical ($S \rightarrow \infty$, where S is the spin length) limit. The construction can also be done at the level of quantum states in a variational manner, by using a mean-field Ansatz for the ground state. For a set of spin- $\frac{1}{2}$, the mean-field picture is provided by a factorized form, in which each spin has a well-defined orientation of states on a Bloch sphere parametrized by the angles (θ_{lp}, ϕ_{lp})

$$|\Psi_{\text{MF}}\rangle = \bigotimes_{l,p} \left(\cos\left(\frac{\theta_{lp}}{2}\right) |\uparrow\rangle_{lp} + e^{i\phi_{lp}} \sin\left(\frac{\theta_{lp}}{2}\right) |\downarrow\rangle_{lp} \right). \quad (2.2)$$

The determination of the proper set of angular parameters defining this Ansatz relies on the variational minimization of the mean-field energy, defined as

$$E_{\text{MF}}(\{\theta_{lp}\}, \{\phi_{lp}\}) = \langle \Psi_{\text{MF}} | \hat{\mathcal{H}} | \Psi_{\text{MF}} \rangle. \quad (2.3)$$

Generically, the mean-field state exhibits translational invariance, such that every unit cell has the same magnetic structure. Therefore the number of free variables to determine in the minimization of the energy is reduced to n pairs of angles (θ_p, ϕ_p) .

For spins of arbitrary length S the Ansatz for the ground state takes the more specific form of a so-called coherent spin state (CSS) :

$$|\Psi_{\text{CSS}}\rangle = \bigotimes_{lp} |S_{(\theta_p, \phi_p)}\rangle_{lp}, \quad (2.4)$$

where $|S_{(\theta_p, \phi_p)}\rangle$ is the state of an S -spin fully aligned with the (θ_p, ϕ_p) direction on the unit sphere. Even though we shall develop the following treatment to the case of an arbitrary value of S , all of our results will be specialized to the case $S = 1/2$, relevant for the physics of Rydberg-atom simulators.

For the model at hand (Ising spins coupled to a magnetic field), the orientations of the spins in the above factorized states can be searched in the $(x - z)$ plane in order to minimize the spin-spin interaction and the coupling to the field, namely $\forall p, \phi_p = 0$. The angles θ_p define an operator transformation as a set of local rotations around the y -axis $\mathcal{R}_y(\theta_p)$ which will bring the local z -axis to coincide with the axis defined by the mean-field orientation. Under such a rotation the spin operators transform as

$$\begin{aligned} \hat{S}_{lp}^{x'} &= \cos\theta_p \hat{S}_{lp}^x - \sin\theta_p \hat{S}_{lp}^z \\ \hat{S}_{lp}^{y'} &= \hat{S}_{lp}^y \\ \hat{S}_{lp}^{z'} &= \cos\theta_p \hat{S}_{lp}^z + \sin\theta_p \hat{S}_{lp}^x, \end{aligned} \quad (2.5)$$

and the trial ground state becomes a perfect ferromagnet with all spins aligned along the z' axis. The Ising Hamiltonian, in terms of these rotated spins, takes the form

$$\begin{aligned} \hat{\mathcal{H}} &= \frac{1}{2} \sum_{lp, l'p'} J_{pp'}^{ll'} \left(\cos\theta_p \cos\theta_{p'} \hat{S}_{lp}^{z'} \hat{S}_{l'p'}^{z'} + \sin\theta_p \sin\theta_{p'} \hat{S}_{lp}^{x'} \hat{S}_{l'p'}^{x'} \right) \\ &+ \frac{1}{2} \sum_{lp, l'p'} J_{pp'}^{ll'} \left(\cos\theta_p \sin\theta_{p'} \hat{S}_{lp}^{z'} \hat{S}_{l'p'}^{x'} + \sin\theta_p \cos\theta_{p'} \hat{S}_{lp}^{x'} \hat{S}_{l'p'}^{z'} \right) \\ &- \sum_{lp} [(\Omega \cos\theta_p - \Delta \sin\theta_p) \hat{S}_{lp}^{x'} + (\Omega \sin\theta_p + \Delta \cos\theta_p) \hat{S}_{lp}^{z'}]. \end{aligned} \quad (2.6)$$

Once the mean-field ground state has been established, spin-wave theory amounts to treating the quantum fluctuations beyond the mean-field approximation, which are introduced by means of a mapping of the spins onto a boson field via the Holstein-Primakoff transformation.

Holstein-Primakoff transformation – Let us consider a set of bosonic operators $\hat{b}_{l_p}, \hat{b}_{l_p}^\dagger$ defined on each site of the lattice, such that $[\hat{b}_{l_p}, \hat{b}_{l'_p}^\dagger] = \delta_{ll'}\delta_{pp'}$. The number of bosons on each site maps onto the local spin deviation with respect to the z' direction $\hat{S}_{l_p}^{z'} = S - \hat{b}_{l_p}^\dagger \hat{b}_{l_p}$. Hence, the bosonic Fock space must be truncated to prevent the single-site occupancy to go beyond $\hat{b}_{l_p}^\dagger \hat{b}_{l_p} = 2S$. Building the other spin components so as to satisfy the $SU(2)$ algebra leads the canonical transformation called *Holstein-Primakoff transformation* (HP) [50]

$$\begin{aligned}\hat{S}_{l_p}^{z'} &= S - \hat{b}_{l_p}^\dagger \hat{b}_{l_p} \\ \hat{S}_{l_p}^+ &= \sqrt{2S - \hat{b}_{l_p}^\dagger \hat{b}_{l_p}} \hat{b}_{l_p}\end{aligned}\quad (2.7)$$

$$\hat{S}_{l_p}^- = \hat{b}_{l_p}^\dagger \sqrt{2S - \hat{b}_{l_p}^\dagger \hat{b}_{l_p}}. \quad (2.8)$$

Bosonic commutation relations ensure the preservation of the spin algebra $[\hat{S}_i^\alpha, \hat{S}_j^\beta] = i\epsilon^{\alpha\beta\gamma}\delta_{ij}\hat{S}_i^\gamma$. This non-linear transformation can be linearized under the assumption that the Bose gas with which we approximate the magnetic excitations of the spin system is sufficiently dilute, namely that the bosonic population is far from the maximal allowed population: $\langle \hat{b}_{l_p}^\dagger \hat{b}_{l_p} \rangle \ll 2S$. Under this assumption, we may neglect the boson number with respect to $2S$ under the square roots defining the \hat{S}^+ and \hat{S}^- operators, and have $\hat{S}_{l_p}^\pm \simeq \sqrt{2S} \hat{b}_{l_p}^\pm$. In so doing the spin Hamiltonian is mapped onto that of a system of coupled harmonic oscillators, or in other words a quadratic form of bosonic operators :

$$\hat{\mathcal{H}} = E_{\text{MF}} + \frac{1}{2} \sum_{l_p, l'_p} \begin{pmatrix} \hat{b}_{l_p}^\dagger \\ \hat{b}_{l_p} \end{pmatrix}^T \mathcal{A}_{pp'}^{ll'} \begin{pmatrix} \hat{b}_{l'_p} \\ \hat{b}_{l'_p}^\dagger \end{pmatrix} + O(b^3), \quad (2.9)$$

where E_{MF} is the mean-field energy defined previously, while $\mathcal{A}_{pp'}^{ll'}$ stands for a $n \times n$ real-valued symmetric matrix whose explicit expression is detailed in Appendix A for the case of interest of the Ising model in a magnetic field.

2.1.3 Bogoliubov transformation

The above quadratic Hamiltonian can be block-diagonalized by moving to Fourier space and considering the transformed operators $\hat{b}_{\mathbf{k}, p} = \sqrt{n/N} \sum_l \exp(i\mathbf{k} \cdot \mathbf{r}_l) \hat{b}_{l_p}$, leading to the following expression

$$\hat{\mathcal{H}} \simeq E_{\text{MF}} + \sum_{\mathbf{k}} \begin{pmatrix} \{\hat{b}_{\mathbf{k}, p}^\dagger\} \\ \{\hat{b}_{\mathbf{k}, p}\} \end{pmatrix}^T \mathcal{A}_{\mathbf{k}} \begin{pmatrix} \{\hat{b}_{\mathbf{k}, p}\} \\ \{\hat{b}_{\mathbf{k}, p}^\dagger\} \end{pmatrix}, \quad (2.10)$$

where $\{\hat{b}_{\mathbf{k},p}\}$ are vectors of bosonic operators with n entries, and $\mathcal{A}_{\mathbf{k}}$ is a $2n \times 2n$ matrix. The \mathbf{k} vectors are defined on the Brillouin zone corresponding to the Bravais lattice of N/n magnetic unit cells.

The diagonalization of the quadratic Hamiltonian is accomplished via a linear transformation on the operators which preserves the bosonic commutation relations. Such a transformation, called *Bogoliubov transformation*, introduces new bosonic operators $\hat{\beta}_{\mathbf{k},r}$ and $\hat{\beta}_{-\mathbf{k},r}^\dagger$ as a linear combination of the $\hat{b}_{\mathbf{k},p}$ and $\hat{b}_{-\mathbf{k},p}^\dagger$ operators

$$\begin{pmatrix} \hat{\beta}_{\mathbf{k}} \\ \hat{\beta}_{-\mathbf{k}}^\dagger \end{pmatrix} = T_{\mathbf{k}} \begin{pmatrix} \hat{\mathbf{b}}_{\mathbf{k}} \\ \hat{\mathbf{b}}_{-\mathbf{k}}^\dagger \end{pmatrix} \quad (2.11)$$

Under such a transformation the Hamiltonian describes free quasi-particles

$$\hat{\mathcal{H}}^{(2)} = \sum_{\mathbf{k},r} \omega_{\mathbf{k}}^{(r)} \left(\hat{\beta}_{\mathbf{k},r}^\dagger \hat{\beta}_{\mathbf{k},r} + \frac{1}{2} \right), \quad (2.12)$$

where $\omega_{\mathbf{k}}^{(r)}$ are the eigenenergies attached to the quasi-particle of momentum \mathbf{k} of the r -th band. The preservation of the bosonic commutation relations requires that $T_{\mathbf{k}}$ obeys to the relation $T_{\mathbf{k}} \eta T_{\mathbf{k}}^\dagger \eta = 1$, where

$$\eta = \begin{pmatrix} 1_n & 0_n \\ 0_n & -1_n \end{pmatrix}. \quad (2.13)$$

The eigenenergies are then obtained by transforming the modified Hamiltonian $\eta \mathcal{A}$ with respect to the matrix $T_{\mathbf{k}}$, namely $T_{\mathbf{k}} \eta \mathcal{A}_{\mathbf{k}} T_{\mathbf{k}}^{-1} = \Omega_{\mathbf{k}}$, with

$$\Omega_{\mathbf{k}} = \text{diag}(\omega_{\mathbf{k}}^{(1)}, \dots, \omega_{\mathbf{k}}^{(n)}, -\omega_{\mathbf{k}}^{(1)}, \dots, -\omega_{\mathbf{k}}^{(n)}). \quad (2.14)$$

It shall be useful in the latter to unravel the inner structure of the Bogoliubov matrix, which is separated in $n \times n$ blocks

$$T_{\mathbf{k}} = \begin{pmatrix} U_{\mathbf{k}} & V_{\mathbf{k}}^* \\ V_{\mathbf{k}} & U_{\mathbf{k}}^* \end{pmatrix}, \quad (2.15)$$

which are themselves composed of n column vectors of length n , such that $U_{\mathbf{k}} = (\mathbf{u}_{\mathbf{k}}^{(1)}, \dots, \mathbf{u}_{\mathbf{k}}^{(n)})$ and $V_{\mathbf{k}} = (\mathbf{v}_{\mathbf{k}}^{(1)}, \dots, \mathbf{v}_{\mathbf{k}}^{(n)})$, each encoding the spatial structure over the unit cell of the eigenfunction associated with the couple of quantum numbers (\mathbf{k}, r) . Besides, the expression of the inverse Bogoliubov transformation $T_{\mathbf{k}}^{-1} = \eta T_{\mathbf{k}}^T \eta$ translates into a property of η -orthogonality : $(\mathbf{u}_{\mathbf{k}}^{(r)}, \mathbf{v}_{\mathbf{k}}^{(r)}) \eta (\mathbf{u}_{\mathbf{k}}^{(r')}, \mathbf{v}_{\mathbf{k}}^{(r')}) = \delta_{rr'}$. Once the diagonalization scheme is achieved, one holds the keys to explicitly calculate the equilibrium properties as the dynamics of the β -bosons fields and, applying backwards the Bogoliubov and HP transformations, one can reconstruct the some properties for the spin.

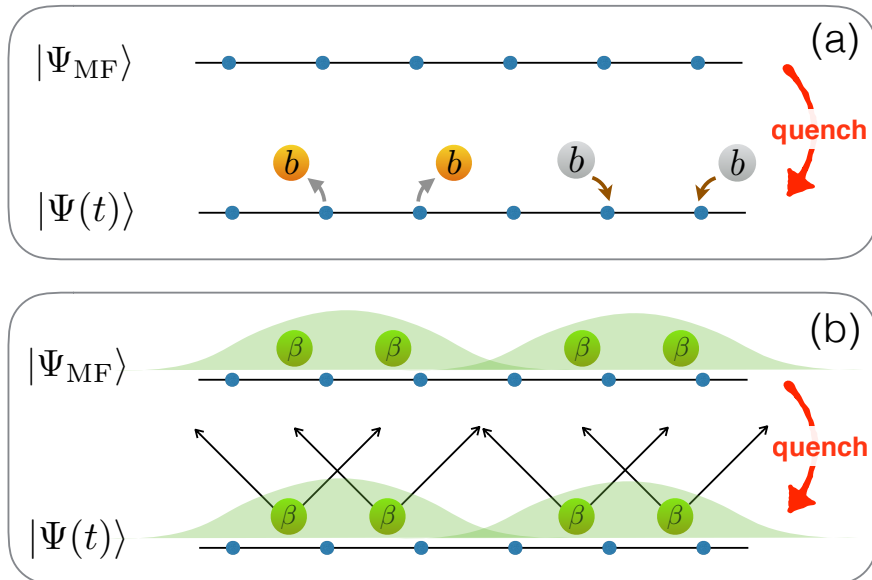


Figure 2.1: b - and β -boson images of dynamics - the upper panel illustrates the spontaneous creation and annihilation of bosonic pairs from the vacuum of excitations (mean-field state). The lower panel represents the same situations from the point of view of a gas of free quasi-particles. At initialization, the system is a combination of coherent states of pairs, the dynamics only ballistically propagating these pairs.

2.1.4 Bosonic Gaussian states

In the following, we shall be mostly concerned with the study of quenches starting from the mean-field state, namely the vacuum of b -bosons. This state has the advantage of being simple and, if it offers a reasonable approximation of the ground state of the evolution Hamiltonian, the dynamics initialized from it is expected to generate a dilute gas of quasiparticles, thereby justifying the linear spin-wave theory approach, as described below. Indeed, due to the pair-creation and annihilation terms $\hat{b}_{l_p}\hat{b}_{l_p'}$ introduced in the Hamiltonian by the $S^{x'}S^{x'}$ couplings, the vacuum of b -bosons is not an eigenstate of the system, and consequently the time evolution results in the spontaneous creation of magnetic excitations as illustrated in the upper panel of Fig.2.1. The resulting density of b -bosons, $r = 1/(2SN) \sum_{l_p} \langle \hat{b}_{l_p}^\dagger \hat{b}_{l_p} \rangle$ is then expected to grow until reaching a finite value at equilibration. The density r quantifies the validity of the dilution hypothesis upon which the linear spin-wave theory stands, thus gauging how reliable its results are. In order to be accurately described by the LSW theory, the spin dynamics shall keep the density at sizably small values

$$r(t) = \frac{1}{2SN} \sum_{l_p} \langle \hat{b}_{l_p}^\dagger \hat{b}_{l_p} \rangle(t) \ll 1. \quad (2.16)$$

On the other hand, β -bosons offer a dual and complementary point of view on the system and its dynamics. While, the mean-field state is devoid of any b -boson, it can be described in terms of β -quasiparticles as a gas of finite and fixed density.

Indeed, the population $\hat{n}_{\mathbf{k},r} = \hat{\beta}_{\mathbf{k},r}^\dagger \hat{\beta}_{\mathbf{k},r}$ of β -bosons at every momentum and for every band is a conserved quantity of the quadratic model used to approximate the system of interest ($[\hat{n}_{\mathbf{k},r}, \hat{\mathcal{H}}] = 0$). In terms of the β -bosons, the mean-field state takes the form of a combination of two-mode squeezed states [15]

$$\begin{aligned} |\Psi_{\text{MF}}\rangle &= \mathcal{N} \exp(-K) |0\rangle_\beta \\ K &= \frac{1}{2} \sum_{\mathbf{k}} \sum_{r,r'} \hat{\beta}_{\mathbf{k},r}^\dagger [(U_{\mathbf{k}}^\dagger)^{-1} V_{\mathbf{k}}^\dagger]_{rr'} \hat{\beta}_{\mathbf{k},r'}, \end{aligned} \quad (2.17)$$

where \mathcal{N} is a normalization factor and $|0\rangle_\beta$ the vacuum of β -quasiparticles, or in other words the ground state of the LSW quadratic Hamiltonian. This image also puts the quench dynamics into another perspective. Indeed, the form taken in Eq.(2.17) by the many-body state, namely a collection of two-mode squeezed states, belongs to a broader family of states dubbed as *Gaussian states* [42]. These states are characterized by their reduced density matrices for any subsystem A , which admit a description in terms of the exponential of an Hermitian quadratic form of bosonic (or fermionic) operators called *entanglement Hamiltonian*,

$$\hat{\rho}_A = \frac{1}{Z} \exp \left[-\frac{1}{2} \sum_{i,j \in A} \left(\hat{b}_i^\dagger \mathcal{A}_{ij} \hat{b}_j + \hat{b}_i \mathcal{B}_{ij} \hat{b}_j + \text{h.c.} \right) \right] = \frac{1}{Z} \exp(-\hat{\mathcal{H}}_E^{(A)}), \quad (2.18)$$

Z being a normalization factor ensuring the property $\text{Tr}[\hat{\rho}] = 1$. One of the main characteristics of Gaussian states is that they can be fully described in terms of their covariance matrix, or in other words by the two-point correlators $G_{ij} = \langle \hat{b}_i^\dagger \hat{b}_j \rangle$ and $F_{ij} = \langle \hat{b}_i \hat{b}_j \rangle$ due to Wick's theorem.

Theorem 1 (Wick). *Let us consider $(\phi_1, \phi_2, \dots, \phi_n)$ an even-numbered set of zero-mean valued bosonic operators ($\phi = b^{(\dagger)}$); the expectation value of their product on a Gaussian state reads*

$$\langle \phi_1 \phi_2 \cdots \phi_n \rangle = \sum_{p \in \mathfrak{P}_n^2} \prod_{\{i,j\} \in p} \langle \phi_i \phi_j \rangle, \quad (2.19)$$

where \mathfrak{P}_n^2 is the ensemble of possible pairing of n elements, while the product runs on all the pair configurations contained in p .

Assuming that the Hamiltonian involved in the unitary evolution of the bosonic operators $\hat{b}_i^{(\dagger)}$ is quadratic, then the evolved form of the operators at any time is a linear combination of the b -operators at $t = 0$, which can be written in a vectorial way as

$$\begin{pmatrix} \mathbf{b}(t) \\ \mathbf{b}^\dagger(t) \end{pmatrix} = \mathcal{U}(t) \begin{pmatrix} \mathbf{b}(0) \\ \mathbf{b}^\dagger(0) \end{pmatrix}, \quad (2.20)$$

where $\mathcal{U}(t)$ is a $2N \times 2N$ time-dependent matrix. Injecting this linear relation into the expression of the entanglement Hamiltonian, one finds that the unitary evolution preserves the Gaussian nature of the state,

$$\mathcal{H}_E(t) = (\mathbf{b}^\dagger(0) \quad \mathbf{b}(0)) \underbrace{\mathcal{U}^\dagger(t) \mathcal{M}(0) \mathcal{U}(t)}_{\mathcal{M}(t)} \begin{pmatrix} \mathbf{b}(0) \\ \mathbf{b}^\dagger(0) \end{pmatrix}, \quad (2.21)$$

where $\mathcal{M}(0)$ is the matrix describing the quadratic form of b -operators at $t = 0$, therefore enabling the application of Wick's theorem at all times, as well as all other properties descending from the Gaussian nature of the state. One of them, being the ability to compute exactly the entanglement entropy of a reduced density matrix.

Similarly to the linear spin-wave theory, the quadratic form encased in the exponential can be diagonalized via an invertible Bogoliubov transformation U in order to obtain a set of eigenvalues ω_α called *entanglement spectrum*

$$\eta \begin{pmatrix} \mathcal{A} & \mathcal{B} \\ \mathcal{B}^* & \mathcal{A}^* \end{pmatrix} = U \begin{pmatrix} \text{diag}(\omega_\alpha) & 0 \\ 0 & -\text{diag}(\omega_\alpha) \end{pmatrix} U^{-1}. \quad (2.22)$$

As the state of the system is fully described by the two-point correlators, one must be able to use the information stored in the covariance matrix to deduce the eigenspectrum. As it shares its eigenbasis with the entanglement Hamiltonian, the covariance matrix can actually be related to the entanglement spectrum by means of the relation

$$\begin{pmatrix} -1 - G^* & F \\ -F^* & G \end{pmatrix} = U \begin{pmatrix} \text{diag}(-1 - n_\alpha) & 0 \\ 0 & \text{diag}(n_\alpha) \end{pmatrix} U^{-1}, \quad (2.23)$$

where the coefficients $n_\alpha = 1/(\exp(\omega_\alpha) - 1)$ are the populations of each entanglement mode of the density matrix [39]. Similarly to thermal entropy of a Bose gas, these bosonic populations can be linked to the entanglement entropy using the relation

$$E_A = \sum_\alpha [(1 + n_\alpha) \ln(1 + n_\alpha) - n_\alpha \ln n_\alpha]. \quad (2.24)$$

The theoretical framework of linear spin-wave theory provides an approximate description of the system in terms of an integrable model with a Gaussian representation of states, leading to a full description of the system in terms of the two-point correlators. However, one should keep in mind that this description in terms of an integrable model is inaccurate at long times, however valid the dilution hypothesis might be. Indeed, the conservation of the integrals of motion constraints the long-time and equilibration dynamics, leading the system toward a pre-thermalized state. Which may not be realized by the exact diagonalization of the system.

2.2 The treatment of non-linearity : the Gaussian Ansätze

2.2.1 Modified spin-wave theory

Linear spin-wave theory relies on the strong assumption that the deviation of the quantum state from the mean-field state is sufficiently weak to justify a linearization of the Holstein-Primakoff transformation. This dilution hypothesis is accurate when the mean-field state is itself a good approximation of the quantum ground state, but breaks down when quantum fluctuations become sizably large, e.g. near quantum critical points at equilibrium. On the other hand, stronger deviations from the mean-field state can be accounted for when dealing with the non-linear terms of the Hamiltonian, something that can be done in an approximate fashion while retaining the Gaussian nature of the states generated by the approach, either at equilibrium as well as away from it. These observations are at the heart of Takahashi's *modified spin-wave theory* (MSW) [92], which provides self-consistent equations for the two-point correlators fully describing the Gaussian state of the system.

In the following, we will outline the reasoning underlying MSW theory for translationally invariant systems at equilibrium, and then discuss its successes and limitations. Let us assume that the density matrix for the state of the system of interest, described by the Hamiltonian $\hat{\mathcal{H}}$, has a general Gaussian structure reading

$$\hat{\rho} = \frac{1}{Z} \exp \left[-\frac{1}{2} \sum_{i,j} \left(\hat{b}_i^\dagger \mathcal{A}_{ij} \hat{b}_j + \hat{b}_i \mathcal{B}_{ij} \hat{b}_j + \text{h.c.} \right) + \sum_i \left(\mathcal{C}_i \hat{b}_i + \text{h.c.} \right) \right]. \quad (2.25)$$

Similarly to LSW theory, by means of a Bogoliubov transformation, the quadratic form can be diagonalized to reconstruct a collection of harmonic oscillators described by operators $\hat{\lambda}_\alpha, \hat{\lambda}_\alpha^\dagger$ associated to eigenvalues ω_α . For systems with translational invariance, the index labelling these modes is represented by the quasi-momentum \mathbf{k} ; the Bogoliubov transformation is then parametrized by an momentum dependent Bogoliubov angle $\theta_{\mathbf{k}}$

$$\begin{cases} \hat{\lambda}_{\mathbf{k}} = \cosh \theta_{\mathbf{k}} \hat{\beta}_{\mathbf{k}} - \sinh \theta_{\mathbf{k}} \hat{\beta}_{-\mathbf{k}}^\dagger \\ \hat{\lambda}_{\mathbf{k}}^\dagger = -\sinh \theta_{\mathbf{k}} \hat{\beta}_{-\mathbf{k}} + \cosh \theta_{\mathbf{k}} \hat{\beta}_{\mathbf{k}}^\dagger \end{cases} \quad (2.26)$$

where we have introduced the shifted operators $\hat{\beta}_{\mathbf{k}} = \hat{b}_{\mathbf{k}} - c_{\mathbf{k}}$, with shifts $c_{\mathbf{k}} = \langle b_{\mathbf{k}} \rangle$ such that the linear part of the Gaussian form vanishes, only leaving the quadratic part. In a state described by the density matrix

$$\hat{\rho} = \frac{1}{Z} \exp \left[-\sum_{\alpha} \frac{\omega_{\alpha}}{T} \hat{\lambda}_{\mathbf{k},\alpha}^\dagger \hat{\lambda}_{\mathbf{k},\alpha} \right], \quad (2.27)$$

where T is the temperature, the population of the mode \mathbf{k} is Bose-Einstein distributed,

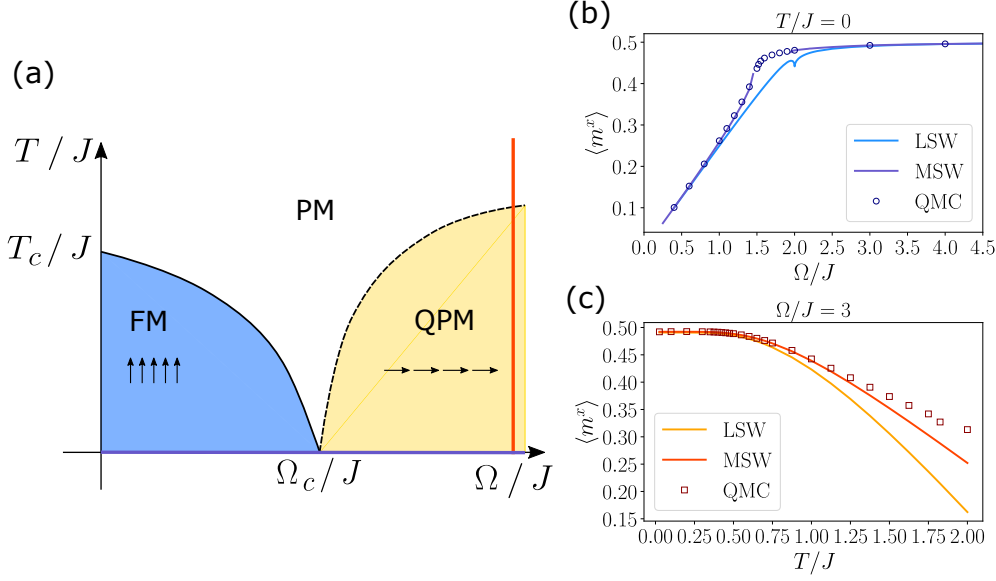


Figure 2.2: Phase diagram of the transverse field Ising model - (a) shows a schematic phase diagram for the ferromagnetic transverse field Ising model, FM standing for ferromagnetic, PM for paramagnetic. The blue and red lines on the figure represent the inserts (b) and (c) which respectively compare MSW results with LSW and quantum Monte-Carlo simulations obtained for a system of size 64×64 .

$$n_{\mathbf{k}} = \langle \hat{\lambda}_{\mathbf{k}}^\dagger \hat{\lambda}_{\mathbf{k}} \rangle = \frac{1}{e^{\omega_{\mathbf{k}}/T} - 1} \quad (2.28)$$

leading to the following expression for the two points correlators C_{ij} and F_{ij}

$$\begin{cases} C_{ij} = \langle \hat{\beta}_i^\dagger \hat{\beta}_j \rangle - \frac{1}{2} \delta_{ij} = \frac{1}{N} \sum_{\mathbf{k}} e^{-i\mathbf{k} \cdot (\mathbf{r}_i - \mathbf{r}_j)} \cosh(2\theta_{\mathbf{k}}) \left(n_{\mathbf{k}} + \frac{1}{2} \right) \\ F_{ij} = \langle \hat{\beta}_i \hat{\beta}_j \rangle = \langle \hat{\beta}_i^\dagger \hat{\beta}_j^\dagger \rangle = \frac{1}{N} \sum_{\mathbf{k}} e^{-i\mathbf{k} \cdot (\mathbf{r}_i - \mathbf{r}_j)} \sinh(2\theta_{\mathbf{k}}) \left(n_{\mathbf{k}} + \frac{1}{2} \right). \end{cases} \quad (2.29)$$

As suggested by Eq.(2.29), all the information on the two-point correlators, and by extension on the Gaussian state, is actually carried by a finite set of independent coefficients $(\theta_{\mathbf{k}}, \omega_{\mathbf{k}}, c_{\mathbf{k}})$. One can reconstruct the equilibrium of the system in a variational fashion by treating the Bogoliubov angles, the eigenfrequencies and the operator shift as variational parameters for the Gaussian state. As the system is put into contact with a thermal bath at temperature T , the variational principle that must be satisfied by the Gaussian state is the minimization of the free energy $\mathcal{F} = \langle \hat{\mathcal{H}} \rangle - TS$, where S is the thermodynamic entropy defined for bosonic systems as $S = \sum_{\mathbf{k}} (1 + n_{\mathbf{k}}) \ln(1 + n_{\mathbf{k}}) - n_{\mathbf{k}} \ln n_{\mathbf{k}}$. The Gaussian nature of the state becomes central at this point, as it enables the use of Wick's theorem, reducing the expectation value of $\hat{\mathcal{H}}$ to a function of the two-point correlators even when including arbitrary non-linearities in the Hamiltonian. As a consequence, the equations for the $(\theta_{\mathbf{k}}, \omega_{\mathbf{k}}, c_{\mathbf{k}})$ parameters defining the minimum of the free

energy are non-linear, but they can be generally solved in a self-consistent manner. We remind that in the context of diluted Bose gases, this Gaussian approach is also well known as the Hartree-Fock-Bogoliubov theory [44].

An example of implementation of the MSW theory is shown in Fig. 2.2 in the case of the ferromagnetic transverse-field Ising model on the square lattice, whose Hamiltonian is expanded up to the quartic order in terms of the b -operators. The field-induced magnetization obtained using LSW and MSW theories is compared with results obtained via quantum Monte-Carlo simulations along two lines of the phase diagram (Fig. 2.2 (a)): at constant temperature $T/J = 0$ (blue) and at fixed field $\Omega/J = 3$ (red). We can see that although modified spin-wave theory sizeably improves the results of the linear spin-wave approach and compares well with the numerical simulation, especially on Fig. 2.2 (c), it still fails to grasp the physics of the system in the vicinity of the quantum critical point (located in Fig. 2.2 at $\Omega_c/J \simeq 1.522$), since the self-consistent equations do not admit a solution in the range $1.5 \lesssim \Omega \lesssim 2$. This numerical instability of equations is caused by the emergence of imaginary parts in the frequencies $\omega_{\mathbf{k}}$ and are a signature of strong quantum fluctuations that escape the description provided by a self-consistent harmonic approximation [46].

2.2.2 Dynamical Gaussian Ansatz

The improvement brought to LSW theory by the extension of the Gaussian description of spins beyond the linearization regime leads us to implement the same type of approach to the dynamics of quantum many-body systems. The Gaussian Ansatz is also especially relevant as it enables to deal with the infinite hierarchy of correlation functions in interacting systems.

Bogoliubov-Born-Green-Kirkwood-Yvon hierarchy – Let us consider a bosonic Hamiltonian written as the sum of quadratic and quartic forms of bosonic operators $\hat{\mathcal{H}} = \hat{\mathcal{H}}^{(2)} + \hat{\mathcal{H}}^{(4)}$. In general, the expectation value of any observables, expressed in terms of bosonic operators, can be generically written as a combination of n -point correlators, the simplest ones being the two-point correlators. In the Heisenberg picture of quantum mechanics, the evolution of operators is dictated by the Heisenberg equation. The equation of motion for the two-point correlators $\langle \hat{b}_i^\dagger \hat{b}_j \rangle$ reads

$$i \frac{d}{dt} \langle \hat{b}_i^\dagger \hat{b}_j \rangle = \underbrace{\langle [\hat{b}_i^\dagger \hat{b}_j, \hat{\mathcal{H}}^{(2)}] \rangle}_{f^{(2)}(C^{(2)})} + \underbrace{\langle [\hat{b}_i^\dagger \hat{b}_j, \hat{\mathcal{H}}^{(4)}] \rangle}_{f^{(4)}(C^{(4)})}, \quad (2.30)$$

where the $f^{(n)}$ functions are linear combinations of n -point correlators noted $C^{(n)}$. We should particularly stress that this expression involves correlation functions of higher order, and that consequently the dynamics of two-point correlators is coupled to the evolution of four-point correlators. Writing down the equation of motion for the four-point correlators, one can notice that new correlators of higher degree appear. We can then deduce that, for interacting systems, the

dynamics of n -point correlators is described by an infinite set of first-order linear differential equations,

$$\begin{aligned}\frac{d}{dt}C^{(2)} &= \mathcal{F}^{(2)}(\{C^{(2)}\}, \{C^{(4)}\}) \\ \frac{d}{dt}C^{(4)} &= \mathcal{F}^{(4)}(\{C^{(4)}\}, \{C^{(6)}\})\end{aligned}\tag{2.31}$$

$$\frac{d}{dt}C^{(6)} = \mathcal{F}^{(6)}(\{C^{(6)}\}, \{C^{(8)}\})\tag{2.32}$$

⋮

where $\mathcal{F}^{(n)}$ are linear functions of the correlators. This set of linear differential equations is generally called *Bogoliubov-Born-Green-Kirkwood-Yvon (BBGKY) hierarchy* and its infinite structure reflects the difficulty of studying the dynamics of correlations in interacting systems.

Dynamical Gaussian Ansatz – Similarly to modified spin-wave theory, we propose to overcome the problem of the BBGKY hierarchy by assuming that the quantum many-body state of the system is Gaussian, allowing for the application of Wick’s theorem. The high-order correlators can then be split into products of two-point correlators, which then provide a full description of the physics of the system of interest, and lead to a truncation of the BBGKY hierarchy to the lowest order.

Let us now consider an arbitrary bosonic Hamiltonian $\hat{\mathcal{H}}$. Assuming that the quantum state can be described according to the form given in Eq.(2.25) the Heisenberg equations for the mean-field $\langle \hat{b}_i \rangle = c_i$ and the two-point correlators $G_{ij} = \langle \hat{\beta}_i^\dagger \hat{\beta}_j \rangle$ and $F_{ij} = \langle \hat{\beta}_i \hat{\beta}_j \rangle$ result in a closed set of non-linear coupled differential equations

$$\begin{aligned}\frac{d}{dt}c_i &= i\langle [\hat{\mathcal{H}}, \hat{b}_i] \rangle = \mathcal{J}_i(\{c_i\}, \{G_{ij}\}, \{F_{ij}\}) \\ \frac{d}{dt}G_{ij} &= i\langle [\hat{\mathcal{H}}, \hat{\beta}_i^\dagger \hat{\beta}_j] \rangle = \mathcal{G}_{ij}(\{c_i\}, \{G_{ij}\}, \{F_{ij}\}) \\ \frac{d}{dt}F_{ij} &= i\langle [\hat{\mathcal{H}}, \hat{\beta}_i \hat{\beta}_j] \rangle = \mathcal{F}_{ij}(\{c_i\}, \{G_{ij}\}, \{F_{ij}\}).\end{aligned}\tag{2.33}$$

The first equation of this set describes the dynamics of the mean-field c_i , and it plays the same role as the Gross-Pitaevski equation in the theory of the dilute Bose gases. Yet, within the Gaussian Ansatz the mean-field dynamics is coupled to that of the two-point correlators, as in Hartree-Fock-Bogoliubov theory.

The dynamical Gaussian Ansatz offers an effective approach for the study of dynamical phenomena that exceed the scope of linear spin-wave theory, with applications to the physics of spin systems related to the current capabilities of quantum simulators.

2.3 Fermionic Gaussian states

2.3.1 Spin-fermion projection

So far, we have seen how the physics of quantum spins could be projected onto a bosonic image with an imposed constraint on the dimension of the local Fock space. In particular, in the case where $S = 1/2$, the spin excitations map onto a gas of hardcore bosons. In the following we shall consider an alternative mapping of spins onto (spinless) fermions, which becomes particularly convenient in one spatial dimension as it can map strongly interacting spin models onto models of free fermions.

Jordan-Wigner transformation – For a $S = 1/2$ spin chain, one can easily establish a correspondance between the local Hilbert space of a spin and that of a fermionic mode f ,

$$|\uparrow\rangle \leftrightarrow |0\rangle, \quad |\downarrow\rangle \leftrightarrow \hat{f}^\dagger|0\rangle. \quad (2.34)$$

However, the fermionic anticommutation relations between different sites are not compatible with the spin algebra, and to fix this inconsistency one shall attach a non-local phase factor to every fermionic operators in order to reproduce spin operators:

$$\hat{S}_i^- = \hat{f}_i^\dagger e^{i\phi_i}, \quad (2.35)$$

where the phase factor is called string operator, and contains the sum of the fermionic populations to the left of the i -th site,

$$\phi_i = \pi \sum_{k < i} \hat{n}_k. \quad (2.36)$$

The full spin-fermion transformation, or so-called *Jordan-Wigner transformation* [56], then provides expressions of the spin operators in terms of fermionic operators,

$$\begin{aligned} \hat{S}_i^z &= \frac{1}{2} - \hat{f}_i^\dagger \hat{f}_i \\ \hat{S}_i^+ &= e^{-i\pi \sum_{k < i} \hat{n}_k} \hat{f}_i \\ \hat{S}_i^- &= \hat{f}_i^\dagger e^{i\pi \sum_{k < i} \hat{n}_k}. \end{aligned} \quad (2.37)$$

The transverse-field Ising chain – Let us consider a set of N spins arranged in a chain and coupled to a magnetic field whose orientation is orthogonal to the direction set by the Ising coupling of spins. Choosing the direction of the magnetic field as the quantization axis, the Hamiltonian reads

$$\hat{\mathcal{H}} = -J \sum_i \hat{S}_i^x \hat{S}_{i+1}^x - \Omega \sum_i \hat{S}_i^z, \quad (2.38)$$

which can be equivalently written as

$$\hat{\mathcal{H}} = -\frac{J}{4} \sum_i \left(\hat{S}_i^- \hat{S}_{i+1}^+ + \hat{S}_i^+ \hat{S}_{i+1}^- + \text{h.c.} \right) - \Omega \sum_i \hat{S}_i^z. \quad (2.39)$$

The implementation of the Jordan-Wigner transformation leads to a free-fermion representation of the system, due to the cancellation of the string operator in the case of the nearest-neighbour Ising couplings. The Hamiltonian can then be written as a quadratic form of fermionic operators,

$$\hat{\mathcal{H}} = -\frac{J}{4} \sum_i \left(\hat{f}_i^\dagger \hat{f}_{i+1} + \hat{f}_{i+1}^\dagger \hat{f}_i + \hat{f}_i^\dagger \hat{f}_{i+1}^\dagger + \hat{f}_{i+1} \hat{f}_i \right) - \Omega \sum_i \left(\frac{1}{2} - \hat{f}_i^\dagger \hat{f}_i \right), \quad (2.40)$$

which in Fourier space takes the form

$$\hat{\mathcal{H}} = \frac{1}{2} \sum_k \begin{pmatrix} \hat{f}_k^\dagger & \hat{f}_{-k} \end{pmatrix} \begin{pmatrix} \xi_k & i\zeta_k \\ -i\zeta_k & -\xi_k \end{pmatrix} \begin{pmatrix} \hat{f}_k \\ \hat{f}_{-k}^\dagger \end{pmatrix}, \quad (2.41)$$

where $\xi_k = -(J/2) \sin k - \Omega$ and $\zeta_k = (J/2) \sin k$. Similarly to the bosonic case, quadratic forms of fermionic operators can be readily diagonalized via a Bogoliubov transformation which preserves the fermionic anticommutation relations [3]

$$\begin{pmatrix} \hat{\eta}_k \\ \hat{\eta}_k^\dagger \end{pmatrix} = \begin{pmatrix} \cos \theta_k & \sin \theta_k \\ \sin \theta_k & -\cos \theta_k \end{pmatrix} \begin{pmatrix} \hat{f}_k \\ \hat{f}_k^\dagger \end{pmatrix}. \quad (2.42)$$

Under this transformation, the Hamiltonian takes a diagonal form in terms of a fermionic gas of quasiparticles [74]

$$\hat{\mathcal{H}} = \sum_k \omega_k \left(\hat{\eta}_k^\dagger \hat{\eta}_k - \frac{1}{2} \right) \quad (2.43)$$

where the spectrum $\omega_k = \Omega \sqrt{1 + \lambda^2 - 2\lambda \cos k}$ and $\lambda = J/(2\Omega)$, also leading to an analytical expression for the matrix elements of the Bogoliubov transformation,

$$\begin{cases} \cos \theta_k = \sqrt{\frac{1}{2} \left(1 + \frac{\xi_k}{\omega_k} \right)} \\ \sin \theta_k = \sqrt{\frac{1}{2} \left(1 - \frac{\xi_k}{\omega_k} \right)} \end{cases}, \quad (2.44)$$

therefore providing full access to any spin observable or correlation function expressed in terms of the Jordan-Wigner fermions.

2.3.2 Fermionic Gaussian Ansatz

From the perspective of the fermionic η -quasiparticles, the vacuum of the Jordan-Wigner fermions is a BCS state, namely a fermionic two-mode coherent state

$$|0\rangle_f = \mathcal{N} \prod_k \left[1 + \cotan(\theta_k) \hat{\eta}_k^\dagger \hat{\eta}_{-k}^\dagger \right] |0\rangle_\eta \quad (2.45)$$

$$= \mathcal{N} \prod_k \exp[\cotan(\theta_k) \hat{\eta}_k^\dagger \hat{\eta}_{-k}^\dagger] |0\rangle_\eta, \quad (2.46)$$

which also admits a description in terms of a Gaussian state. The whole reasoning we developed for bosonic Gaussian states holds as well as their fermionic counterpart: at all times, a Gaussian fermionic state evolved by a quadratic Hamiltonian remains Gaussian. Moreover, the covariance matrix fully characterizes the system, and in particular entanglement entropy can be extracted from its eigenvalues,

$$\begin{pmatrix} 1 - G^* & F \\ -F & G \end{pmatrix} = U \begin{pmatrix} \text{diag}(1 - n_\alpha) & 0 \\ 0 & \text{diag}(n_\alpha) \end{pmatrix} U^{-1}, \quad (2.47)$$

where the occupancy of the corresponding eigenmode $n_\alpha = 1/(\exp(\omega_\alpha) + 1)$ is Fermi-Dirac distributed and leads to the form

$$E_A = - \sum_\alpha [(1 - n_\alpha) \ln(1 - n_\alpha) + n_\alpha \ln n_\alpha]. \quad (2.48)$$

If the Ising chain in a transverse field maps into a model of fermions, other spin models such as the XXZ chain map onto a problem of interacting fermions with a quartic Hamiltonian,

$$\hat{\mathcal{H}} = - \sum_i \frac{J}{2} \left(\hat{f}_i^\dagger \hat{f}_{i+1} + \hat{f}_{i+1}^\dagger \hat{f}_i \right) + J_z \left(\frac{1}{4} - \hat{f}_i^\dagger \hat{f}_i + \hat{f}_i^\dagger \hat{f}_i \hat{f}_{i+1}^\dagger \hat{f}_{i+1} \right). \quad (2.49)$$

In order to investigate dynamical properties of these cases, we propose to extend the Gaussian Ansatz to treat the case of interacting fermionic systems similarly to what is done for non-linear bosonic Hamiltonians. Under the assumption that the system can be described in terms of a fermionic Gaussian state, all information on the many-body state is contained into the mean-field value of the fermionic operators $\phi_i = \langle \hat{f}_i \rangle$ and the two-point correlators. Defining the shifted fermionic operators as $\hat{\gamma}_i = \hat{f}_i - \phi_i$, the elements of the covariance matrix $G_{ij} = \langle \hat{\gamma}_i^\dagger \hat{\gamma}_j \rangle$ and $F_{ij} = \langle \hat{\gamma}_i \hat{\gamma}_j \rangle$, these quantities obey the same type of equations as Eq. (2.33),

$$\begin{aligned} \frac{d}{dt} \phi_i &= i \langle [\hat{\mathcal{H}}, \hat{f}_i] \rangle = \mathcal{J}_i(\{\phi_i\}, \{G_{ij}\}, \{F_{ij}\}) \\ \frac{d}{dt} G_{ij} &= i \langle [\hat{\mathcal{H}}, \hat{\gamma}_i^\dagger \hat{\gamma}_j] \rangle = \mathcal{G}_{ij}(\{\phi_i\}, \{G_{ij}\}, \{F_{ij}\}) \\ \frac{d}{dt} F_{ij} &= i \langle [\hat{\mathcal{H}}, \hat{\gamma}_i \hat{\gamma}_j] \rangle = \mathcal{F}_{ij}(\{\phi_i\}, \{G_{ij}\}, \{F_{ij}\}), \end{aligned} \quad (2.50)$$

with the notable difference that the decomposition of the n -point correlators follows the prescription of the fermionic Wick's theorem [34].

2.4 Conclusion

In this chapter, we reviewed a semi-classical approach to the physics of quantum spin systems based on a linearized bosonic field theory of the quantum fluctuations around the mean-field approximation. This method, the so-called linear spin-wave theory, is limited to regimes in which the fluctuations are sufficiently weak to allow one to neglect the interactions of the bosonic field. Modified spin-wave theory, introduced by Takashi, allows one to include the effects of non-linearities in the study of low-temperature thermodynamics by using a Gaussian Ansatz for the study of non-equilibrium dynamics, leading to a set of coupled non-linear equations for the evolution of the mean field and of two-points correlation functions. Such an approach can be applied to both bosonic as well as fermionic models onto which one can map quantum spin Hamiltonians.

In the next chapters, we will use these Gaussian approaches to explore the dynamics of spins systems, first in regimes where the linear spin-wave theory is sufficient to disclose exotic dynamical phenomena. Then we will apply the Gaussian Ansatz to investigate strongly quenched regimes where the linearized approach to dynamics does not provide a valid image any more.

Dynamics of flat-band systems

*”Ils vont, de l’aube au soir, faire éternellement
Dans la même prison le même mouvement.”*

Victor Hugo, ”Melancholia”, *Les Contemplations*

3.1 Flat-bands of excitations

3.1.1 Band flatness and Aharonov-Bohm caging

The concept of flat-band systems originates from the work of Sutherland [88] on tessellations of the two-dimensional plane, and especially on the so-called dice lattice. He noticed that a tight-binding model cast on such a geometry results in the emergence of a *flat band* of excitations, namely a band of constant energy over the whole Brillouin zone. Shortly after Lieb [57] showed that, at half-filling, the Hubbard model on systems with chiral flat bands of excitations could exhibit ferrimagnetic order, such as in the dice lattice or in the so-called Lieb lattice. The latter work of Mielke and Takasaki [93] extended the results of Lieb to other lattice structures with flat-bands, leading to a burst of new possible structures in one or two dimensions (diamond chain, stub lattice, kagome lattices among others). Perfect flatness however is often a fine-tuned effect that does not survive to the introduction of perturbations as the band then acquires a slight width. This leads us to formulate a less restrictive definition of flat-band systems as systems exhibiting a band whose width is much smaller than that of the other dispersive bands of the spectrum. A direct consequence of band flatness is the (nearly) vanishing group velocity attached to the propagation of these excitations, and consequently their apparent localization at sufficiently short time scales (or at any time scale for perfectly flat bands).

Several mechanisms can explain the emergence of band flatness. Perfectly flat bands can indeed appear for some geometries in the spectrum of the π -flux Harper-Hofstadter model describing a particle on a lattice subjected to an external magnetic field [94]. In some periodic structure such as the dice lattice, the

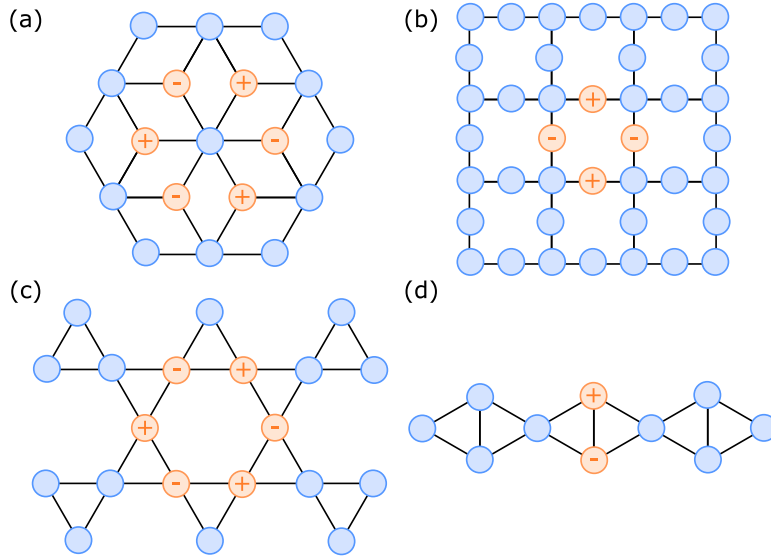


Figure 3.1: Examples of geometries exhibiting Aharonov-Bohm caging - (a) Dice lattice, (b) Lieb lattice, (c) kagome lattice, (d) diamond ladder. The sites colored in orange represent the support of a caged states, while the + and - signs indicate the local sign of the wavefunction.

application of a magnetic flux induces destructive interference effects that trap excitations in a spatially restricted eigenmode, and therefore leads to localization. This effect, known as *Aharonov-Bohm caging*, is exhibited by several lattice structures and it can be either seen as the effect of a magnetic flux threading the lattice, or, under a suitable gauge transformation of a phase pattern exhibited by a localized wavefunction, which even in the absence of a magnetic flux, prevents it from spreading through the lattice under the effect of hopping - Fig. 3.1 providing some illustrative examples of such localized eigenmodes without magnetic field. One can observe on every example a common feature of the wave function, namely the alternation between positive and negative weights, all with the same amplitude. As a result, every neighbouring site of the caged mode is connected to

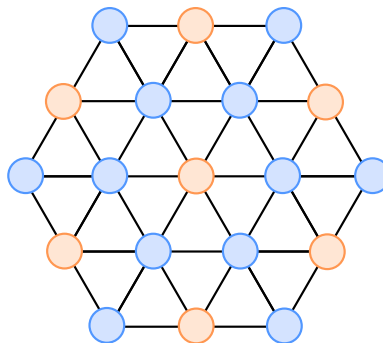


Figure 3.2: The triangular lattice can be separated into two sublattices, a connected lattice (blue) labeled A and a disconnected one (orange) labeled B . If an energy offset is imposed between the sublattices A and B , then the off-resonant propagation of excitations between the sites of B leads to a nearly flat band.

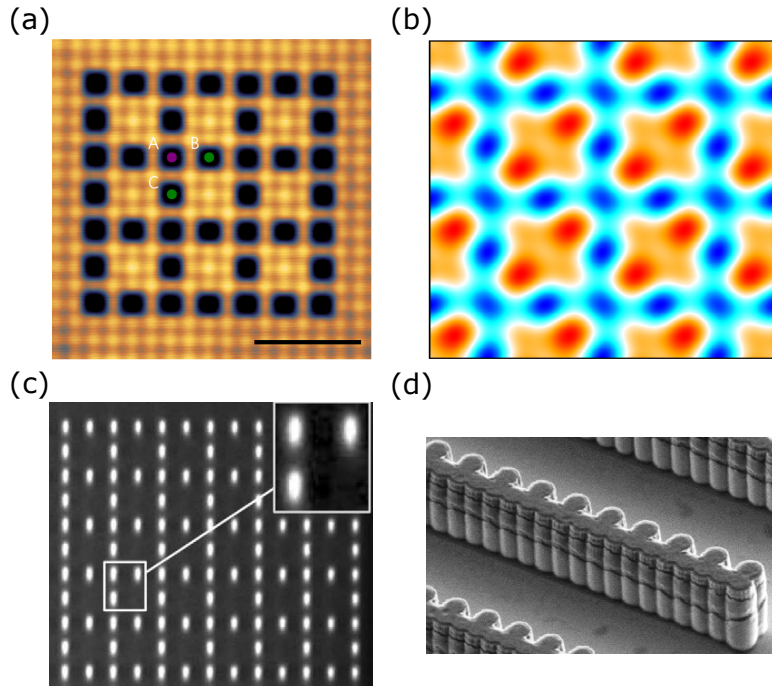


Figure 3.3: Examples of the realizations of Lieb lattices with quantum simulators - (a) Lieb lattice realized with an artificial atomic lattice, (b) Interference pattern of an optical Lieb lattice realized using several laser sheets, (c) Assembly of waveguides engraved in the shape of a Lieb lattice, (d) one-dimensional Lieb lattice (or stub lattice) realized with a chain of coupled micropillar quantum cavities.

as many positively as negatively valued sites, leading to a destructive interference that prevents the localized wavefunction from spreading to the rest of the system.

On the other hand, an imperfect flatness can emerge from a lattice in which an energetic offset is imposed between two sublattices as illustrated in Fig. 3.2 for the case of the triangular lattice: the first sublattice hosts strongly dispersive eigenmodes, as its sites form a connected network. The second sublattice, however, is disconnected and, as a consequence of the energy off-set, supports weakly dispersive modes that need to overcome the energy off-set and go through the dispersive sublattice in order to propagate from one site to another. As we will discuss in Sec. 3.2.2, the off-resonant motion of the modes between sublattices leads to a very weak dispersion of the corresponding band.

3.1.2 From models to experiments

Flat-bands of excitations motivated the engineering of several experimental set-ups using different quantum simulation platforms to capture signatures of their peculiar band structure. Four experimental realizations of the Lieb lattice are shown on Fig. 3.3, each using a different platform. The first displayed example is the reconstruction proposed by Drost & al. [30] of an artificial atomic lattice by creating vacancies in a monolayer of chlorine set on a copper substrate. The

electrons trapped in the vacancies can then tunnel from one site to a neighbouring one similarly to a tight-binding model, in a direct implementation to the model historically proposed by Lieb. The second method shown relies on the protocol of Taie & al. [91] to engineer a Lieb optical lattices that can latter hold laser-cooled atoms, simulating a Bose-Hubbard model on a flat-band geometry with the purpose to study the dynamics of localized states. The physics of the Lieb lattice was also explored in the context of photonic lattices [67]: light is injected in a periodic arrangement of optical waveguides engraved in a host material, and can hop from one to another as it ballistically propagates along the waveguides. For weak couplings between the waveguides, the system can be mapped on a tight-binding model where the propagation axis acts as the time-dimension, thus providing yet another platform for the implementation of the Lieb lattice and the study of its localized modes. The last experimental platform represented on Fig. 3.3 simulates a one-dimensional equivalent of the Lieb lattice (the stub lattice) for exciton-polariton in semiconductor cavities [9]. Each site of the lattice is a micropillar consisting of a quantum well embedded in an optical cavity, the coupling between these micropillars enables a description in terms of a tight-binding model, with the additional possibility to probe the amplitude and phase of the polaritons on each site by photoluminescence imagery.

Due to the modulability of their geometries, Rydberg-atom simulators provide a new experimental platform for the study of flat-band systems in general, yet in models that differ from the tight-binding one. In the following we will discuss the influence of flat bands of excitations in the dynamics of spin models accessible to Rydberg-atom simulators, and propose diagnostic tools to probe the properties of localized modes. For this purpose, we will focus our interest on models illustrating the two aforementioned possible mechanisms for the emergence of flat bands: either by imposing an energy offset between two sublattices, or by Aharonov-Bohm caging.

3.2 Geometric frustration : the triangular lattice

3.2.1 Ground-state degeneracy

The first case we shall consider in our exploration of the physics of flat-band systems is the transverse-field Ising model on a triangular lattice with antiferromagnetic nearest-neighbours couplings, a model notorious for being the prototype of *frustrated systems*. Frustration is the impossibility for a physical system to simultaneously minimize the interaction energy within each pair of interacting degrees of freedom, resulting from the competition between all the involved interactions. In the triangular lattice, this competitive effect stems for the anti-ferromagnetic nature of Ising interactions, that require the spins on neighbouring sites to have antiparallel orientation in order to be minimized. This condition however cannot be simultaneously satisfied by all spins on a triangular plaquette, leading to frustration on the triangular lattice. A similar situation is also

featured by other two-dimensional lattice geometries, such as the kagome lattice, or the checkerboard lattice [47].

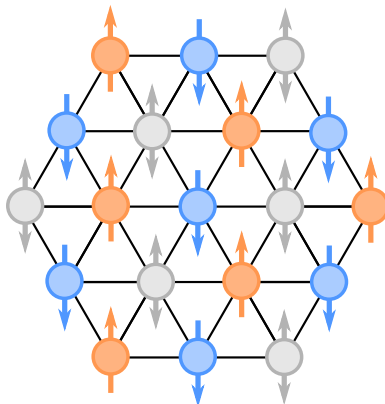


Figure 3.4: Frustrated antiferromagnetic Ising model on the triangular lattice - Once opposite spin orientations has been fixed in the blue and orange sites, the spins on the grey sites can be oriented arbitrarily.

Among the intriguing features displayed by the physics of frustrated systems, a remarkable one is the large degeneracy of the ground state, which may even become macroscopic, leading to a finite entropy per spin even at zero temperature, as observed by Wannier [100] for the antiferromagnetic Ising model on the triangular lattice. The construction of spin configurations in the degenerate ground-state manifold obeys a simple constraint, the so-called *up-down rule*: every triangular plaquette of the lattice should have at least one spin oriented along the up-direction and one along the down-direction, while the orientation of the third one is left undetermined. Through this construction, some spins are surrounded by an equal number of up- and down-oriented nearest neighbours, with the consequence that the local mean field felt by these sites is vanishing. These spins, which occupy a finite fraction of the lattice, can be flipped without any energy cost, leading to an exponential degeneracy of the ground state.

An example of such partial magnetic tiling of the triangle lattice with the up- and down-oriented spins with respect to the up-down rule is provided on Fig. 3.4. One can observe that the sites with a local arbitrary spin orientation occupy a finite fraction ($N/3$) of the system. As for each of these sites two spin configurations are possible, the total degeneracy of the states of this kind amounts to $2^{N/3}$, providing a lower bound for the total degeneracy and consequently to the microcanonical entropy as $S/N = \ln 2/3 \approx 0.231$. The actual ground-state entropy is much larger, $S/N = 0.3383$. This degeneracy is actually problematic for a theoretical study of the quantum antiferromagnetic triangular lattice. Indeed, the linear spin-wave theory as we described it in the previous chapter relies on the existence of a well-defined mean-field image for the ground state to set the foundations of a description of spins in terms of linear quantum fields. Degeneracy prevents this construction by offering an exponential number of possible mean-field spin states. Therefore, the construction of the linear-spin wave theory

for the antiferromagnetic triangle lattice requires the degeneracy to be lifted and an unambiguous mean-field state to be selected in the ground-state manifold.

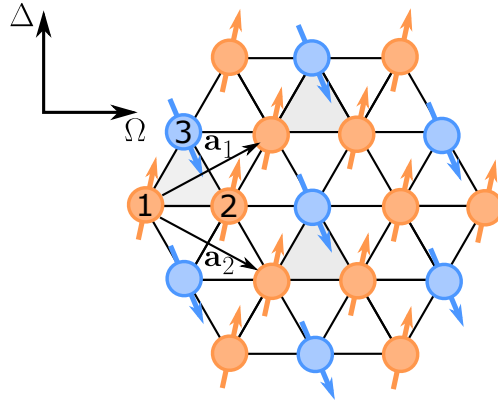


Figure 3.5: State selected by the order-by-disorder mechanism on the triangle lattice - the unit cell of the long-range ordered system is represented in grey while its different elements are labeled 1, 2, 3. The vectors \mathbf{a}_1 and \mathbf{a}_2 stand for the unit vectors of the lattice.

The application of a transverse field is expected to induce a selective mechanism in the ground-state manifold which lifts the degeneracy according to an effect dubbed as *order by disorder* by Villain [96]. This seemingly paradoxical effect consists of an energy selection of the ground-state configurations that are connected to the largest possible number of equally degenerate ground states via elementary transformations (namely spin flips). The addition of a transverse-field term $-\Omega \sum_i \hat{S}_i^x$ acts on the spins by flipping their orientation, therefore it induces a selection of the configurations in the ground-state manifold according to their "flippability", namely the number of spins they possess that can be flipped without any energetic cost. As shown on Fig. 3.4 all spins surrounded by as many up- as down-oriented spins are flippable; yet choosing the orientation of flippable spins carefully, namely choosing them to point up in Fig. 3.4, makes all the other up spins flippable as well, leading to the largest possible fraction ($2/3$) of flippable spins. This argument suggests that an ordered configuration with $\uparrow\uparrow\downarrow$ (or respectfully $\downarrow\downarrow\uparrow$) unit cell is energetically favoured by the transverse field, leading to long-range order, as shown by Moessner and Sondhi [66]. The ordered nature of the ground state (Fig. 3.5) in a finite but moderate transverse field is manifested by the structure factor, showing Bragg peaks at wave-vectors $\mathbf{k} = (\frac{4\pi}{3}, 0)$ and $\mathbf{k} = (\frac{2\pi}{3}, \frac{2\pi}{\sqrt{3}})$.

The lifting of degeneracy from the application of a transverse magnetic field and the resulting emergence of long-range order in the antiferromagnetic triangle lattice seems to be a good starting point for the application of linear spin-wave theory and to investigate the effects of frustration on the elementary excitations. However, as the calculation unfolds, one can notice that for all values of the field Ω the linear spin-wave theory breaks down as it predicts that the lowest band of the excitation spectrum contains imaginary frequencies, actually revealing an

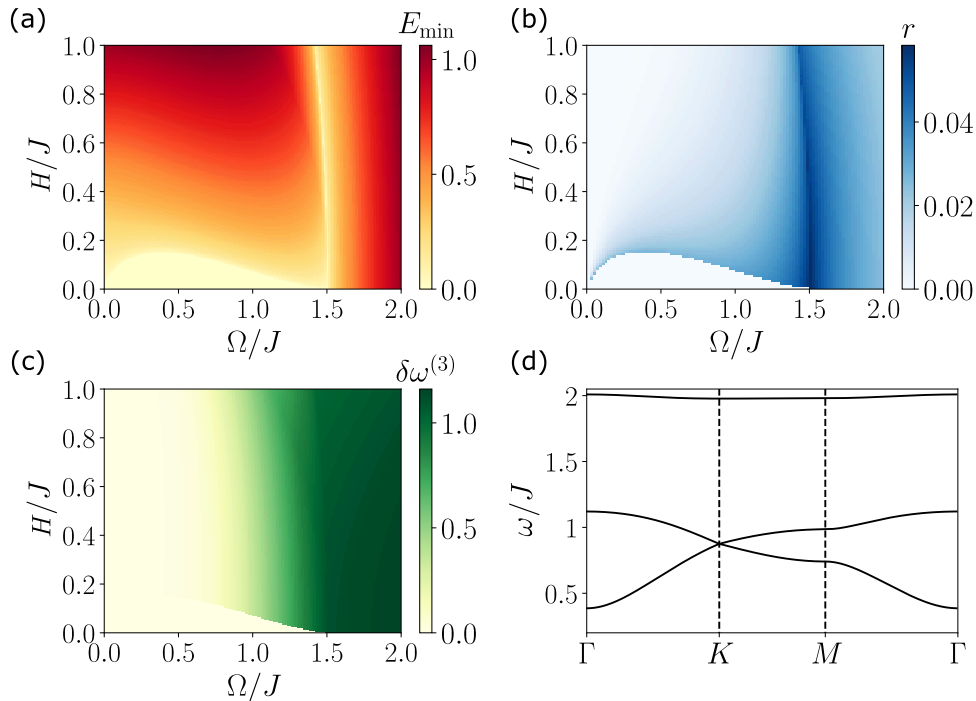


Figure 3.6: Spectral properties of the antiferromagnetic TFIM on a triangle lattice - (a) Lowest energy of the first band of the spectrum computed over the $(\Omega/J, H/J)$ plane. The vanishing of E_{\min} indicates a phase transition, or the emergence of imaginary frequencies in the spectrum. (b) Density of excitations r . (c) Width of the upper band of the spectrum $\delta\omega^{(3)}$. (d) Excitation spectrum of the TFIM on a triangular lattice computed for the set of parameters $(\Omega/J = 0.6, H/J = 0.3)$.

instability of the quasi-particle picture. The breakdown of LSW theory also reveals that the ground state selected by the order-by-disorder mechanism exhibits strong fluctuations that cannot be properly captured by a harmonic approximation. This problem can be addressed by adding a longitudinal field $-H \sum_i \hat{S}_i^z$, which partially lifts the ground-state degeneracy in favour of the spin configurations with two up-oriented spins per unit cell (if $H > 0$) and stabilizing the linear spin-wave theory on a model relevant for Rydberg-atom simulators.

3.2.2 Spectral properties

In the following we shall develop linear spin-wave theory for the Ising antiferromagnet on the triangular lattice in a longitudinal and transverse field with Hamiltonian

$$\hat{\mathcal{H}} = J \sum_{\langle i,j \rangle} \hat{S}_i^z \hat{S}_j^z - \Omega \sum_i \hat{S}_i^x - H \sum_i \hat{S}_i^z \quad (3.1)$$

As we have just discussed, the application of the magnetic fields stabilizes a three-fold degenerate ground state for the antiferromagnetic Ising model, enabling a reliable application of the linear spin wave theory. One can quantify the validity

of the LSW theory with two indicators: the spectral gap of the lowest band of the spectrum, namely the lowest energy level of the excitation spectrum; and the density r of the magnetic excitations predicted by the linear spin-waves theory in the ground state. The vanishing of the spectral gap in the model at hand is accompanied by the appearance of imaginary energies in the spectrum; moreover the density of excitations in the ground state must be sufficiently low to trust their treatment as non-interacting quasi-particles, at the heart of the linear spin-waves approach.

The spectral gap $E_{\min} = \min \omega_{\mathbf{k}}^{(1)}$ and the excitation density r as a function of the fields $(\Omega/J, H/J)$ plane are plotted in Fig. 3.6 (a) and (b). One can observe that the spectrum displays a gap as it is expected from the excitations of a system that breaks discrete symmetries, which is a first consistency test for the LSW prediction. However, the gap closes and imaginary frequencies appear for a sufficiently small longitudinal and transverse field -in particular for all $\Omega \leq \Omega_c = 1.5J$ and $H = 0$, where Ω_c is the critical field (within the mean-field approximation) for the transition between long-range order and quantum paramagnetism. As for the ground-state density of excitations $r = 1/(2SN) \sum_{\mathbf{k},r} |\mathbf{v}_{\mathbf{k}}^{(r)}|^2$ whose expression involves the Bogoliubov vectors of the LSW theory, it remains at a sizeably weak value except at the boundaries of the instability area, and at the transition line with the paramagnetic state, therefore ensuring the validity at equilibrium of the linear spin-wave construction. The actual transition point is at $\Omega_c \approx 0.82J$ [52] as predicted by quantum Monte Carlo simulations. The mean-field prediction $\Omega = 1.5J$ is highly inaccurate, and linear spin-wave theory corrections do not shift this value significantly, showing that the linearization of fluctuations around the mean-field state is a rough approximation at sufficiently strong transverse fields. Therefore in the following we shall stay away from this regime as well.

The boundaries of the explorable set of parameters being defined, we shall examine the spectral properties of the excitations, as predicted by the LSW formalism. The LSW spectrum exhibits two low-lying bands touching at Dirac cones and a single branch lying at higher energies, which is nearly flat compared to the width of the two other bands, as illustrated on Fig. 3.6(d). The flatness of the high energy band is a robust property that characterizes it on a large range of parameters inside the stability domain of the LSW theory. The band structure of the spin excitations can be understood by inspecting the associated eigenmodes at any given wavevector \mathbf{k} encoded in the Bogoliubov vectors $\mathbf{u}_{\mathbf{k}}^{(r)}$ and $\mathbf{v}_{\mathbf{k}}^{(r)}$. The eigenmodes are fundamentally characterized by their wavevector in the Brillouin zone of the magnetic lattice; as well as by their structure within each unit cell (Fig.3.5) which can be parametrized via two bond-dependent coefficients $a_{\mathbf{k}}^{(r)}$ and $b_{\mathbf{k}}^{(r)}$ for the sites 1, 2 ($a_{\mathbf{k}}^{(r)}$) and 3 ($b_{\mathbf{k}}^{(r)}$), according to the numbering convention of Fig. 3.5. The eigenmodes of the two lowest bands exhibits a structure reminiscent of optical and acoustic modes of phonon spectra, with in- and out-of-phase oscillations in the unit cell

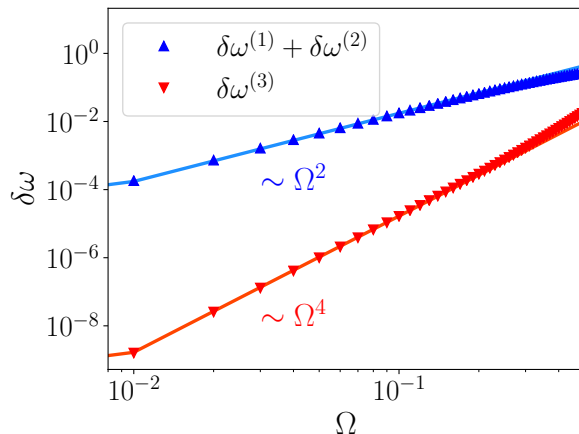


Figure 3.7: Evolution of the band openings with respect to the transverse field Ω , for $J = 1$ and $H = 0.9$. Solid lines represent the polynomial fitting for the bandwidth by Ω .

$$\begin{cases} \mathbf{u}_{\mathbf{k}}^{(1)} = (a_{\mathbf{k}}^{(1)}, -a_{\mathbf{k}}^{(1)}, b_{\mathbf{k}}^{(1)}) \\ \mathbf{u}_{\mathbf{k}}^{(2)} = (a_{\mathbf{k}}^{(2)}, a_{\mathbf{k}}^{(2)}, b_{\mathbf{k}}^{(2)}) \end{cases} \quad (3.2)$$

where $|a_{\mathbf{k}}^{(1,2)}| \gg |b_{\mathbf{k}}^{(1,2)}|$. The excitations of the low-lying bands are then mainly propagating on the up-oriented spins of the unit cell, while the down-oriented one is marginally involved in the wavefunction. The structures of eigenmodes shed light on two properties of the low-lying bands : the presence of Dirac cones in the spectrum and the low energy excitations they describe. Indeed, the excitations of the lowest bands have predominantly support on the honeycomb-shaped lattice formed by the up-oriented sites, leading to a graphene-like spectrum. Moreover, since the up-oriented sites are flippable due to a vanishing local mean-field, the only energetic cost paid to excite the up-oriented sublattice comes from the longitudinal magnetic field H , which fundamentally controls the minimum excitation energy.

On the other hand, the third band has mainly support on the triangular lattice of down-oriented spins,

$$\mathbf{u}_{\mathbf{k}}^{(3)} = (a_{\mathbf{k}}^{(3)}, a_{\mathbf{k}}^{(3)}, b_{\mathbf{k}}^{(3)}) \quad (3.3)$$

with $|b_{\mathbf{k}}^{(3)}| \gg |a_{\mathbf{k}}^{(3)}|$; the energetic cost necessary to create these excitations is much higher due to the strong up-oriented mean-field felt by these sites. This structure of eigenmodes also explains the relative flatness of the high-lying band of the spectrum: as the down-oriented sites are disconnected and they are only weakly coupled to the rest of the lattice, excitations have to propagate according to a two-fold mechanism which involves an intermediate step through the up-oriented lattice. This propagation mechanism is highly non-resonant as can be deduced from a perturbative treatment of the effects of the transverse field. As

we discussed in the previous chapter, the introduction of a transverse field leads to a tilting of the quantization axis z' and therefore to the introduction of Ising couplings along the local x' -axis $S^{x'}S^{x'}$. From the point of view of the bosonic excitations of the spin system, these terms induce tunneling and pair creation and annihilation terms with an effective amplitude $J_{\text{eff}} \sim J \sin^2 \theta$, in the low field limit $\Omega \ll 1$. Given that $\sin \theta = \Omega/\Omega_c$, with $\Omega_c = 1.5J$, the resulting effective coupling for the propagation of excitation on the sublattice A is expected to be of the form $J_{\text{eff}} \sim \Omega^2/J$ and to display a bandwidth of the same form. On the other hand, excitations sitting on the sublattice B propagate by performing a virtual transition through a lower energy state of the sublattice A , so that the two-step propagation mechanism leads to an effective hopping amplitude $J_{\text{eff}} \sim \Omega^4/J^3$ controlling the bandwidth of the upper band. These scaling relations for the bandwidths

$$\begin{cases} \delta\omega^{(1,2)} \propto \Omega^2 \\ \delta\omega^{(3)} \propto \Omega^4, \end{cases} \quad (3.4)$$

compare well with the actual behaviour of the bandwidth for low fields as demonstrated on Fig. 3.7.

3.2.3 Quench dynamics

As discussed in the previous section, the excitations of the antiferromagnetic transverse-field Ising model on a triangular lattice exhibits rich spectral properties. In the following we will investigate several dynamical signatures of their distinctive properties, namely the existence of excitation modes with radically different propagation properties as well as spatial structures. All the results presented hereafter are obtained with the choice of parameters $\Omega = 0.6J$ and $H = 0.3J$, for which the width of the high-energy band is $\delta\omega^{(3)} = 0.04(\delta\omega^{(1)} + \delta\omega^{(2)})$, ensuring the stabilization of a mean-field state and a large separation in width between the bands.

Global quench and correlation functions – The first property we will investigate is the evolution of spin-spin correlation functions in search of evidences of the band flatness. Indeed, the multiband nature of the spectrum is expected to result in a dynamics with several typical timescales defined by band-dependent Lieb-Robinson velocities $v_{\text{LR}}^{(r)} = 2 \max_{\mathbf{k} \in \text{BZ}} |v_g^{(r)}(\mathbf{k})|$.

The dynamics is initialized from the mean-field ground state, which is a fully factorized states displaying no correlations between spins. Correlations are introduced by the ensuing non-equilibrium evolution, and we will focus on the x -spin component as it is the one displaying the strongest build-up of correlations. The corresponding correlation function is:

$$C^{xx}(\mathbf{r}_{lp}, \mathbf{r}_{l'p'}; t) = \langle \delta \hat{S}_{lp}^x \delta \hat{S}_{l'p'}^x \rangle(t), \quad (3.5)$$

where $\delta \hat{S}_{lp}^x = \hat{S}_{lp}^x - \langle \hat{S}_{lp}^x \rangle$, which in terms of linearized bosonic operators reads

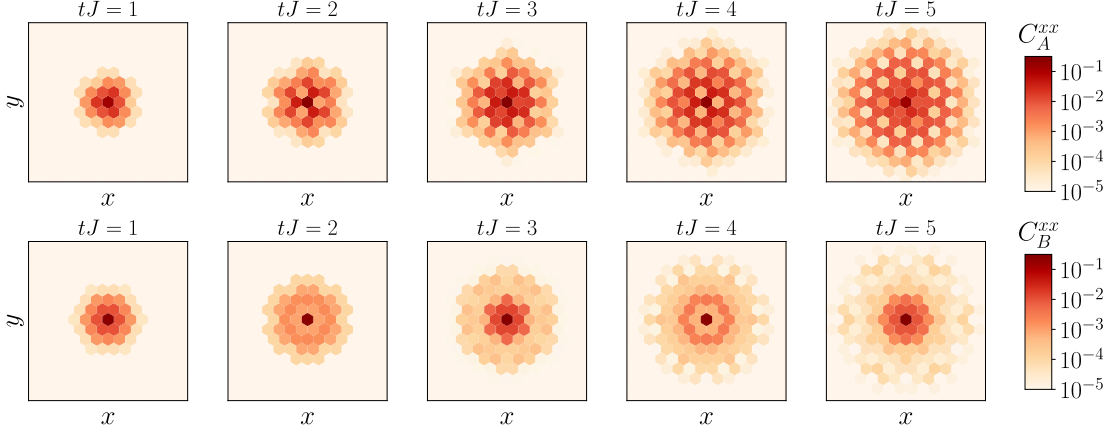


Figure 3.8: Evolution of spin-spin correlation functions on the triangle lattice after a global quench from the mean-field state - The first row shows the build-up of correlations between a site $p = 2$ with the rest of the system, while the second row shows the correlations taken from a site at $p = 3$

$$C^{xx}(\mathbf{r}_{lp}, \mathbf{r}_{l'p'}; t) \simeq \sin \theta_p \sin \theta_{p'} \left(\langle \hat{b}_{lp}^\dagger \hat{b}_{l'p'} \rangle \langle \hat{b}_{lp} \hat{b}_{l'p'}^\dagger \rangle + \langle \hat{b}_{lp}^\dagger \hat{b}_{l'p'}^\dagger \rangle \langle \hat{b}_{lp} \hat{b}_{l'p'} \rangle \right) \quad (3.6)$$

$$+ \frac{S}{2} \cos \theta_p \cos \theta_{p'} \left(\langle \hat{b}_{lp}^\dagger \hat{b}_{l'p'} \rangle + \langle \hat{b}_{lp} \hat{b}_{l'p'}^\dagger \rangle + \langle \hat{b}_{lp}^\dagger \hat{b}_{l'p'}^\dagger \rangle + \langle \hat{b}_{lp} \hat{b}_{l'p'} \rangle \right).$$

Due to translational invariance modulo the magnetic unit cell, the correlation function only depends on the distance $|\mathbf{r}_{lp} - \mathbf{r}_{l'p'}|$ as well as on the reference site p within the unit cell - more specifically, it depends on whether the reference site belongs to the A sublattice ($p = 1, 2$) or to the B sublattice ($p = 3$). Hence we shall focus our attention on two distinct correlation functions, namely $C_A^{xx}(r)$ and $C_B^{xx}(r)$, whose evolution is represented in Fig.3.8. For both correlation functions, one can clearly observe the ballistic spreading of correlations within light cones, whose aperture velocity is consistent with the predictions of LSW theory. Yet their most remarkable feature lies in their internal structures. Indeed, C_A^{xx} , and

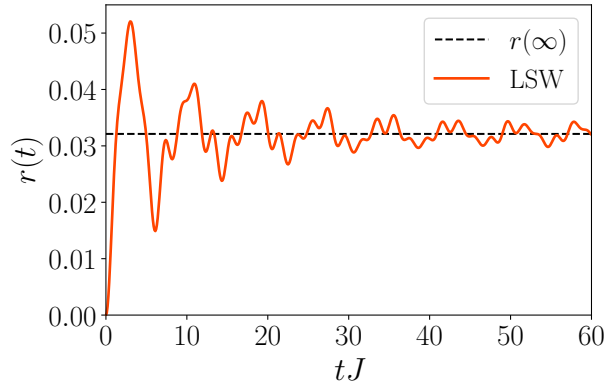


Figure 3.9: Evolution of the density of excitations. The dashed line represents the time-average of r , verifying the condition $r \ll 2S$

C_B^{xx} to a lesser extent, show the establishment of predominant correlations with the sublattice A resulting in honeycomb patterns, corresponding to the support of the low energy eigenmodes. This suggests that the short time dynamics of correlations is dominated by the propagation of modes belonging to the low-lying bands of the spectrum, due to their high group velocity. We shall also note that linear spin-wave theory remains well-controlled over time as shown by Fig. 3.9, where one can see that at all times the dilution condition $r \ll 2S$ remains valid.

The slow dynamics of the high energy band manifests at longer time scales, but an analysis of the density of excitation per band shows that the observation of this phenomenon is actually problematic. Indeed, the density per band $n^{(r)} = (n/N) \sum_{\mathbf{k}} \langle \Psi_0 | \hat{\beta}_{\mathbf{k},r}^\dagger \hat{\beta}_{\mathbf{k},r} | \Psi_0 \rangle$ quantifies the amount of excitations injected in the system by the initial state for each band, and how much they weight in the dynamics of the system. In the cases at hand, the dynamics triggered by the mean-field state results in a low population of the higher energy band ($n^{(3)} = 8.4 \times 10^{-4}$) compared to the low energy ones ($n^{(1)} = 1.0 \times 10^{-2}$ and $n^{(2)} = 2.6 \times 10^{-3}$). Therefore, the dynamics of correlations is dominated by the fast-propagating excitations, preventing an unambiguous observation of the slow dynamics of the high energy band.

Local quench and magnetization – In order to highlight the transport properties of the highest band, we modify the previous quench protocol by initializing the system to the mean-field state plus a single spin-flip on the site (l_0, p_0) belonging to the sublattice B . In other words, the system undergoes a global plus local quench starting from the state $|\Psi'_{\text{MF}}\rangle = \hat{S}_{l_0, p_0}^- |\Psi_{\text{MF}}\rangle$, or in terms of the bosonic operators $|\Psi'_{\text{MF}}\rangle = \hat{b}_{l_0, p_0}^\dagger |0\rangle_b$. Given that the eigenmodes attached to the flat band have support mainly on the B sublattice, exciting a down-oriented spin will result in locally injecting a supplementary amount of β -bosons into the flat band, therefore enhancing the signatures of their slow dynamics.

We monitor the spreading of the wavepacket of extra excitations by means of the local excess of magnetization with respect of the global quench starting from the mean-field state

$$\begin{aligned} \delta m_{lp}(t) &= -\langle \Psi'_{\text{MF}} | \hat{S}_{lp}^{z'}(t) | \Psi'_{\text{MF}} \rangle + \langle \Psi_{\text{MF}} | \hat{S}_{lp}^{z'}(t) | \Psi_{\text{MF}} \rangle \\ &= \langle \Psi'_{\text{MF}} | \hat{n}_{lp}(t) | \Psi'_{\text{MF}} \rangle - \langle \Psi_{\text{MF}} | \hat{n}_{lp}(t) | \Psi_{\text{MF}} \rangle. \end{aligned} \quad (3.7)$$

The above expectation values can be easily computed as they can be seen as expectation values over the vacuum of b -bosons ($|\Psi_{\text{MF}}\rangle$) either of the evolved number operator $\hat{n}_{lp}(t)$ or of its transformed partner $\hat{b}_{l_0 p_0} \hat{n}_{lp}(t) \hat{b}_{l_0 p_0}^\dagger$ (for the expectation value on the $|\Psi'_{\text{MF}}\rangle$ state). In the second case the use of Wick's theorem reduces the expectation value to a time-dependent function of the LSW parameters $u_{\mathbf{k}, p}^{(r)}$, $v_{\mathbf{k}, p}^{(r)}$ and $\omega_{\mathbf{k}}^{(r)}$.

The result of this quench protocol for the local excess of magnetization is shown on Fig. 3.10. Similarly to the spin-spin correlation function, it displays

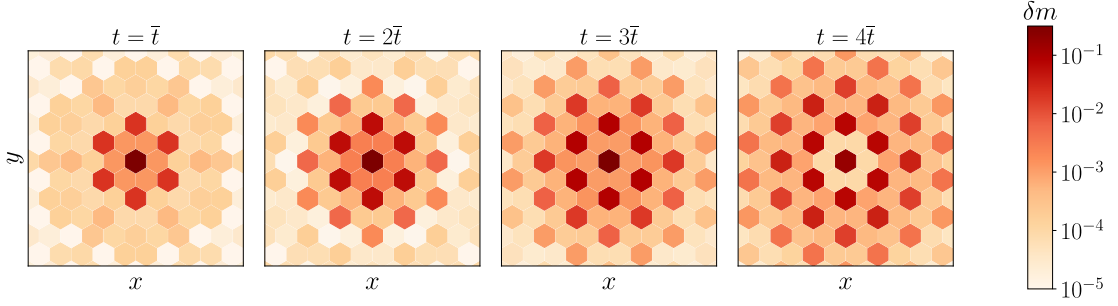


Figure 3.10: Evolution of the local spin excess δm_{lp} following the global/local quench with $p_0 = 3$. The time chosen for the evolution are integer multiples of the characteristic propagation time attached to the flat band $\bar{t} = d/v_{\text{LR}}^{(3)} \simeq 50J^{-1}$.

causal propagation from the injection point ($l_0 p_0$). However, one can notice two main differences from the behaviour observed in correlations: firstly, the spreading wavepacket has essentially support on the sites of the sublattice B ; and secondly, compared to correlations, it exhibits a much larger time scale for propagation, given by $\bar{t} = d/(v_{\text{LR}}^{(3)})$, where d stands for the lattice spacing. Therefore, the local quench protocol successfully highlights two properties of the eigenmodes of the flat band : its spatial structure, mainly involving the sites of the B sublattice on one hand, and the flatness of the band, resulting in the long characteristic timescales for the propagation of these excitations.

3.2.4 Quench spectroscopy

The previous quench protocol highlights the slow dynamics associated with the highest band of the spectrum, and provides an estimate of the bandwidth through the characteristic time scale of propagation $\bar{t} \sim (\delta\omega^{(3)})/Q$, where Q is the norm of a basis vector of the reciprocal space, while $\delta\omega^{(3)}$ is the width of the high energy band. In the following, we will present a diagnostic method to probe the spectral properties of the system in a more quantitative manner.

As we discussed in the first chapter of this thesis, the expectation value of any observable can be expressed in any eigenbasis of the evolution Hamiltonian $\{|\psi_n\rangle\}_{n \in \mathbb{N}}$ as the sum of functions oscillating at frequencies differences between the eigenenergies of the spectrum $\omega_n = E_n/\hbar$,

$$\langle \hat{A} \rangle(t) = \sum_{m,n} \langle \Psi_{\text{MF}} | \psi_m \rangle \langle \psi_m | \hat{A} | \psi_n \rangle \langle \psi_n | \Psi_{\text{MF}} \rangle e^{i(\omega_m - \omega_n)t}. \quad (3.8)$$

As one can see in Eq. (3.6), the eigenfrequencies of the Hamiltonian pilot the evolution of the expectation and their differences can be extracted by a Fourier analysis. Moreover, in order to have a \mathbf{k} -resolved spectrum, the evolved observable should depend on \mathbf{k} itself. A convenient choice for the evolved observable is the spin-spin structure factor defined for the x -component as

$$S_{pp'}^{xx}(\mathbf{k}, t) = \sqrt{\frac{n}{N}} \sum_{l,l'} e^{i\mathbf{k} \cdot (\mathbf{r}_l - \mathbf{r}_{l'})} C^{xx}(\mathbf{r}_{lp}, \mathbf{r}_{l'p'}; t), \quad (3.9)$$

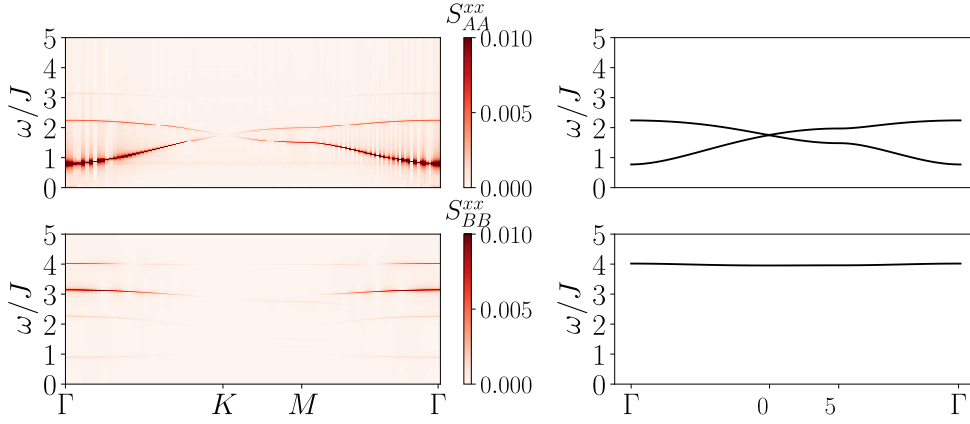


Figure 3.11: Quench spectroscopy of the TFIM on a triangle lattice - The left panels represent the power spectrum $|\text{FT}[S_{pp}^{xx}](\omega, \mathbf{k})|^2$ computed after a postquench evolution of 200 units of J . The right panels represent twice the value of the eigenfrequencies $2\omega_{\mathbf{k}}^{(r)}$, with $r = 1, 2$ for the upper panel and $r = 3$ for the lower one.

where \mathbf{r}_l is the position of the l -th unit cell defined as $\mathbf{r}_l = \mathbf{r}_{l,p=1}$. The choice of the considered correlations, AA , BB or AB , selects the type of excitations involved in the dynamics and consequently the frequencies appearing in the dynamics.

The quadratic approximation underlying the linear spin-wave theory enables to express the spin-spin structure factor at vector \mathbf{k} as

$$\begin{aligned}
 S_{pp'}^{xx}(\mathbf{k}, t) &\simeq f_{pp'}(\mathbf{k}) \\
 &+ \sum_{r \leq r'} g_{pp'}^{rr'}(\mathbf{k}) \cos[(\omega_{\mathbf{k}}^{(r)} + \omega_{\mathbf{k}}^{(r')})t] + i \bar{g}_{pp'}^{rr'}(\mathbf{k}) \sin[(\omega_{\mathbf{k}}^{(r)} + \omega_{\mathbf{k}}^{(r')})t] \quad (3.10) \\
 &+ \sum_{r > r'} h_{pp'}^{rr'}(\mathbf{k}) \cos[(\omega_{\mathbf{k}}^{(r)} - \omega_{\mathbf{k}}^{(r')})t] + i \bar{h}_{pp'}^{rr'}(\mathbf{k}) \sin[(\omega_{\mathbf{k}}^{(r)} - \omega_{\mathbf{k}}^{(r')})t].
 \end{aligned}$$

This shows that the Fourier spectrum of the structure factor is composed of sum and differences of the eigenfrequencies $\omega_{\mathbf{k}}^{(r)}$, respectively weighted by $g_{pp'}^{rr'}$ and $\bar{g}_{pp'}^{rr'}$ for sums and $h_{pp'}^{rr'}$ and $\bar{h}_{pp'}^{rr'}$ for differences, whose explicit expression is provided in Appendix C. As a result, a Fourier transform discloses the band structure of the excitation via the frequency sums; while the Fourier amplitudes g and h inform us of the overlap of the modes at hand with the sites p and p' of the unit cell. Such an analysis provides a complete description of both the spectral properties of excitations and the spatial structure of the corresponding eigenstates over the unit cell. This spectroscopic analysis based on the postquench evolution of observables, which we call *quench spectroscopy*, offers an alternative to scattering-based spectroscopic techniques (such as neutron or light diffraction) in the analysis of synthetic condensed matter systems, as shown by some successful implementation in cold-atom experiments [51, 81]. This idea has been recently generalized beyond the realm of LSW theory by Villa & al. [95].

We applied the quench spectroscopy protocol to the dynamics of the antiferromagnetic TFIM on the triangular lattice evolved from the mean-field state, for the same set of parameters as for the correlation functions shown on Fig.3.8, namely $(\Omega/J = 0.6, H/J = 0.3)$. The result of the Fourier analysis performed on a system of size 120×120 at times up to $tJ = 200$ are displayed on Fig.3.11. The structure factors S_{AA}^{xx} (upper left panel) and S_{BB}^{xx} (lower left panel) both reveal complementary aspects of the band structure : due to their support on the A sublattice, the former discloses the two lower bands of the spectrum with the frequency combinations $2\omega_{\mathbf{k}}^{(1)}$ and $2\omega_{\mathbf{k}}^{(2)}$ (represented for comparison next to the AA structure factor). On the other hand, the latter clearly reveals the flat band as it displays a line of peaks at $2\omega^{(3)}$. One can also notice that secondary peaks can be seen on the BB structure factor, corresponding to other band combinations such as $\omega_{\mathbf{k}}^{(2)} + \omega_{\mathbf{k}}^{(3)}$, due to the non-vanishing overlap between their respective eigenmodes.

3.3 Aharonov-Bohm caging : Lieb and Kagome lattices

3.3.1 High-energy quench protocols

In the following, we will explore the dynamics resulting from the second mechanism responsible for the emergence of flat bands, namely Aharonov-Bohm caging. Among the large family of lattice geometries supporting such behaviour, we chose to focus our investigation on two of them : the Lieb lattice and the kagome lattice, with the purpose of directly evidencing the emergence of localized states. In the case of the kagome lattice, the study of the antiferromagnetic Ising model with LSW theory is faced with much more difficulties than in the case of the triangular lattice, as the infinite degeneracy of the ground state without transverse field is not lifted in favor of a ground state with long-range order when a field is applied [66]. This state of affairs is not substantially altered by the application of a longitudinal field, making the application of LSW theory very problematic as it systematically results in the emergence of imaginary frequencies. Nonetheless, when focusing on quench dynamics from a uniform state with all spins aligned with a given direction, one can change perspective, thanks to the following theorem proved in Refs. [38, 78].

Theorem 2. *Consider a Hamiltonian $\hat{\mathcal{H}}$ admitting a real-valued representation over a basis of vector $\{|\phi_n\rangle\}$, if the unitary dynamics piloted by $\hat{\mathcal{H}}$ is initialized from a state $|\Psi_0\rangle$ written on the same basis as a linear combination with only real coefficients. Then the evolution of any observable \hat{A} admitting a real-valued representation is invariant under time-reversal symmetry, namely at all times*

$$\langle \hat{A} \rangle(t) = \langle \Psi(t) | \hat{A} | \Psi(t) \rangle = \langle \hat{A} \rangle(-t). \quad (3.11)$$

As a corollary of this theorem, the unitary evolution starting from $|\Psi_0\rangle$ and governed by $\hat{\mathcal{H}}$ is equivalent to the evolution governed by $-\hat{\mathcal{H}}$. In the case at hand,

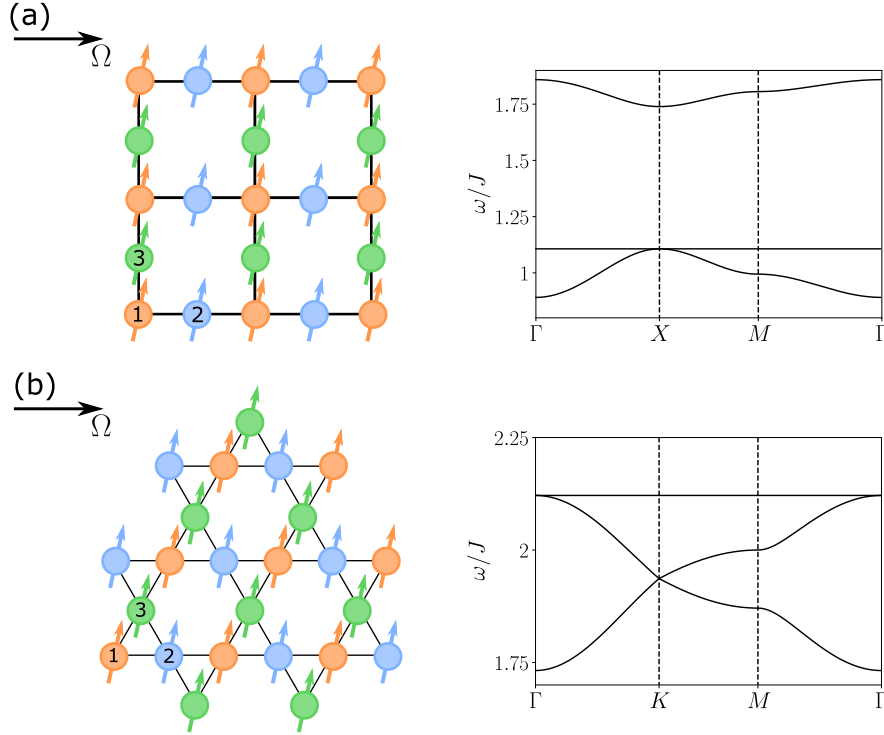


Figure 3.12: Lattice and band structures of flat-band systems - (a) shows the unit cell and the excitation spectrum of the Lieb lattice computed for $\Omega/J = 1$, while (b) displays the unit cell and band structure of the kagome lattice also for $\Omega/J = 1$.

one can consider a quench starting from the mean-field ground state of the ferromagnetic Ising model, $|\Psi_0\rangle = \otimes_i |\uparrow\rangle_i$, where $|\uparrow\rangle_i$ is the spin configuration at site i aligned with the z' -axis, tilted with respect to the z -axis by the application of the field. As both the initial state as well as the Hamiltonian obey the hypothesis of the above theorem, then evolving this state with the ferromagnetic Hamiltonian gives the same results as evolving it with the antiferromagnetic Hamiltonian, appropriate for the physics of Rydberg atoms. In other words, instead of exploring the low-energy excitations spectrum, this type of quench prepares the antiferromagnetic system in its highest energy states, which is equivalent to exploring the low-energy dynamics of the ferromagnetic Hamiltonian.

The linear spin-wave theory is well-defined for the ferromagnetic model, and no imaginary frequencies appear in the spectrum. In the spirit of the above discussion we shall adapt the same strategy for the Lieb and kagome lattices. The resulting spectra and unit cells for the two lattice structures are represented in Fig. 3.12. The spectrum computed for the kagome lattice exhibits Dirac cones and a flat band in a manner that is identical to what can be observed for its tight-binding counterpart modulo a global energy shift. On the contrary, the excitation spectrum of the Lieb lattice differs from that of the tight-binding model. Indeed, it displays two low-lying bands, one of which being the flat band, and a single high energy band, while the tight-binding model predicts also the existence of a Dirac cone on the spectrum. This discrepancy between the LSW spectrum

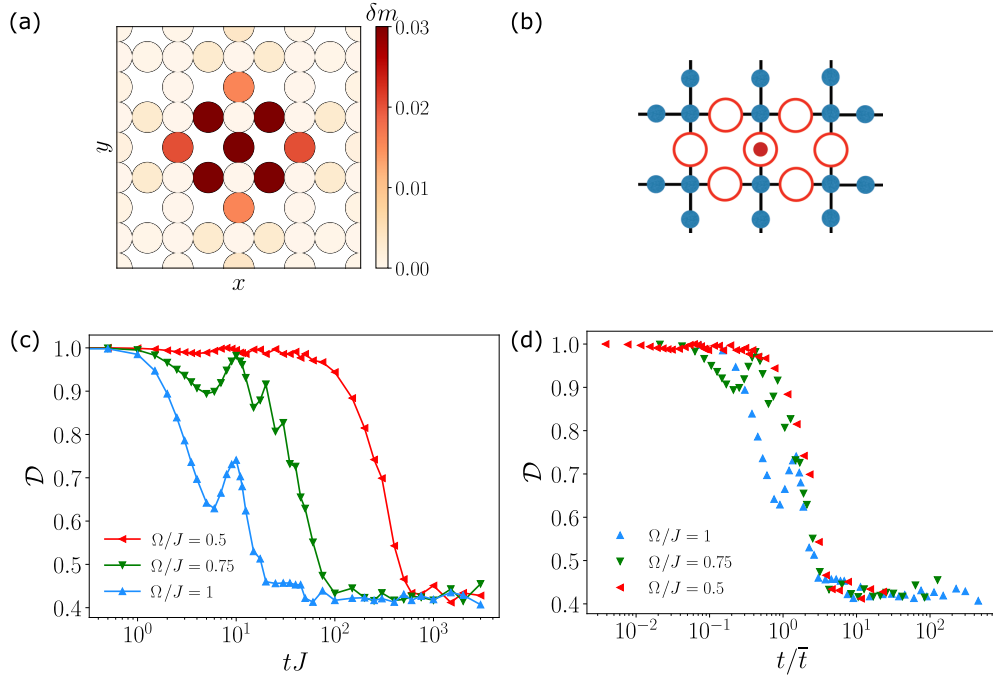


Figure 3.13: Caged state in the Lieb lattice - (a) Asymptotic spin deviation δm_{l_p} following a local/global quench. (b) Representation of the localized states overlapping with the injection site (l_{0p_0}). (c) Evolution of the localized fraction computed for a 30×30 lattice for several transverse magnetic fields. (d) Rescaled evolution of the localized fraction by the typical propagation timescale.

and the tight-binding model is actually explained by the site-dependent chemical potential appearing in the LSW Hamiltonian described in Appendix. A. Indeed, this local chemical potential depends on the coordination of the sites, and since sites 2 and 3 of the unit cell have two nearest neighbours (contrarily to site 1 which has four of them), the chemical potential is inhomogeneous ($\mu_1 \neq \mu_{2,3}$) on the unit cell, hence the opening of a gap between the low- and high-energy parts of the spectrum. On the other hand, given that every site of the kagome lattice has the same number of nearest neighbours, the chemical potential is homogeneous over the unit cell and the energy spectrum expected from a tight-binding model is preserved.

3.3.2 Emergence of caged states

As we did for the triangular lattice, we can analyse the structure of eigenmodes and how they are supported on the unit cell. The translational invariance of the Hamiltonian leads to a description of the flat-band modes in terms of extended Bloch functions $\psi_{\mathbf{k}}(\mathbf{r}) = \exp(i\mathbf{k} \cdot \mathbf{r})u_{\mathbf{k}}(\mathbf{r})$, where

$$u_{\mathbf{k}} = (0, a_{\mathbf{k}}, -b_{\mathbf{k}}) \quad (3.12)$$

is defined over the unit cell; yet given that all Bloch waves of the flat band are at the same energy, they can be superposed to form localized eigenmodes at

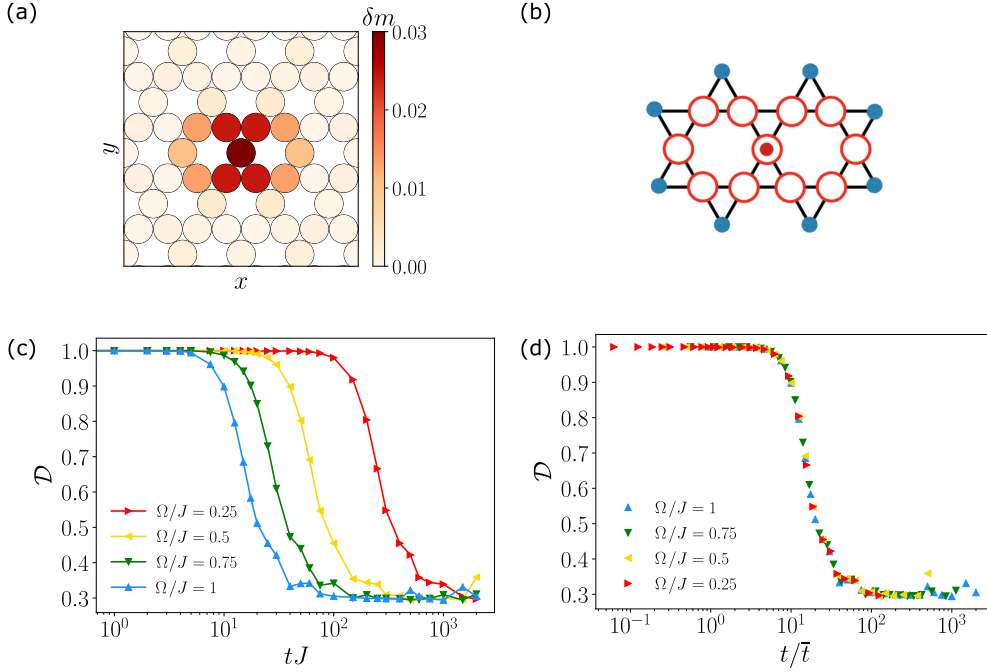


Figure 3.14: Caged state in the kagome lattice - (a) Asymptotic spin deviation δm_{l_p} following a local/global quench. (b) Representation of the localized states overlapping with the injection site ($l_0 p_0$). (c) Evolution of the localized fraction computed for a 30×30 lattice for several transverse magnetic fields. (d) Rescaled evolution of the localized fraction by the typical propagation timescale.

the same energy, with the same geometry as in Fig. 3.1. A local/global quench provides a way to populate the flat band by injecting a magnetic excitation on one site and then let the wavepacket of the excitation spread so as to reveal the localized modes. This strategy is particularly important in the case of the Lieb lattice, as one find that a global quench from the mean-field ground state leaves the flat band completely empty of excitations, so that its presence completely disappears from the ensuing dynamics.

Lieb lattice – The dynamics is initialized from the ferromagnetic mean-field state with one flipped spin: $|\Psi_0\rangle = \hat{b}_{l_0, p_0}^\dagger |\Psi_{\text{MF}}\rangle$, with the injection site chosen such that $p_0 = 2, 3$ (following the convention established in Fig. 3.12), as suggested by Eq. (3.12), in order to populate a localized mode. As shown on Fig. 3.13, once part of the injected wavepacket escaped due the dispersive modes overlapping with the flipped site, one can observe the emergence of the pattern expected from the localized state in the excess magnetization at long times δm . Moreover, since we set $H = 0$, the only remaining parameter left to control the bandwidth and the characteristic time of the propagation of excitation is the transverse field Ω . Therefore, by tuning the transverse field, one can control the time at which the localized mode emerges, and possibly the population of excitations remaining trapped in it. Hereafter, we introduce the localized fraction, namely the excess magnetization that remains trapped in the localized modes (\mathcal{LM}) overlapping with site (l_0, p_0)

$$\mathcal{D}(t) = \sum_{(l,p) \in \mathcal{LM}(l_0 p_0)} \delta m_{lp}. \quad (3.13)$$

As seen on Fig. 3.13, the localized fraction decreases with time as the wavepacket spreads and partially escapes the Aharonov-Bohm cage before reaching an Ω -independent asymptotic value. Though the asymptotic value of the localized fraction is independent of the transverse field, the saturation time actually does and therefore controls the emergence of the caged state.

Kagome lattice – The same kind of study can be performed for the kagome lattice with similar effects, as shown on Fig. 3.14. As for the Lieb lattice, the dynamics exhibits the emergence of a caged state which is the superposition of the two hexagone-shaped localized modes overlapping with the injection site. Similarly to the Lieb lattice, one can investigate the evolution of the localized fraction of the magnetization deviation for different values of the magnetic field and study the localization dynamics. It turns out that \mathcal{D} displays similarities with what we witnessed for the Lieb lattice: for every value of the magnetic field the localized fraction relaxes towards the same asymptotic value, and field dependence is only shown by the time necessary to observe the stabilization of the caged state. However, contrarily to the Lieb lattice, the dynamics of the localized fraction exhibits more pronounced universal features, for if time is rescaled by the characteristic time $\bar{t} = d/(2v_{\text{LR}}) \propto \Omega^2$, all points collapse on the same universal curve, whose origin is still to be fully understood.

3.3.3 Effects of van der Waals interactions

The results and phenomena we observed in the flat band systems rely on the existence of nearest neighbours couplings only, neglecting the long-range nature of van der Waals coupling, which are naturally present in the models realized by Rydberg-atom quantum simulators. In particular, the Aharonov-Bohm caging effect at the heart of the flatness of bands for the Lieb and kagome lattices is a fine tuned effect that specifically relies on nearest-neighbour interactions. These observations question the relevance of the study of flat-band systems with for Rydberg-atom simulators. In the following, we will investigate the robustness of flat bands of excitations when the algebraic tail of the van der Waals couplings is taken into account into the linear spin-wave calculations.

The additional intersite couplings introduced by the long-range nature of van der Waals interactions result in a finite width of the flat band as one can see on the left panels of Fig. 3.15 which compare the nearest-neighbour spectra (blue) with the one obtained with van der Waals interactions (orange). One can clearly see that the flat band of the Lieb lattice acquires a sizeable width, while the width of the flat band is nearly invisible for the kagome lattice. This discrepancy is explained by the geometries of these two lattices and the resulting distance between the next-nearest neighbours. Indeed the next-nearest neighbours are at a distance of $\sqrt{3}a$ (where a is the lattice spacing) for the kagome lattice, leading

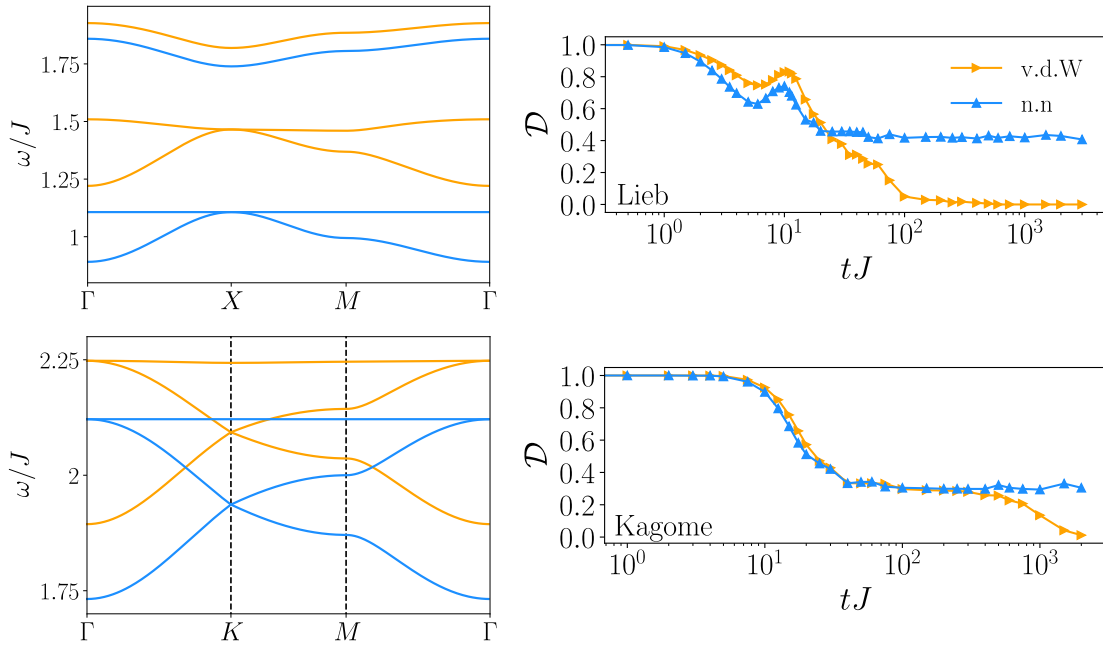


Figure 3.15: Influence of the long-range nature of van der Waals interactions - Left panels show the time-evolution of the localized fraction for both van der Waals and nearest-neighbours interactions, for Lieb and kagome geometries. The right panels show the influence of van der Waals interactions on the band structure, particularly on the width of the flat bands.

to ratio between nearest and next nearest neighbours of $J_{nnn}/J_{nn} = 1/27$, while for the Lieb lattice this distance is $\sqrt{2}a$ with a coupling ratio of $J_{nnn}/J_{nn} = 1/8$. Therefore the effects of the tail in the van der Waals couplings are more sizeable in the Lieb lattice and give rise to a wider bandwidth. The direct consequence of a finite band width $\delta\omega$ is that the previously localized modes now acquire a finite life-time $\tau \sim 1/\delta\omega$ that limits their observation at long times.

The evolution of the localized fraction is also compared on the right panels of Fig. 3.15 for nearest-neighbour and van der Waals couplings. While the dynamics of \mathcal{D} matches the one predicted for nearest neighbours at short time scales, the localized fraction is eventually found to go to zero at long times given by the inverse of the bandwidth. The kagome lattice however exhibits a plateau in the evolution of the localized fraction over a much longer time scale, enabling in practice the observation of Aharonov-Bohm caging via Rydberg-atom simulators.

3.4 Conclusions

In this chapter, we discussed the quench dynamics of several two-dimensional antiferromagnetic Ising models featuring flat bands of excitations. We observed how the flatness of excitations affects the dynamics of spin systems following global or global/local quenches and how we could use this dynamics in order to design spectroscopic strategies to unveil the spectral properties of experimentally relevant models in the context of Rydberg atoms simulators.

However, during this study we also restricted ourselves to cases where the density of quasiparticles was weak enough to allow us to neglect the effects of interactions, and especially the non-linearities that mimic the hardcore constraint set on bosonic excitations. In the case of quenches inducing higher densities of quasiparticles than those that we presently considered, such effects cannot be neglected any more, thus putting into question several aspects of the physics of flat-band systems. Indeed, we expect the repulsive hardcore interaction to induce scattering among the quasiparticles and consequently rearrange the populations of each band. As we will further elaborate in the concluding chapter of this thesis, the robustness to non-linearities of the localization effects reported above is an intriguing question that we postpone to further works.

Anomalous diffusion in positionally disordered quantum spin systems

*"Souvent dans l'être obscur habite un Dieu caché ;
Et comme un œil naissant couvert par ses paupières,
Un pur esprit s'accroît sous l'écorce des pierres !"*

Gérard de Nerval, "Vers dorés", *Les Chimères*

4.1 Disordered spin systems

4.1.1 Ground-state localization and localization of the excitations

Coherent waves in a disordered medium are subject to multiple reflections and interference effects that may lead eventually to a drastic suppression of their propagation - a phenomenon known as Anderson localization [6]. In the context of quantum mechanical systems such a phenomenon alters substantially the eigenstates of single particles in a disordered potential, which acquire an exponentially localized nature. On the other hand, disorder also impacts the low-energy behaviour of quantum many-body systems by disrupting the long-range correlations that one may observe in the ground state of a clean system, thus driving the system toward a quantum phase transition. Several examples of such disorder-induced phase transitions are offered by solid-state physics models such as the Bose-glass transition [37], superconductor-insulator transition [29] or the Mott-glass transition [98]. These transitions are also characterized by the localization of the elementary excitations above the new disordered ground state, as stressed by a representation of the elementary excitations of disordered quantum spin in terms of bosonic spin-waves [4] and slave bosons [97].

In particular, for systems whose ground state spontaneously breaks a contin-

uous symmetry -such as bosonic or fermionic superfluids with $U(1)$ symmetry, or spin systems with $SU(2)$ symmetry- elementary excitations are expected to remain extended as long as the continuous symmetry broken by the ground state is not restored. The robustness of the properties of elementary excitations against disorder stems from the Goldstone theorem [68] and the low-energy excitations (Goldstone bosons) that it predicts in systems spontaneously breaking a continuous symmetry. Indeed, a Goldstone boson is a gapless, long-wavelength excitation which connects the symmetry breaking ground state with other ground states having a "rotated" order parameter - hence its gapless nature. The fact that it has the tendency to rearrange the order parameter of the system globally requires that it has an extended nature, and therefore it prevents localization even in the presence of disorder. On the other hand, if disorder restores the broken symmetry in the ground state, it also exposes the low-energy excitation spectrum to localization. Therefore, if a ground-state transition toward localization occurs, its effects should be observable in both the low-temperature thermodynamic properties of the system (governed by the ground state) and the low-energy dynamics, which reflects the nature (extended or localized) of the excitations.

For system breaking a discrete symmetry, however, Goldstone theorem does not apply and the excitation spectrum is expected to be gapped. In this case, spontaneous symmetry breaking in the ground state cannot prevent the localization of low-energy excitations. The paradigm that we have just outlined above breaks down, and the properties of the low-energy excitation are generically decoupled from the presence or absence of long-range order in the ground state. The excitations atop a discrete symmetry breaking ground state may then be localized. Though rarely highlighted, this dichotomy between the ground-state properties and those of excitations has been nonetheless reported in quasi-periodic Ising chains with a transverse magnetic field [23, 26]. In this chapter, we will discuss a similar illustration of the separation between ground-state and excitation properties in a two-dimensional disordered Ising model inspired by the possibilities offered by Rydberg atoms simulators.

4.1.2 Positionally disordered atoms arrays

Let us consider a square array of $L \times L$ atoms whose internal states are mapped onto $S = 1/2$ spins according to the transverse-field Ising model that we previously described (Eq. (2.1)). We will take advantage of the flexibility offered by the individual trapping of single atoms via optical tweezers to introduce geometrical disorder in the atom array in a controlled manner. Positional disorder can be implemented by means of a tunable displacement of the atoms with respect to their ordered position $\mathbf{r}_i = (n_1 + d_1)\mathbf{e}_1 + (n_2 + d_2)\mathbf{e}_2$, where $\mathbf{e}_{1,2}$ are the basis vectors of the square lattice, while $n_{1,2}$ are integer numbers standing for the localization of site i in the clean case. The displacements $d_{1,2}$, on the other hand, are uniformly distributed random variables with value in the interval $[-\Delta, \Delta]$, where the disorder parameter Δ is the knob that tunes the system from perfectly ordered ($\Delta = 0$) to completely disordered $\Delta \lesssim 1/2$, the upper-bound being half the lattice spacing. As a consequence of the position dependence of the van der

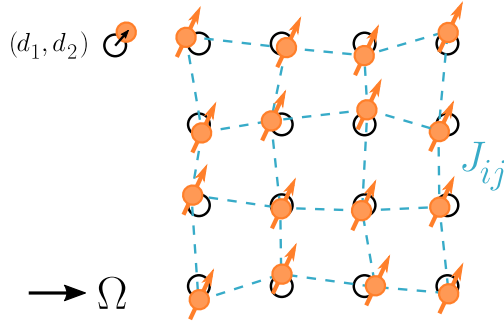


Figure 4.1: Disordered square lattice - The Rydberg atoms represented by the orange spheres are displaced away from the position on the ordered square lattice shown as an array of black circles. The dashed blue lines shows the randomized nearest-neighbours Ising couplings, representing the strongest source of randomness in the Hamiltonian.

Waals couplings, positional disorder translates into the model as a randomization of the spin-spin couplings $J_{ij} = J_0/|\mathbf{r}_i - \mathbf{r}_j|^6$, with a high sensitivity to positional variations due to the fast decay of the van der Waals interactions.

In the following study, we shall focus our attention on the quench dynamics starting from a (nearly) homogeneous spin configuration. This choice, rather natural for experiments, amounts to preparing the spins in a high-energy state for the antiferromagnetic van der Waals interactions. Yet, as we have seen in Sec. 3.3.1, when starting from a time-reversal invariant state, the quantum dynamics generated by \mathcal{H} and $-\mathcal{H}$ have the same physical properties (in terms of average values of observables as well as of entanglement entropies), so that we can more conveniently view the quench dynamics that starts from a (nearly) homogeneous spin state as a low-energy quench for the ferromagnetic Hamiltonian $-\mathcal{H}$. We shall adjust this point of view in the following and analyze the properties of the quantum Ising model on the positionally disordered square lattice with ferromagnetic van der Waals interactions. Moreover, we will also make the simplifying assumption that the detuning perfectly compensates the term $\kappa_i = \sum_j J_{ij}$, so that the longitudinal field H vanishes. This is strictly impossible as κ_i is a site-dependent term due to the randomization of the spin positions. Taking it into account would introduce a further source of randomness in the Hamiltonian, with the effect of strengthening the disordered nature of the Hamiltonian, but not altering substantially the phenomenology of the system at hand. Under these assumptions, the Hamiltonian of interest reads

$$\hat{\mathcal{H}} = -\frac{1}{2} \sum_{i,j} J_{ij} \hat{S}_i^z \hat{S}_j^z - \Omega \sum_i \hat{S}_i^x, \quad (4.1)$$

describing a Rydberg-atom simulator that mimics the physics of a random-bond transverse field ferromagnetic Ising model with van der Waals couplings and correlated bond randomness, as represented on Fig. 4.1. In the following we shall consider only the case where $\Omega = |J_0|$.

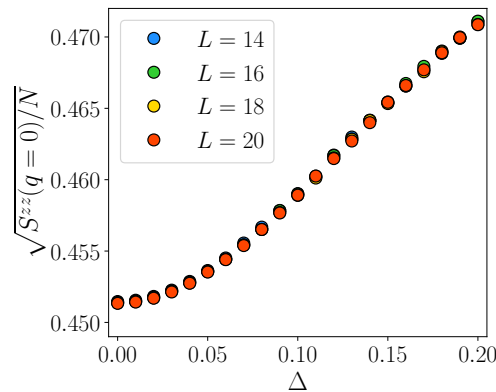


Figure 4.2: Ground-state Ising order parameter in the linear spin-wave theory as a function of the disorder parameter Δ , computed for several linear sizes L

As the introduction of disorder disturbs the translational invariance of the system, the linear spin-wave formalism that we introduced in Chapter 2 should be amended. Similarly to the clean case, we start the spin-wave construction by aligning the local quantization axes with the ones defined by the mean-field state $|\Psi_{\text{MF}}\rangle = \otimes_i [\cos(\theta_i/2)|\uparrow\rangle_i + \sin(\theta_i/2)|\downarrow\rangle_i]$, where θ_i is the local angle imposed by the transverse field. The mean-field state consequently defines a set of local rotations around the y -axis $\mathcal{R} = \otimes_i \mathcal{R}_y^{(i)}(\theta_i)$ leading to a transformed spin Hamiltonian $\mathcal{R}^\dagger \hat{\mathcal{H}} \mathcal{R}$ that can be mapped onto a bosonic Hamiltonian according to the Holstein-Primakoff transformation. Under the assumption that the described Bose gas is sufficiently dilute ($\hat{n}_i \ll 2S$), the bosonic Hamiltonian can be expanded up to quadratic order and then takes the form $\hat{\mathcal{H}} = E_{\text{MF}} + (1/2) \sum_{i,j} (\hat{b}_i^\dagger, \hat{b}_i) \mathcal{A}_{ij} (\hat{b}_j, \hat{b}_j^\dagger)^T$, that can be diagonalized in a straightforward manner by the means of a Bogoliubov transformation. However, due to the lack of translational invariance, the Bogoliubov modes are not labeled by the momentum \mathbf{k} , but by a generic index α for the new bosonic operators $\hat{\beta}_\alpha^{(\dagger)}$ expressing the Holstein-Primakoff bosonic operators through the linear transformation $\hat{b}_i = \sum_\alpha u_i^{(\alpha)} \hat{\beta}_\alpha + v_i^{(\alpha)} \hat{\beta}_\alpha^\dagger$. The condition $\sum_i [|u_i^{(\alpha)}|^2 - |v_i^{(\alpha)}|^2] = 1$ guarantees that the β operators are bosonic ones. The Bogoliubov transformation leads to the diagonalized Hamiltonian $\hat{\mathcal{H}} = E_{\text{MF}} + \sum_\alpha \epsilon_\alpha \hat{\beta}_\alpha^\dagger \hat{\beta}_\alpha$, where ϵ_α stands for the α -th eigenenergy of the spectrum.

4.1.3 Ground-state properties : dirty ferromagnetism

In the following, we will discuss the ground-state behaviour of the positionally disordered transverse-field Ising model and how the randomization process that we implemented preserves and even enhances long-range order, through an average strengthening of the nearest-neighbours couplings, thereby fully justifying a spin-wave treatment.

Ising order is described by the magnetization m^z of spins along the z -axis, namely $m^z = (1/N) \sum_i \langle S_i^z \rangle$. Alternatively, the longitudinal magnetization can also be obtained via the spin-spin structure factor at momentum $\mathbf{k} = 0$ defined as

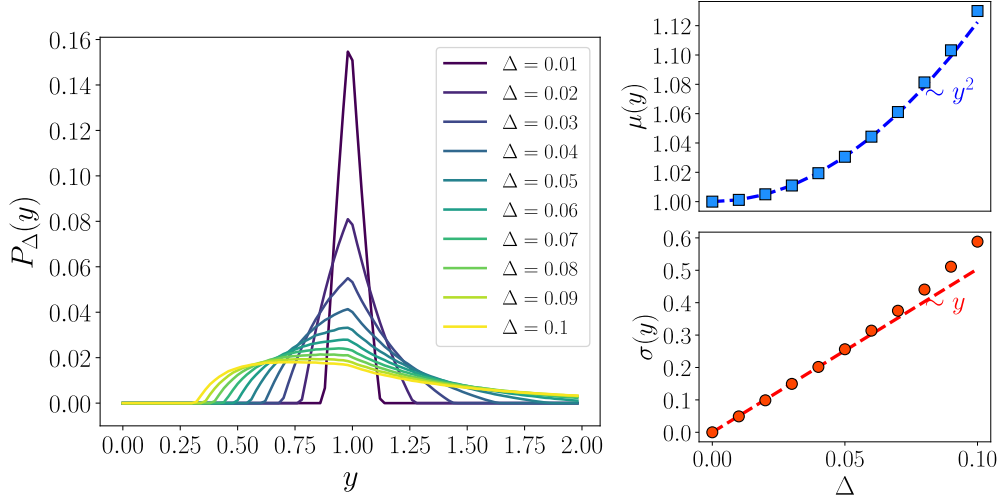


Figure 4.3: Nearest-neighbours coupling distribution

$S_{\mathbf{k}=0}^{zz} = (1/N) \sum_{i,j} \langle S_i^z S_j^z \rangle_\beta$ computed over the ground state (namely the vacuum of the β -bosons). The order parameter can then be estimated as

$$m^z = \sqrt{\frac{1}{N} S_{\mathbf{k}=0}^{zz}}. \quad (4.2)$$

The structure factor can be explicitly computed in terms of the Bogoliubov vectors $\mathbf{u}^{(\alpha)}$ and $\mathbf{v}^{(\alpha)}$ with entries given by the coefficients $u_i^{(\alpha)}$ and $v_i^{(\alpha)}$. In terms of such coefficients, the spin-spin structure factor takes the form

$$S_{\mathbf{k}=0}^{zz} = \frac{1}{N} \left(S^2 N^2 - 2S \sum_{\alpha} |\mathbf{v}^{(\alpha)}|^2 + \sum_{\alpha,\gamma} |\mathbf{v}^{(\alpha)}|^2 |\mathbf{v}^{(\gamma)}|^2 + \sum_{\alpha,\gamma} (\mathbf{v}^{(\alpha)} \cdot \mathbf{u}^{(\gamma)}) (\mathbf{u}^{(\alpha)} \cdot \mathbf{v}^{(\gamma)} + \mathbf{v}^{(\alpha)} \cdot \mathbf{u}^{(\gamma)}) \right). \quad (4.3)$$

Fig. 4.2 shows the ground-state order parameter as a function of disorder strength for different lattice sizes. The results have been averaged over a hundred realizations of disorder. It can be observed that instead of weakening the ferromagnetic order, the introduction of positional disorder leads to its strengthening. Such a seemingly paradoxical affect can be understood as a result of a disorder-induced increase in the average nearest-neighbour coupling. Indeed, the convex property of the coupling function ($J \sim r^{-6}$) ensures the inequality $\mathbb{E}[r^{-6}] > \mathbb{E}[r]^{-6}$, where $\mathbb{E}[\cdot]$ accounts for the statistical average over disorder.

4.1.4 Probability distribution of the disordered couplings

We shall further discuss the properties of the coupling distribution and quantify the behaviour and sensitivity of the system with respect to disorder. In order to gain insight through analytical calculations, we will consider in the following a slightly simplified case where two atoms are displaced in one spatial dimension

with respect to a reference distance (set to 1), with respective displacements d_1 and d_2 uniformly distributed over the interval $[-\Delta, \Delta]$. We will thereafter consider the general case where couplings decay as a power-law of the distance with the exponent α , but we will later specialize the discussion to the case of van der Waals interactions ($\alpha = 6$). The dimensionless coupling y then takes the form

$$y = \frac{J}{J_0} = \frac{1}{|1 - d_1 + d_2|^\alpha}, \quad (4.4)$$

where the total displacement of the two atoms $z = d_1 - d_2$ is also a random variable following a triangle distribution p_Δ with support on the interval $[-2\Delta, 2\Delta]$

$$p_\Delta(z) = \theta(-z)(z + 2\Delta) + \theta(z)(2\Delta - z), \quad (4.5)$$

where θ stands for the Heaviside distribution. As a result, the distribution of normalized couplings with support on the interval $[y_-, y_+]$, where $y_+ = |1 + 2\Delta|^{-\alpha}$ and $y_- = |1 - 2\Delta|^{-\alpha}$, is described by the function

$$P_\Delta(y) = \frac{1}{4\Delta\alpha^2 y^{1+1/\alpha}} [\theta(y - 1)(y^{-1/\alpha} + 2\Delta - 1) + \theta(1 - y)(2\Delta + 1 - y^{-1/\alpha})]. \quad (4.6)$$

From this expression of the distribution of normalized couplings, one can deduce its n -th moment

$$\mathbb{E}[y^n] = \frac{(1 - 2\Delta)^{2-\alpha n} + (1 + 2\Delta)^{2-\alpha n} - 2}{4\alpha^2 \Delta^2 (n - 2/\alpha)(n - 1/\alpha)}, \quad (4.7)$$

which in the limit of weak disorders ($\Delta \rightarrow 0$) can be Taylor expanded to obtain the approximated expression

$$\mathbb{E}[y^n] = 1 + \frac{\alpha^2}{6} n \left(n + \frac{1}{\alpha} \right) \Delta^2 + O(\Delta^4). \quad (4.8)$$

In particular, one can deduce that the variance of the couplings behaves at small disorder as

$$\text{Var}(y) = \frac{\alpha^2}{3} \Delta^2 + O(\Delta^4). \quad (4.9)$$

One can then observe that the variance displays a higher sensitivity of the couplings to disorder the higher the α exponent is. Indeed, the greater α is, the stronger variations are induced by positional disorder in the couplings.

The actual form of the distribution P_Δ of the nearest-neighbour couplings, as computed for atoms displaced on a square window in two dimensions and for $\alpha = 6$, is shown on Fig. 4.3, along with the average value of the coupling μ and the standard deviation σ . One shall notice that the distribution displays an asymmetric form with an increasing skewness as the displacement parameter Δ grows. Similarly to the one-dimensional case, the support of the distribution is bounded by y_- and y_+ , which admit different behaviours in the limit case

$\Delta \rightarrow 0.5$, as $y_- \rightarrow 1/125$, while for the same limit the upper bound y_+ diverges. As predicted in the one-dimensional case, the average value μ grows quadratically with respect to small values of the disorder parameter Δ , which is consistent with the strengthening of ferromagnetism we observed in the order parameter. Moreover, the standard deviation $\sigma = \sqrt{\text{Var}(y)}$ grows linearly with Δ but with a larger proportionality factor than the one predicted by the one-dimensional calculation, since here $\sigma \simeq 5\Delta$ instead of $\sqrt{12}\Delta$. As a result for a relative displacement of a few percent, namely $\Delta = 0.04$, one observes significant coupling fluctuations with $\sigma = 0.2$. As we shall see this small amount of positional disorder will have a drastic impact on the low-energy excitations of the model.

4.2 Spectral properties and localization

4.2.1 Inverse participation ratio

In the case of disorder-induced quantum phase transition involving a continuous symmetry of the ground-state, long-range order is preserved -and even strengthened- by the introduction of disorder, one should not observe localization of the low-energy elementary excitations. However, since the symmetry broken by the Ising order is discrete, the spectrum exhibit an energy gap which decouples the spectrum from the ground-state order. In the following, we will explore the spectrum properties, in particular the form taken by the eigenmodes in search for traces of localization.

The localized nature of a Bogoliubov eigenmode can be captured and studied via the generalized *inverse participation ratio* (IPR_q) [33]. In the case of a normalized wavefunction $\sum_i |\psi_i|^2 = 1$, the IPR_q takes the form,

$$I_q[\psi] = \sum_i |\psi_i|^{2q} \quad (4.10)$$

In particular for $q = 2$, one recovers the expression of the conventional IPR, which scales like the inverse volume of the effective support of the eigenfunction. If I_2 scales like $I_2 \sim L^{-D} \sim N^{-1}$, the wavefunction has support on the whole system, namely it is extended. On the contrary, a localized eigenmode has effective support on a finite portion of the system, implying that $I_2 \sim \text{cste}$. Similar properties carry out to the generalized IPR_q which is generally expected to exhibit a scaling of the kind

$$I_q \sim N^{-D_q(q-1)/D}, \quad (4.11)$$

with $D_q = D$ for extended states and $D_q = 0$ for localized states, expressing the effective dimensionality of the wavefunction support [69]. Yet an intermediate case between extended and localized states is offered by the so-called extended non-ergodic or multifractal states, namely states whose effective support is a set of zero measure in the spatial embedding in which the wavefunction is defined, yet this support diverges with system size exhibiting a sub-extensive scaling. A simple example could be offered by a wavefunction localized on a line of points

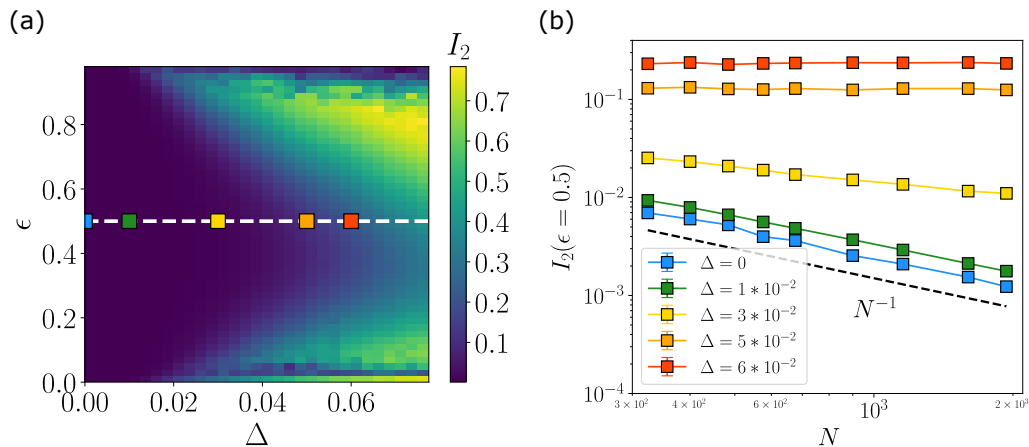


Figure 4.4: IPR and its scaling - (a) I_2 as a function of the energy density ϵ and the disorder parameter Δ , computed for a system of size 40×40 . (b) Scaling with the system size N of I_2 for several points along the line $\epsilon = 0.5$

in a two-dimensional system. In this case, the effective dimensionality is given by $D_q = 1$ (independent of q). More generally the effective dimensionality D_q is an irrational number, expressing the *fractal* nature of the wavefunction support; and it is dependent upon the index q , in which case one speaks of *multifractal* wavefunctions.

We propose to generalize this classification to the case of Bogoliubov eigenmodes $(\mathbf{u}^{(\alpha)}, \mathbf{v}^{(\alpha)})$ normalized so that $\sum_i [|u_i^{(\alpha)}|^2 - |v_i^{(\alpha)}|^2] = 1$. This normalization suggests that the role of the squared wavefunction $|\psi_i|^2$ is played here by the quantity $|u_i^{(\alpha)}|^2 - |v_i^{(\alpha)}|^2$, which, although not being non-negative a priori, turns out to be non-negative in all practical applications we considered. This is a physical consequence of the diluteness of the gas of Holstein-Primakoff bosons in the ground state: indeed the diluteness condition leads to $\langle \hat{n}_i \rangle = \sum_\alpha |v_i^{(\alpha)}|^2 \ll 1$, which implies a fortiori $|v_i^{(\alpha)}|^2 \sim \langle \hat{n}_i \rangle / N \ll 1$ for any α ; while in order for the mode to be correctly normalized, one needs $|u_i^{(\alpha)}|^2 = O(1/N)$, namely $|v_i^{(\alpha)}|^2 \sim \langle \hat{n}_i \rangle |u_i^{(\alpha)}|^2 \ll |u_i^{(\alpha)}|^2$. Hence, we introduce the generalized IPR $_q$ for the Bogoliubov modes in the form

$$I_q^{(\alpha)} = \sum_i \left[|u_i^{(\alpha)}|^2 - |v_i^{(\alpha)}|^2 \right]^q. \quad (4.12)$$

This quantity will be subject of our analysis in the following paragraph.

4.2.2 Scaling of the inverse participation ratio

The behaviour of I_2 as a function of the disorder parameter Δ and the normalized energy $\epsilon_\alpha = (\epsilon_\alpha - \epsilon_{\min}) / (\epsilon_{\max} - \epsilon_{\min})$, where $\epsilon_{\min, \max}$ are the extremal values of the LSW spectrum, is shown on Fig. 4.4. The inverse participation ratio is computed for $\Omega = |J_0|$ and averaged over windows of energy densities of width $\delta\epsilon = 0.02$, and then further averaged over several hundreds of disorder realizations. One can distinguish three regimes in the behaviour of I_2 :

1. At low disorder, namely for $\Delta \lesssim 10^{-2}$, all modes of the spectrum are extended.
2. For stronger disorder $10^{-2} \lesssim \Delta \lesssim 4 \cdot 10^{-2}$, the system lies in an intermediate regime where low- and high-energy eigenmodes exhibit a scaling with system size which is consistent with localized behavior, while the scaling properties of the medium part of the spectrum (namely $\epsilon = 0.5$ as shown on Fig. 4.4) suggest that the eigenmodes remain delocalized.
3. At high disorder, namely for $\Delta \gtrsim 4 \cdot 10^{-2}$, all eigenmodes undergo localization.

Indeed, Fig. 4.4 (b) shows how I_2 scales with system size for different values of the disorder parameter Δ for eigenmodes at energy density $\epsilon = 0.5$. For weakly disordered system ($\Delta = 0 - 0.01$) the inverse participation ratio displays a scaling compatible with an extended nature of eigenmodes. On the contrary, at high values of disorder ($\Delta = 0.05 - 0.06$), I_2 is size-independent, as expected from localized eigenmodes. For values of disorder standing in between these two limiting cases, however one finds that I_2 shows an algebraic scaling that will be further discussed in Sec. 4.2.4.

One can find this phenomenology puzzling since tight-binding Hamiltonians with short-range hopping in the absence of spin-orbit coupling and magnetic fields, possessing the same symmetries as those of the Gaussian orthogonal ensemble of random matrices, are not expected to exhibit a localization transition at finite disorder for dimension $D \leq 2$. However, the bosonic quadratic Hamiltonian treated in this study, despite describing spinless particles in the absence of (orbital) magnetic field, contains pairing terms that ascribe it to a different class of models whose localization properties are still far from being fully understood, leaving open the possibility for the system to undergo localization at finite disorder in $D = 2$, as pointed out by recent numerical studies [18]. One should not exclude however the possibility that the observed extended phase is actually a finite-size effect, and that localization occurs at any disorder but with a localization length that exceeds the system sizes explored in this study $\xi_l \gg L$. In that case one would not be able to grasp the truly localized nature of the eigenmodes unless one explores systems whose size compares with ξ_l .

4.2.3 Dynamical structure factor

As shown in [97], the extended versus localized nature of eigenmodes can also be probed via the properties of the dynamical structure factor defined as

$$S^{zz}(\mathbf{k}, \omega) = \int_{-\infty}^{+\infty} \frac{d\omega}{2\pi} \sum_{i,j} \frac{e^{i\mathbf{k} \cdot (\mathbf{r}_i - \mathbf{r}_j)}}{N} \langle 0 | S_i^z(t) S_j^z(0) | 0 \rangle_{\beta}. \quad (4.13)$$

Indeed, since disorder breaks translational invariance, Bloch's theorem does not apply anymore and the momentum \mathbf{k} cannot be used to label the eigenstates. As a result, contrarily to clean systems, the eigenmodes acquire a non-trivial structure

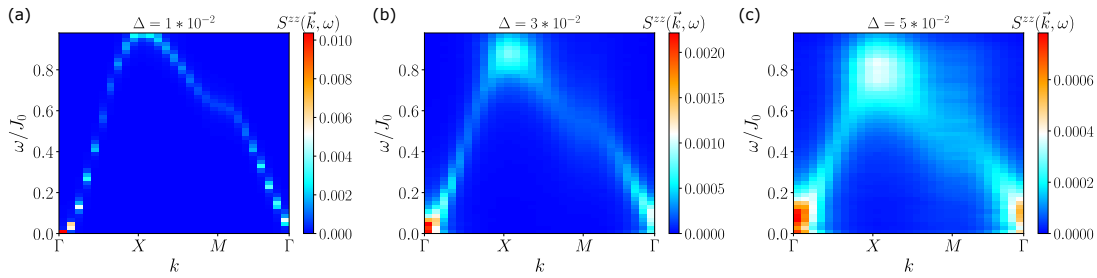


Figure 4.5: Spin-spin structure factor as a function of impulsion \mathbf{k} and energy density, computed for three values of the disorder parameter (a) $\Delta = 1 \cdot 10^{-2}$, (b) $\Delta = 3 \cdot 10^{-2}$, (c) $\Delta = 5 \cdot 10^{-2}$, all with the same system size 20×20

in momentum space and in particular the appearance of a finite momentum width in the case of localized eigenmodes whose localization length corresponds to the inverse of the width in question. The evolution of the structure factor can be easily accessed using linear spin-wave theory, which provides an expression of the dynamical structure factor in terms of the Bogoliubov coefficients $\mathbf{u}_i^{(\alpha)}$ and $\mathbf{v}_i^{(\alpha)}$, and the local mean-field angle θ_i ,

$$S^{zz}(\mathbf{k}, \omega) = \frac{S}{2N} \sum_{\alpha} \delta(\omega - \omega_{\alpha}) \left| \sum_i e^{-i\mathbf{k} \cdot \mathbf{r}_i} \sin \theta_i (u_i^{(\alpha)} + v_i^{(\alpha)}) \right|^2, \quad (4.14)$$

where δ stands for the Dirac distribution.

The dynamical structure factor computed for three different disorder parameters Δ in the three aforementioned regimes is shown on Fig. 4.5, as a function of momentum \mathbf{k} and of the energy density ϵ . One can indeed observe the same phenomenology as the one exhibited by I_2 : while at weak disorder the extended nature of the eigenmodes is preserved, as Δ increases the peaks of the dynamical structure factor start to acquire a finite momentum width as disorder increasingly localizes the eigenmodes, starting from the edges of the spectrum. Then, ultimately, the whole spectrum attains localization and a finite momentum width appears for modes at all energies. The dynamical structure factor therefore shows evidences of the transition toward localization.

4.2.4 Multifractal eigenmodes

In the intermediate regime of coexistence between localized and extended eigenmodes, the scaling of I_2 with system size (shown on Fig. 4.4) displays a power-law decay $I_2 \sim N^{-a}$ with an exponent $0 \leq a \leq 1$, which suggests that the effective support of the eigenmodes in the middle of the spectrum has non-integer dimensions, a property typical of fractals. In the following, we will investigate and identify the fractal properties of the eigenmodes lying in the intermediate regime of disorder.

In particular, the generalized inverse participation ratio I_q provides a tool to probe the possible multifractal nature of the eigenmodes, namely the property of

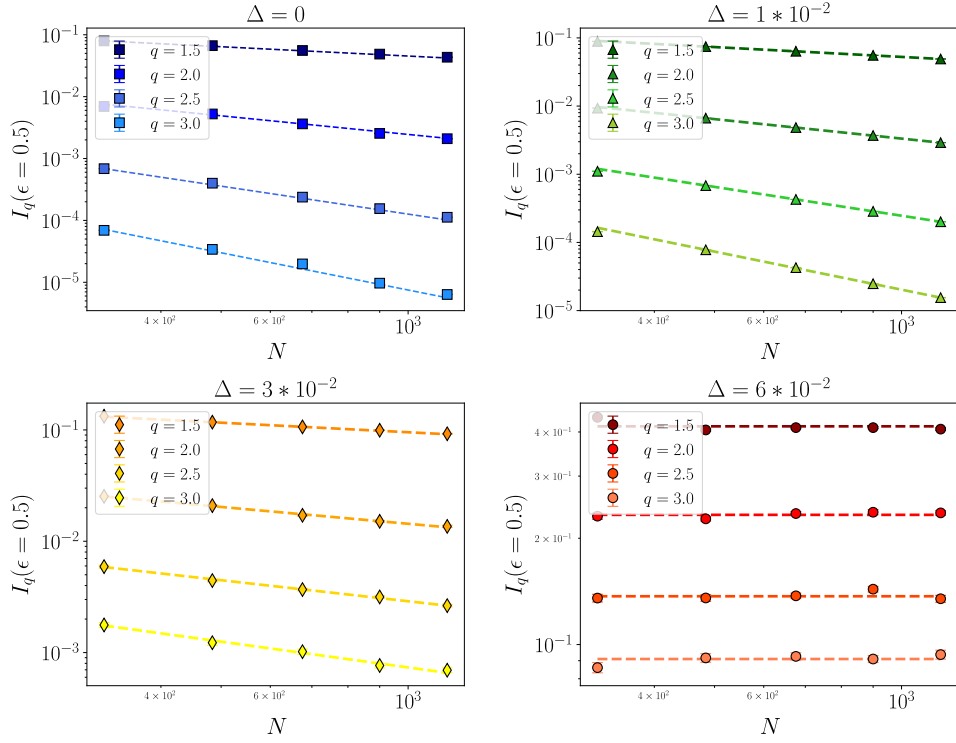


Figure 4.6: Generalized inverse participation ratio I_q at energy density $\epsilon = 0.5$) computed for four values of Δ , and four different values of q .

being described by an infinite number of dimensions D_q , governing the size-scaling of I_q as

$$I_q \sim N^{D_q(q-1)/D}. \quad (4.15)$$

D_q can be interpreted as the effective dimensions of the eigenmode's support revealed by I_q . Indeed, for all values of q , we expect to observe $D_q = D$ in the case of extended non-fractal eigenmodes, while $D_q = 0$ for localized eigenmodes. On the other hand, a q -dependent D_q signals the multifractal property of the eigenmode.

The scaling of I_q in the middle of the spectrum ($\epsilon = 0.5$) is shown on Fig. 4.6 for several values of q , while the dimensions extracted from the power-law fitting of I_q for linear sizes ranging from $L = 18$ to $L = 34$ are displayed on Fig. 4.7. As

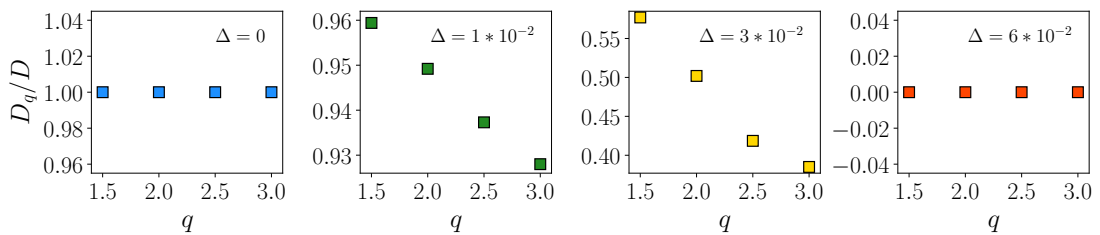


Figure 4.7: Anomalous dimensions corresponding to the curves shown on Fig. 4.6.

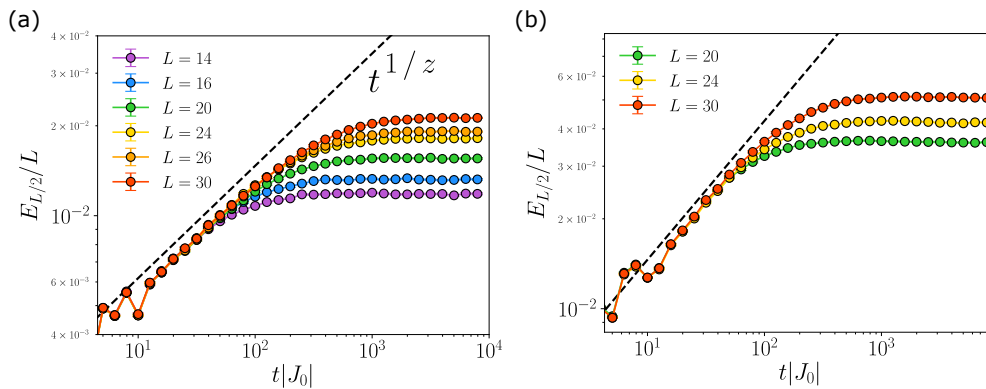


Figure 4.8: Entanglement entropy computed at $\Delta = 3 \cdot 10^{-2}$ for several linear system sizes L - (a) entanglement entropy computed for the full van der Waals interactions (b) entropy computed for truncated van der Waals couplings.

expected, for all values of q , $D_q = D$ in the clean case and $D_q = 0$ in the fully localized one; on the other hand in the mixed extended-localized case ($10^{-2} \lesssim \Delta \lesssim 4 \cdot 10^{-2}$) the effective dimension D_q is q -dependent, thus highlighting the multifractal nature of the mid-spectrum states.

4.3 Anomalous dynamics and localization

4.3.1 Entanglement entropy

Several numerical studies have evidenced a link between multifractal properties of eigenstates and anomalous diffusion, namely non-ballistic propagation of particles and/or information [69, 71, 73, 86, 103]. This connection between multifractality and dynamical properties provides a tool to probe the structure of the eigenmodes and record the transition toward localization by studying the quench dynamics of the system.

In the following, we will proceed according to the global quench protocol described in the previous chapter, namely the dynamics will be initialized from the mean-field state, which in terms of the linear spin-wave theory translates to the vacuum of the b -bosons. The post-quench evolution of this factorized uncorrelated state then leads to the build-up of correlations and entanglement via the generation of correlated pairs of bosons and their propagation through the lattice. Moreover, due to the Gaussian nature of the states described by linear spin-wave theory, entanglement entropy is readily computable. We then consider a two-dimensional toroidal system of size $L \times L$, and entanglement entropy $E_{L/2} = \text{Tr}[\ln \hat{\rho}_{L/2}]$ is computed for the reduced density matrix $\hat{\rho}_{L/2}$ of half of the torus (namely a system of size $L \times L/2$).

The asymptotic value of the entanglement entropy has very different scaling behaviours depending on whether the system is fully localized or still retains some extended eigenmodes. In the former case, entanglement entropy scales like the size of the interface between the subsystem and its complement, following a so-called

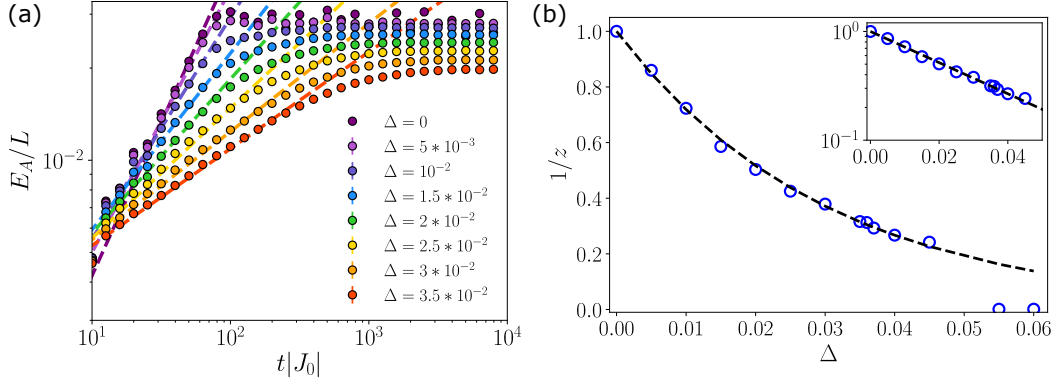


Figure 4.9: Disorder dependence of the growth of the entanglement entropy - (a) post-quench evolution of the entanglement entropy as a function of time for several values of the displacement parameter Δ (here $L = 30$) (b) power-law exponent z as a function of Δ . The dashed line shows an heuristic fit to an exponential decay $z = \exp(-\Delta/\delta)$.

area law; while in the latter entanglement entropy scales like the subsystem size according to a volume law. The results displayed in Fig. 4.8 show that at sizeable disorder corresponding to regime II (namely $\Delta = 3 \cdot 10^{-2}$) the entanglement at long-times does not follow an area-law scaling. This aspect further indicates the persistence of extended eigenmodes in spite of positional disorder; a finite occupation of bosons in such modes leads to the observed asymptotic scaling of entanglement. One can also notice that, unlike in the clean case, the growth of entanglement entropy is not linear, but instead follows a power-law growth of the form

$$E_{L/2} \sim t^{1/z}, \quad (4.16)$$

where $z \approx 2.8$ at the disorder ($\Delta = 3 \cdot 10^{-2}$) shown on Fig. 4.8. This power law growth, while manifesting itself as a transient behavior at short times for a given system size, appears to persist over longer time spans as the size increases, suggesting that it may persist indefinitely in the thermodynamic limit. This

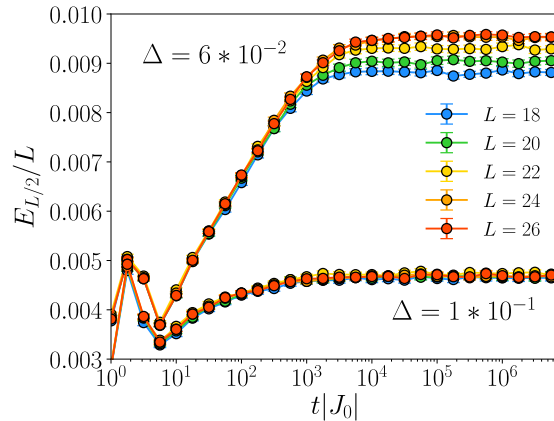


Figure 4.10: Dynamics of entanglement entropy in the localized regime (III) computed for two values of Δ ($\Delta = 6 \cdot 10^{-2}$ and $\Delta = 10^{-1}$)

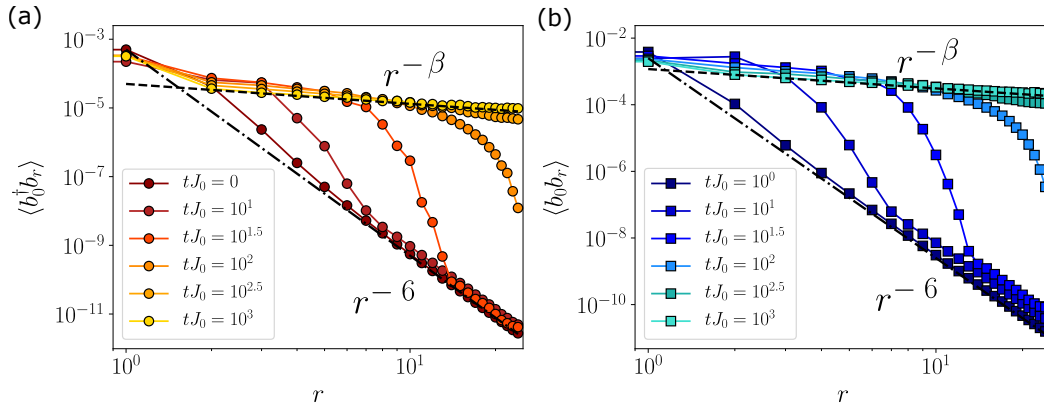


Figure 4.11: Evolution of the spatial structure of the two-point correlators following a global quench at disorder $\Delta = 2 \cdot 10^{-2}$ - (a) Green function (b) pairing function. Both quantities are computed for a system of size 50×50 and averaged over 500 realizations of disorder. Here $\beta \approx 0.58$.

behaviour is not an effect of the long-range nature of the van der Waals couplings as Fig. 4.8 also shows the evolution of entanglement entropy in the case where the tail of the van der Waals interactions is cut-off and couplings brought to zero for distances longer than $r_0 = \sqrt{2}$, there we observe that entanglement entropy still displays a power-law growth, albeit with a different exponent $z \approx 2.2$.

Repeating the study of the growth of entanglement entropy for various disorder strengths, (Fig. 4.9) the results suggest that the exponent z grows continuously from $z = 1$ in the clean case to span the sub-ballistic ($1 < z < 2$) and sub-diffusive regimes ($z \geq 2$), until the system reaches localization, at which z should diverge. The behaviour of entanglement entropy in the localized regime is shown in Fig. 4.10. Sufficiently close to the localization transition ($\Delta = 6 \cdot 10^{-2}$), the entanglement entropy seems to grow logarithmically in time before reaching a saturation regime seemingly described by an area law (at least for the larger systems sizes considered here) consistent with Anderson localization. For an even stronger disorder ($\Delta = 10^{-1}$) the apparent logarithmic growth at short times disappears, and a clear area-law scaling is observed at all times and for all the sizes we considered.

4.3.2 Correlation functions

Since linear spin-wave theory describes Gaussian states, the post-quench evolution of entanglement entropy as well as of any other quantity descends from the dynamics of the Green functions $\langle b_i^\dagger b_j \rangle$ and the anomalous Green functions $\langle b_i b_j \rangle$. Therefore, one expects to observe into the Green functions the anomalous diffusion that is exhibited by the entanglement entropy.

The evolution of the two-point correlators is characterized by the instantaneous post-quench emergence of an algebraic spatial profile of the form r^{-6} due to

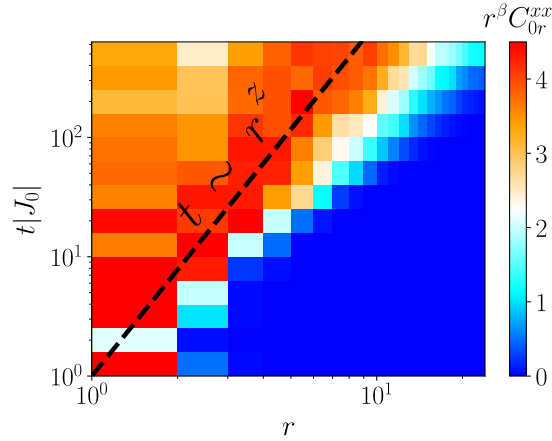


Figure 4.12: Spin-spin correlation function and light-cone effect in a system of size 50×50 at disorder $\Delta = 3 \cdot 10^{-2}$.

the van der Waals form of the couplings. Then as quasi-particles propagate, correlations build-up and stabilize an emergent disorder-dependent spatial structure of the form $r^{-\beta}$, with $\beta < 6$, within the boundaries of a light-cone which opens up sub-ballistically. The evolution of the correlators is shown on Fig. 4.11 for a value of disorder ($\Delta = 2 \cdot 10^{-2}$) that corresponds to the intermediate regime of co-existence between extended and localized eigenmodes. The asymptotic algebraic decay of correlations is another consequence of the non-ergodic (algebraically localized) nature of the eigenmodes, moreover it deviates strongly from what one would expect at thermal equilibrium namely an r^{-6} decay imposed by the long-range interactions. Hence the asymptotic behavior represents a pre-thermalized regime, dominated by the integrable nature of the linearized spin-wave Hamiltonian.

The spin-spin correlation function for e.g. the x -spin component, being expressed in terms of the two-point Green functions, provides a straightforward platform to probe both the subdiffusive propagation of information through a curved light cone with an algebraic aperture $t \sim r^z$, where z is the exponent governing the growth of entanglement entropy; as well as the non-ergodic nature of the eigenmodes via the algebraic decay of the asymptotic correlations. In terms of the two-points correlators, the spin-spin correlation function for the x -spin components reads

$$C^{xx}(\mathbf{r}_i, \mathbf{r}_j; t) = \sin \theta_i \sin \theta_j \left(\langle \hat{b}_i^\dagger \hat{b}_j \rangle \langle \hat{b}_i \hat{b}_j^\dagger \rangle + \langle \hat{b}_i^\dagger \hat{b}_j^\dagger \rangle \langle \hat{b}_i \hat{b}_j \rangle \right) + \frac{S}{2} \cos \theta_i \cos \theta_j \left(\langle \hat{b}_i^\dagger \hat{b}_j \rangle + \langle \hat{b}_i \hat{b}_j^\dagger \rangle + \langle \hat{b}_i^\dagger \hat{b}_j^\dagger \rangle + \langle \hat{b}_i \hat{b}_j \rangle \right). \quad (4.17)$$

The correlation function, multiplied by r^β (with $\beta \approx 1.1$) in order for the light-cone structure to be more visible, is represented on Fig. 4.12, and as expected it shows a sub-ballistic light cone which further highlights the anomalous diffusion of correlations in the model at hand. More importantly, the exponent z extracted

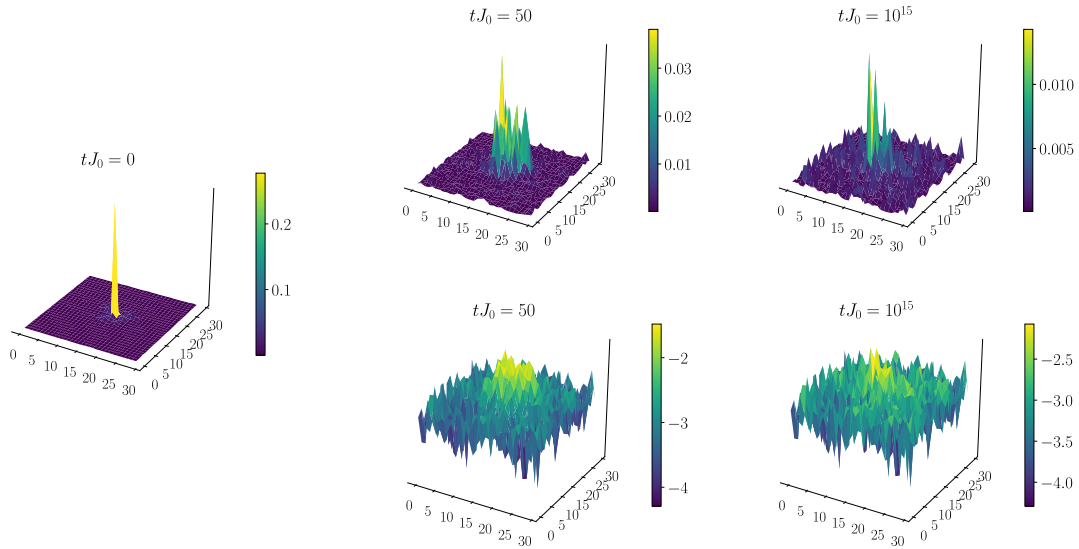


Figure 4.13: Local excess density of bosonic excitations δn_i as a function of time computed for $\Delta = 3 \cdot 10^{-2}$ for a system of size 30×30 . The upper row shows the density profile on linear scale while the lower row displays the same density profiles in logarithmic scale.

from the study of entanglement entropy is consistent with the one piloting the aperture of the light cone.

4.3.3 Probing multifractality via quench dynamics

In the previous chapter, we introduced a second quench protocol (local + global quench) which is complementary to the global quench protocol in the sense that it enables to target the excitation of specific eigenmodes. In the following, we will use this quench protocol to highlight the multifractal structure of eigenmodes in the intermediate regime of disorder.

The locally quenched system from which we initialize the dynamics is the mean-field state, on top of which a single spin is flipped at the injection site j , resulting in the addition of a single b -boson $|\Psi_0\rangle = \hat{b}_j^\dagger |\Psi_{\text{MF}}\rangle$. Therefore, the flipping of a spin at site j leads to a local excess in the density of the Bose gas of excitations. We record the evolution of this excess density compared to the density of quasi-particles induced by a global quench, as encoded in the quantity δn_i defined as

$$\delta n_i(t) = \langle \Psi_{\text{MF}} | \hat{b}_j \hat{n}_i(t) \hat{b}_j^\dagger | \Psi_{\text{MF}} \rangle - \langle \Psi_{\text{MF}} | \hat{n}_i(t) | \Psi_{\text{MF}} \rangle, \quad (4.18)$$

which corresponds to the local density of bosons following a local spin-flip. This excess density of bosonic excitations, from a peak localized at injection site j , is expected to progressively spread via the most extended eigenmodes that overlap with site j , thereby exposing their spatial structure -either extended, multifractal or localized. This is particularly important in the regime in which the most

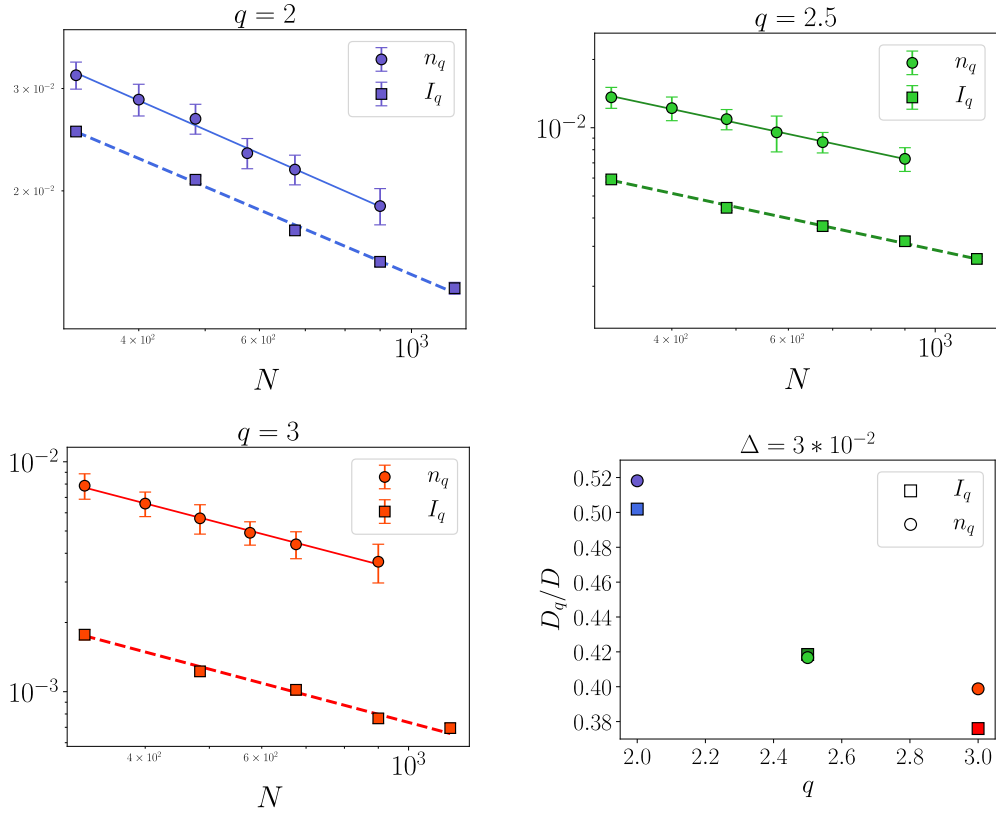


Figure 4.14: Size scaling of n_q compared to the generalized participation ratio and corresponding effective dimension at $\Delta = 3 \cdot 10^{-2}$.

extended eigenmodes are multifractal, as shown in Fig. 4.13. Identifying the asymptotic density profile with its time-average, we obtain an expression for δn_i at long times as

$$\delta n_i(t \rightarrow \infty) = \sum_{\alpha} \left[(u_i^{(\alpha)})^2 + (v_i^{(\alpha)})^2 \right] \left[(u_j^{(\alpha)})^2 + (v_j^{(\alpha)})^2 \right]. \quad (4.19)$$

This expression shows that modes that contribute the most to the long-time excess density are those that have a significant overlap with both site j as well as site i -namely δn_i reflects the spatial structure of modes that are *centered* around j and that extend all the way to site i . To analyze their spatial structure, we investigate their generalized inverse participation ratio defined as

$$n_q = \sum_i [\delta n_i(t \rightarrow \infty)]^q, \quad (4.20)$$

since $\sum_i \delta n_i \approx 1$. We can then deduce from the finite-size scaling of this quantity a q -dependent multifractal dimension of the density profile, noted D'_q dictating the power-law scaling of n_q

$$n_q \sim N^{-D'_q(q-1)/D}. \quad (4.21)$$

Such a scaling is indeed evidenced by Fig. 4.14 at disorder $\Delta = 3 \cdot 10^{-2}$. The size- and q -dependent behaviours of n_q are compared with the scaling of the

generalized inverse participation ratio I_q of the mid-spectrum eigenmodes (being the ones that are most extended) for the same value of the disorder parameter. For all considered values of q , the generalized inverse participation ratios for the eigenmodes and for the excess density show similar scaling properties, resulting in close multifractal dimensions. This similarity in the respective behaviours of n_q and I_q can be understood a posteriori given the value of the disorder parameter at which this study is conducted, namely $\Delta = 3 \cdot 10^{-2}$. For this intermediate disorder regime, the low- and high-energy eigenmodes are localized, and the remaining extended ones lie in the middle of the spectrum, namely at the energy density $\epsilon \simeq 0.5$. As a result, the eigenmodes that contribute the most to the propagation of the spin flip are localized at $\epsilon = 0.5$.

4.4 Conclusions

In this chapter, we illustrated the stark dichotomy between equilibrium and out-of-equilibrium properties exhibited by a positionally disordered quantum many-body system that can be realistically implemented in Rydberg-atoms simulators. Similar physics could also be explored with trapped ions in microtrap arrays. We evidenced how the non-ergodic and multifractal nature of the eigenmodes could be explored via the properties of a rich post-quench dynamics ranging continuously from ballistic to sub-diffusive and to localized. This study is also relevant for experiments in light of the high sensitivity to disorder of van der Waals interactions, and the positional disorder that thermal fluctuations can induce in trapped-atoms arrays [61].

Gaussian Ansatz approaches to non-linear spin dynamics

*”Je t’ai vu grandir comme un arbre,
Inénarrable éternité ;
Je t’ai vu durcir comme un marbre,
Indicible réalité.”*

Marguerite Yourcenar, ”Vers gnomiques”

5.1 Interacting spin systems

5.1.1 Motivations

Despite its seemingly simplistic formulation, linear spin-wave theory provides an insightful framework to explore exotic dynamical effects, such as localization through Aharonov-Bohm caging, or anomalous diffusion and multifractality in geometrically disordered spin systems. However, linear spin-wave theory is inherently limited by the amount of excitations on top of a mean-field reference state that can be faithfully described without accounting for their interactions, and this limitation prevents the theory from correctly describing high-energy quenches. Moreover, the linearization of the Hamiltonian implies that the system is approximated in terms of an integrable model, whose dynamics leads to an equilibration towards a state described by the Generalized Gibbs Ensemble (GGE), thus failing to reach proper thermalization.

Searching for an approach beyond the linearized picture provided by linear spin-wave theory opens new ways towards the study of many-body dynamics far from equilibrium, in cases where the effects of interactions on dynamics cannot be neglected. Extending linear spin-wave theory beyond the dilute regime also enables to consider quenches that are more realistically implemented in cold-atom experiments. In the following, we will apply the Gaussian Ansatz approach sketched in Sec. 2.2.2 to the transverse-field Ising model, first for a

one-dimensional chain - for which an exact solution is available - and then for the two-dimensional square lattice.

5.1.2 Non-linear spin-wave Hamiltonian

The physics of one-dimensional systems, characterized by strong non-linear fluctuations [41], typically expose the linear approach to spin-wave theory to the limits of its relevance. Moreover, as we discussed in Sec. 2.3.1, the transverse-field Ising chain admits an exact description in terms of free fermions, and therefore its dynamics is constrained to conserve an extensive number of integrals of motion. The transverse-field Ising chain, as it lies beyond what can be accurately described by linear spin-wave theory, provides at the same time a suitable benchmarking test for a Gaussian-state approach to non-linear spin dynamics.

In order to lead this comparative study between the results of the Gaussian Ansatz (GA) and the free fermions (FF) exact solution, we will initialize the dynamics in a simple state, namely the spin configuration where every spin is polarized along the transverse-field,

$$|\Psi_0\rangle = \bigotimes_i |\rightarrow\rangle_i, \quad (5.1)$$

which in the particle image of spins -either bosonic or fermionic- corresponds to a vacuum of quasiparticles.

Choosing the direction of the transverse field as the quantization axis z' of the transverse-field Ising model, the corresponding Hamiltonian then reads

$$\hat{\mathcal{H}} = -\frac{1}{2} \sum_{i,j} J_{ij} \hat{S}_i^{x'} \hat{S}_j^{x'} - \Omega \sum_i \hat{S}_i^{z'}. \quad (5.2)$$

As discussed in Chapter 2, linear spin-wave theory starts from a bosonization of the spin operators based on the Holstein-Primakoff transformation, the resulting Bose gas is then assumed to be dilute enough to linearize the expression of spin operators in terms of the bosonic operators. Still under the assumption that the amount of quasiparticles is small, one can bring one step further the Taylor expansion of the square-root term present in the transformation as follows

$$\hat{S}_i^+ = \sqrt{2S - \hat{b}_i^\dagger \hat{b}_i} \hat{b}_i = \sqrt{2S} \left(1 - \frac{1}{2} \frac{\hat{b}_i^\dagger \hat{b}_i}{2S} \right) \hat{b}_i + O(\hat{b}_i^3). \quad (5.3)$$

This results in the appearance of quartic terms in the Hamiltonian, describing pair creation/destruction and hopping modulated by local quasiparticle occupation:

$$\begin{aligned} \hat{\mathcal{H}} \simeq & -N\Omega S - \frac{S}{4} \sum_{i,j} J_{ij} (\hat{b}_i^\dagger + \hat{b}_i) (\hat{b}_j^\dagger + \hat{b}_j) + \Omega \sum_i \hat{b}_i^\dagger \hat{b}_i \\ & + \frac{1}{16} \sum_{i,j} J_{ij} \left[(\hat{b}_i^\dagger + \hat{b}_i) (\hat{b}_j^\dagger \hat{b}_j^\dagger \hat{b}_j + \hat{b}_j^\dagger \hat{b}_j \hat{b}_j) + (\hat{b}_i^\dagger \hat{b}_i^\dagger \hat{b}_i + \hat{b}_i^\dagger \hat{b}_i \hat{b}_i) (\hat{b}_j^\dagger + \hat{b}_j) \right]. \end{aligned} \quad (5.4)$$

The unitary evolution of the system governed by this Hamiltonian is tackled by using the dynamical Gaussian Ansatz framework we established in Chapter 2. Within that Ansatz, the system is fully described by the two-point correlators $G_{ij} = \langle \hat{b}_i^\dagger \hat{b}_j \rangle$ and $F_{ij} = \langle \hat{b}_i \hat{b}_j \rangle$ - while $c_i = \langle \hat{b}_i \rangle = 0$ as the Hamiltonian only contains even terms. The evolution of two-point correlators is driven by a set of first-order non-linear differential equations (given in Appendix D) that can be solved numerically for a set of initial conditions corresponding to the two-point correlators of the initial Gaussian state.

The mapping of spins onto bosons requires to set bounds to the elements of the covariance matrix of the bosonic Gaussian state in order for it to be compatible with the physics of spin degrees of freedom. These constraints impose consistency between the bosonic and spin Hilbert spaces, and form in principle an infinite set of conditions, but for practical purposes we shall limit ourselves to conditions referred to single-spin and spin-spin observables:

1. the expectation value of all spin components shall obey to the relation $|\langle \hat{S}_i^\alpha \rangle| \leq S$,
2. the spin-spin correlation functions for all components are expected to obey the inequality $|\langle \hat{S}_i^\alpha \hat{S}_j^\beta \rangle - \langle \hat{S}_i^\alpha \rangle \langle \hat{S}_j^\beta \rangle| \leq S^2$.

Neither linear spin-wave theory nor the Gaussian Ansatz approach are bound to satisfy the above constraints, and therefore the predictions should be considered as physical only when the above criteria are met. Except when stated otherwise, all the results presented in this chapter have been tested to satisfy the above criteria.

5.2 Transverse-field Ising chain

5.2.1 Fermionic and bosonic images of dynamics

It is very instructive at this point to contrast the exact solution of the transverse-field Ising chain in terms of free fermions with the picture offered by spin-wave theory, linear and non-linear. As seen in Sec. 2.3.1, the Jordan-Wigner transformation allows one to map the transverse-field Ising chain into the free-fermion Hamiltonian [74]

$$\hat{\mathcal{H}} = \sum_{\mathbf{k}} \epsilon_{\mathbf{k}} \left(\hat{\eta}_{\mathbf{k}}^\dagger \hat{\eta}_{\mathbf{k}} - \frac{1}{2} \right), \quad (5.5)$$

where $\epsilon_{\mathbf{k}} = \Omega \sqrt{1 + \lambda^2 - 2\lambda \cos \mathbf{k}}$ and $\lambda = J/(2\Omega)$. On the other hand, linear spin-wave theory amounting to the Hamiltonian Eq. (5.4) in which only the quadratic terms are retained, describes the $S = 1/2$ spin chain in terms of free bosons as

$$\hat{\mathcal{H}}_{\text{LSW}} = -\frac{N\Omega}{2} - \sum_{\mathbf{k}} \tilde{\epsilon}_{\mathbf{k}} \hat{\beta}_{\mathbf{k}}^\dagger \hat{\beta}_{\mathbf{k}}, \quad (5.6)$$

with $\tilde{\epsilon}_{\mathbf{k}} = \Omega\sqrt{1 - \tilde{\lambda}\cos\mathbf{k}}$ and $\tilde{\lambda} = J/\Omega$. Hence applying spin-wave theory to the Ising chain for strong polarizing fields amounts to trying to mimicking a free Fermi gas via a free Bose gas. This approach can only be successful in the limit of a very dilute gas, in which the statistics of the particles plays a minor role. At higher densities instead, the results are expected to differ significantly: the Holstein-Primakoff transformation indeed describes the $S = 1/2$ spin system as a gas of hardcore bosons, as a consequence strong non-linearities are necessary to have a faithful bosonic description of the fermionic gas. A first step in this direction is precisely taken by non-linear spin-wave theory. The purpose of the following analysis is precisely that of assessing the latter approach.

5.2.2 Quench dynamics of the transverse magnetization

Choosing the polarized state as the initial state for the dynamics amounts to preparing the system in the ground state at infinite transverse field ($\Omega = +\infty$), and evolving it with finite field. The value Ω of the transverse field then tunes the strength of the quench: the weaker the field, the further the polarized state is from the ground state of the post-quench Hamiltonian. The most extreme cases correspond to when Ω crosses the critical value ($\Omega_c = 0.5J$) below which the ground state exhibits ferromagnetic order. The evolution of the expectation value of the transverse magnetization

$$m^x = \frac{1}{N} \sum_i \langle \hat{S}_i^x \rangle = S - \frac{1}{N} \sum_i \langle \hat{b}_i^\dagger \hat{b}_i \rangle, \quad (5.7)$$

computed using the Gaussian Ansatz and compared to the exact solution is shown on Fig. 5.1 for three different values of the transverse field lying above, below and at the critical field. Fig. 5.1 (a) shows an example of a "small" quench with $\Omega = 3\Omega_c = 1.5J$, keeping the field well above the transition point. We observe that this quench keep the transverse magnetization close to its initial value, implying the appearance of a gas of fermionic quasiparticles (in the exact solution) or bosonic quasiparticles (within spin-wave theory) of very low density. While this feature is correctly captured by linear spin-wave theory, we observe that the latter theory predicts an asymptotic value which is lower than the exact one (namely it overestimates the density of quasiparticles), and oscillations around the asymptotic value which are far more persistent and possess a significantly lower frequency than the exact solution. This reveals in particular the fact that linear spin-wave theory predicts an incorrect excitation spectrum and persistent oscillations in the absence of non-linearities. All these artifacts are corrected by the inclusion of non-linearities at the level of the Gaussian Ansatz, which recovers at once the correct asymptotic value of the transverse magnetization, and the correct frequency of the oscillations as well as the correct time scale for their damping.

Remarkably, the Gaussian Ansatz is able to reproduce the dynamics of the spin chain in regimes where linear spin-wave theory breaks down. Indeed, for values of the transverse field lying below the critical value predicted by the mean-field approximation, namely $\Omega_c^{\text{MF}} = J$, imaginary frequencies arise in the linear

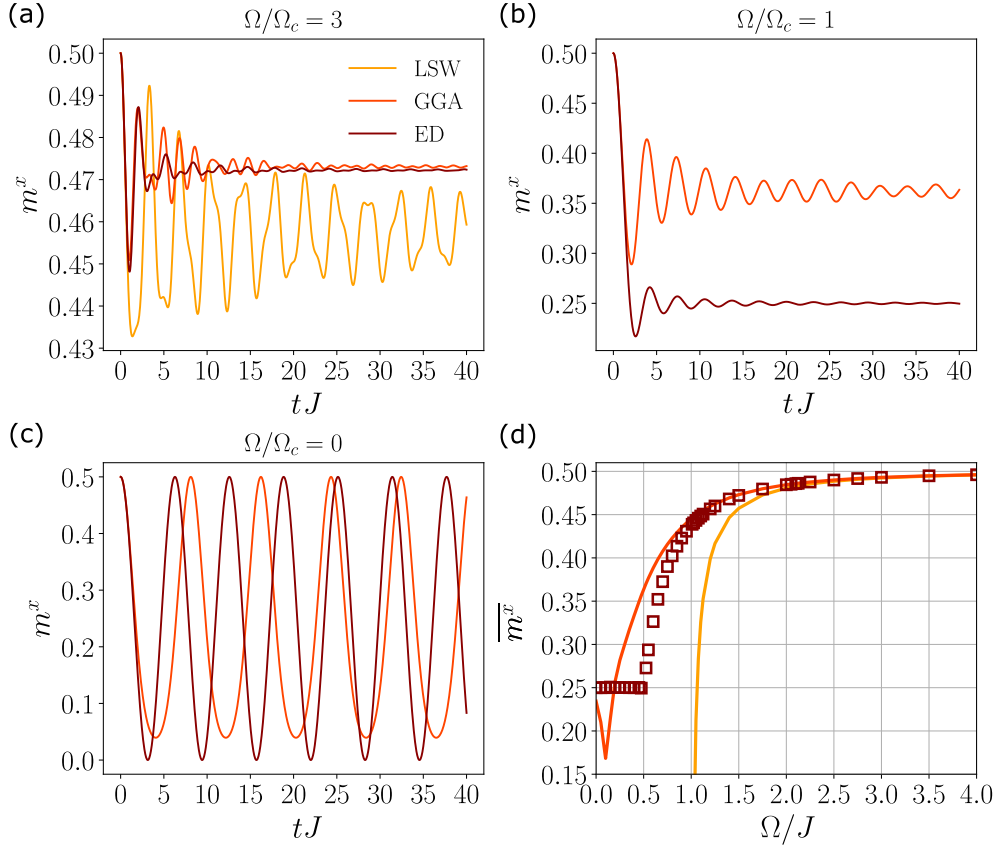


Figure 5.1: Quench dynamics of the transverse field Ising chain - (a) (b) and (c) represent the transverse magnetization m^x as a function of time, computed for a chain of length $N = 50$ at three values of the transverse field $\Omega = 3\Omega_c$, $\Omega = \Omega_c$, $\Omega = 0$. (d) represents the transverse magnetization as a function of the transverse field averaged over a time-window of width $40J$.

spin-wave spectrum, leading to the dynamical instabilities. On the other hand the Gaussian approach remains stable in these regimes of strong quenches, as illustrated on Fig. 5.1 (b)-(c) for transverse fields such as $\Omega = \Omega_c$ and $\Omega = 0$. In these two cases, the agreement between the exact solution and the Gaussian Ansatz on the asymptotic value of the transverse magnetization becomes less quantitative, yet the main features of the dynamics are still well captured. On Fig. 5.1 (b), referring to a quench with $\Omega = \Omega_c$, one can observe that, while overestimating the asymptotic value compared to the exact result, the Gaussian Ansatz captures correctly the frequency of the oscillations around that value and it also shows damping of such oscillations although with an underestimated damping rate. As for Fig. 5.1 (c), it describes the extreme case where $\Omega = 0$; although the oscillations exhibited by the Gaussian Ansatz do not fit perfectly the exact result, both the frequency and the amplitude are rather close to exact behaviour of the spins, despite the high densities of quasiparticles generated by the quench.

The comparison between the linear spin-wave theory, the Gaussian Ansatz and the exact result is summarized on Fig. 5.1 (d), where the time-averaged transverse

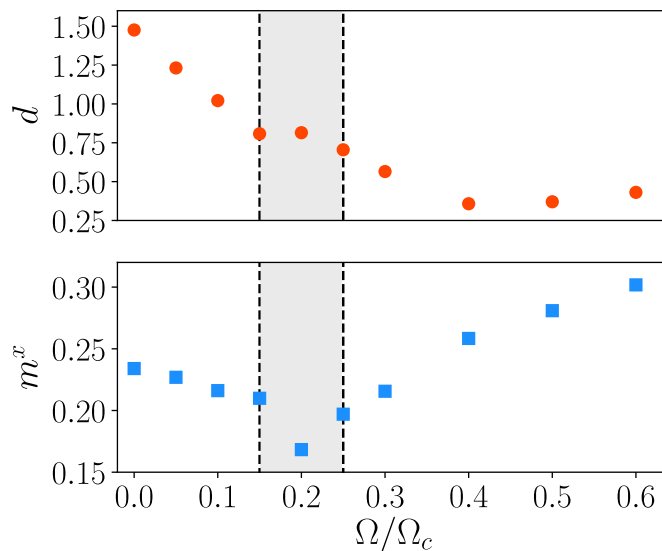


Figure 5.2: Performances of the Gaussian Ansatz for a transverse-field Ising chain of $N = 50$ sites. The upper panel shows the distance d between the exact solution and the Gaussian solution as a function of the transverse field, while the lower panel displays the evolution of the equilibrium magnetization, also as a function of the transverse field.

magnetization is represented as a function of the transverse field, or in other words as a function of the strength of the quench. While linear spin-wave theory only gives accurate predictions for the time-averaged magnetization for small quenches and then becomes unstable at $\Omega = \Omega_c^{\text{MF}}$, the Gaussian Ansatz provides quantitative results for all values of Ω , with a generically good agreement with the exact solution except at a point around $\Omega \simeq 0.1J$, where the time-averaged magnetization decreases below the exact value of $m^x = 0.25$ before showing a cusp and going back up toward the exact solution. In this restricted area, the solutions of the non-linear equations of motion display numerical instabilities.

To gain a global insight into the ability of the Gaussian Ansatz to reproduce the dynamics of the transverse magnetization, one can look at a measure of the distance d between the exact solution (free fermions) and the Gaussian Ansatz,

$$d = \|m_{\text{FF}}^x - m_{\text{GA}}^x\|_2, \quad (5.8)$$

where $\|\cdot\|_2$ accounts for the 2-norm defined on $L^2([0, T])$ as

$$\|f\|_2 = \left(\int_0^T dt |f(t)|^2 \right)^{1/2}, \quad (5.9)$$

with T being the upper bound of the time considered during the evolution of the system.

The performances and accuracy of the Gaussian Ansatz are tested for low values of the transverse field, namely for the strongest quenches, in conditions where the approach is most likely to break down. As illustrated by Fig. 5.2,

the distance d between the exact and the Gaussian solution remains relatively small for $\Omega > 0.2\Omega_c = 0.1J$, but it increases significantly below this value; most importantly in that range of spin-spin correlation functions are predicted by the Gaussian Ansatz to take unphysical values (exceeding S^2). Nonetheless, as illustrated on Fig. 5.1 (c), the dynamics of the transverse magnetization still retains some of the main features of the exact solution.

A possible path to incrementally improve the results provided by the Gaussian approach could be to expand the Holstein-Primakoff transformation to the higher orders, thus including new terms to the Hamiltonian. This strategy however would imply to manipulate $2n$ -points correlators expanded into the sum of $(2n - 1)!!$ products of n two-points correlators.

5.2.3 Spin-spin correlation functions

The picture provided by the dynamics of the transverse magnetization however is not sufficient to assess the efficiency of the Gaussian approach, as it only involves the diagonal elements of the covariance matrix. To complete the picture, it is necessary to study how quantities involving the off-diagonal terms of the covariance matrix compare to the exact solution. A readily computable example is the spin-spin correlations for the x spin components:

$$\begin{aligned} C^{xx}(\mathbf{r}_i - \mathbf{r}_j; t) &= \langle \delta \hat{S}_i^x \delta \hat{S}_j^x \rangle = \langle \hat{S}_i^{z'} \hat{S}_j^{z'} \rangle - \langle \hat{S}_i^{z'} \rangle \langle \hat{S}_j^{z'} \rangle \\ &= \langle \hat{b}_i^\dagger \hat{b}_j \rangle \langle \hat{b}_i \hat{b}_j^\dagger \rangle + \langle \hat{b}_i^\dagger \hat{b}_j^\dagger \rangle \langle \hat{b}_i \hat{b}_j \rangle. \end{aligned} \quad (5.10)$$

The correlation functions computed via linear spin-wave theory and the Gaussian Ansatz are compared to the exact solution in Fig. 5.3. In all cases, we observe a light-cone structure of the correlation with comparable Lieb-Robinson velocities; yet linear spin-wave theory fails to reproduce the inner structure of the light cone as it exhibits undamped oscillations of correlations at all distances. The Gaussian Ansatz, on the other hand, reproduces more accurately the structure of the correlations with strongly damped oscillations.

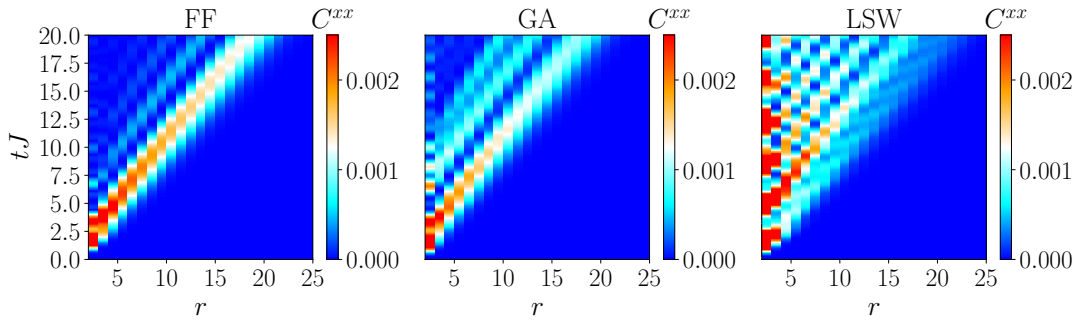


Figure 5.3: Spin-spin correlation function along the x -axis as a function of distance r between two sites and time. The results shown here are computed for $N = 50$ and $\Omega/\Omega_c = 3$.

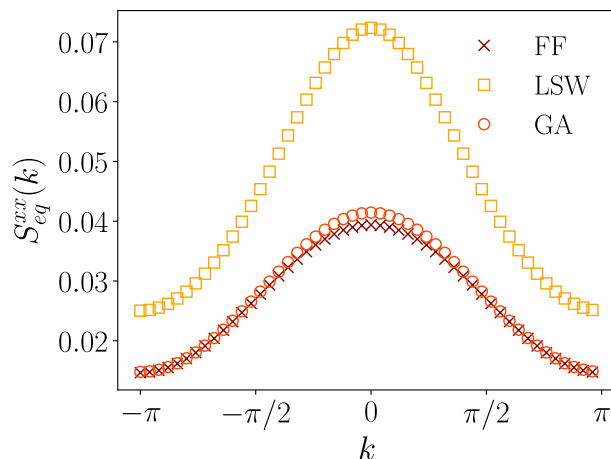


Figure 5.4: Time-averaged structure factor computed for a chain of length $N = 50$ at a transverse-field value of $\Omega/\Omega_c = 3$.

Fig. 5.3 probes the ability of spin-wave theories to reproduce the dynamical behaviour of correlations but it does not illustrate whether such approaches are able to reproduce the asymptotic structure of correlations at long times. To do so, we focus our attention on the time-averaged spin-spin structure factor for x spin components, defined as the Fourier transform of correlations,

$$S_{\text{eq}}^{xx}(\mathbf{k}) = \frac{1}{T} \int_0^T dt \sum_{i,j} e^{i\mathbf{k}\cdot(\mathbf{r}_i - \mathbf{r}_j)} C^{xx}(\mathbf{r}_i - \mathbf{r}_j; t). \quad (5.11)$$

Fig. 5.4 shows the time-averaged structure factor for the same value of transverse field and the same chain length as the ones used to compute the correlation functions shown in Fig. 5.3. All three curves represented on the figure exhibit a Lorentzian-like profile consistent with an exponential decay of the correlation functions. Yet, linear spin-wave theory significantly overestimates the strength of correlations, while the Gaussian Ansatz provides an accurate description of the structure of correlations at long times.

5.2.4 Entanglement entropy

The full structure of the covariance matrix of a sub-system enters in the entanglement entropy, which can be computed for the exact free-fermion picture as well as for bosonic Gaussian states. The evolution of entanglement entropy is expected to be characterized by two properties : the time necessary to observe a saturation, and the value taken by entanglement entropy at the saturation plateau. Indeed, the time t^* necessary for entanglement entropy to reach saturation is controlled by the propagation of excitations, or more precisely by their maximum group velocity. An accurate relaxation time is therefore suggestive of a faithful reproduction of the spectral properties of the excitations. On the other hand, if the entanglement at saturation is reproduced faithfully, this suggests that the statistical ensemble describing the equilibrium state is properly addressed. This last point is particularly significant in the case of the one-dimensional transverse-

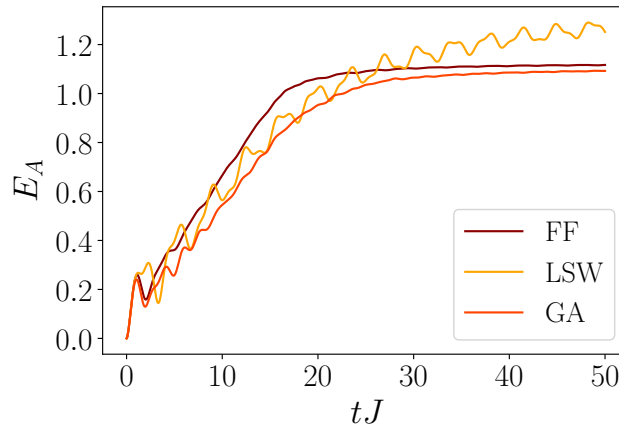


Figure 5.5: Entanglement entropy as a function of time computed for a chain of $N = 150$ sites with periodic boundary conditions. The subsection A is a segment of size $N_A = N/10$ and the transverse field used for the calculation is $\Omega/\Omega_c = 3$

field Ising model due to its integrability and, consequently, to the existence of conserved quantities that constrain the generalized Gibbs ensemble describing long-time behaviour.

An illustration of the comparative evolution of entanglement entropy is shown in Fig. 5.5, entanglement entropy being computed for a chain with boundary conditions of length $N = 150$, the subsection considered here being a tenth of the total chain. As it was already indicated by the study of the transverse magnetization and correlations, linear spin-wave theory fails to capture both the relaxation dynamics of the system following the quench and the state toward which it equilibrates. The entanglement entropy computed by means of the Gaussian approach shows a significant improvement compared to linear spin-wave theory, in the sense that reproduces well the general behaviour of the exact solution - namely a linear growth of entanglement up to a plateau close to the prethermal value of the integrable model. We observe however a discrepancy in the relaxation times between the Gaussian Ansatz and the exact solution: the entanglement entropy described by the former relaxes more slowly than the latter, indicating that the maximum group velocity of excitations described by the Gaussian approach is smaller than expected and that, as a result, the finer details of the excitation spectrum are not perfectly reproduced.

5.3 Transverse-field Ising model on the square lattice

5.3.1 From the chain to the square lattice

In contrary to the one-dimensional case of a chain, the transverse-field Ising model on the square lattice is not integrable, and while the thermal state toward which

the post-quench dynamics bring the system can be described by quantum Monte Carlo calculations, the study of the dynamics itself for large systems calls for the use of approximate methods. The substantial improvement over linear spin-wave theory offered by the inclusion of non-linearities within the Gaussian Ansatz, in the case of the Ising chain, encourages us to look into the predictions of the latter approach for systems in higher dimensions.

Indeed, the distinctive traits of one-dimensional physics, namely strong fluctuations and interactions, are expected to be weaker in the physics of systems of high dimensions. In particular, the density of bosonic quasiparticles is expected to be generically smaller and consequently the importance of non-linearities should be weaker. Moreover, as shown in Sec. 2.2.1, the Gaussian Ansatz as formulated in Takahashi's modified spin-wave theory showed an accurate description of the ground state of the transverse-field Ising model on the square lattice. These considerations suggest the possibility that the Gaussian Ansatz may provide accurate results as well as for the non-equilibrium quantum dynamics.

In the following, the Gaussian approach is applied to two types of initial states. The first case we will consider is the same as the one we used to test the Gaussian Ansatz:

1. the system is initialized from the state where the all spins are aligned along the field direction

$$|\Psi_0\rangle = \bigotimes_i |\rightarrow\rangle_i, \quad (5.12)$$

which equates to quenching the system from an infinite to a finite field ($\infty \rightarrow \Omega$).

2. The second type of quenches considered hereafter starts from the ferromagnetic state where all spins are aligned along the z -axis

$$|\Psi_0\rangle = \bigotimes_i |\uparrow\rangle_i, \quad (5.13)$$

which amounts to turning on a magnetic field to a finite value ($0 \rightarrow \Omega$).

The study of the second quench differs fundamentally from the first as the system starts its evolution in the ferromagnetic phase and, depending on the value taken by the final field the system can be driven out of the ferromagnetic phase, resulting in a paradigmatic example of a dynamical phase transition, as shown by Blaß and Rieger [16]

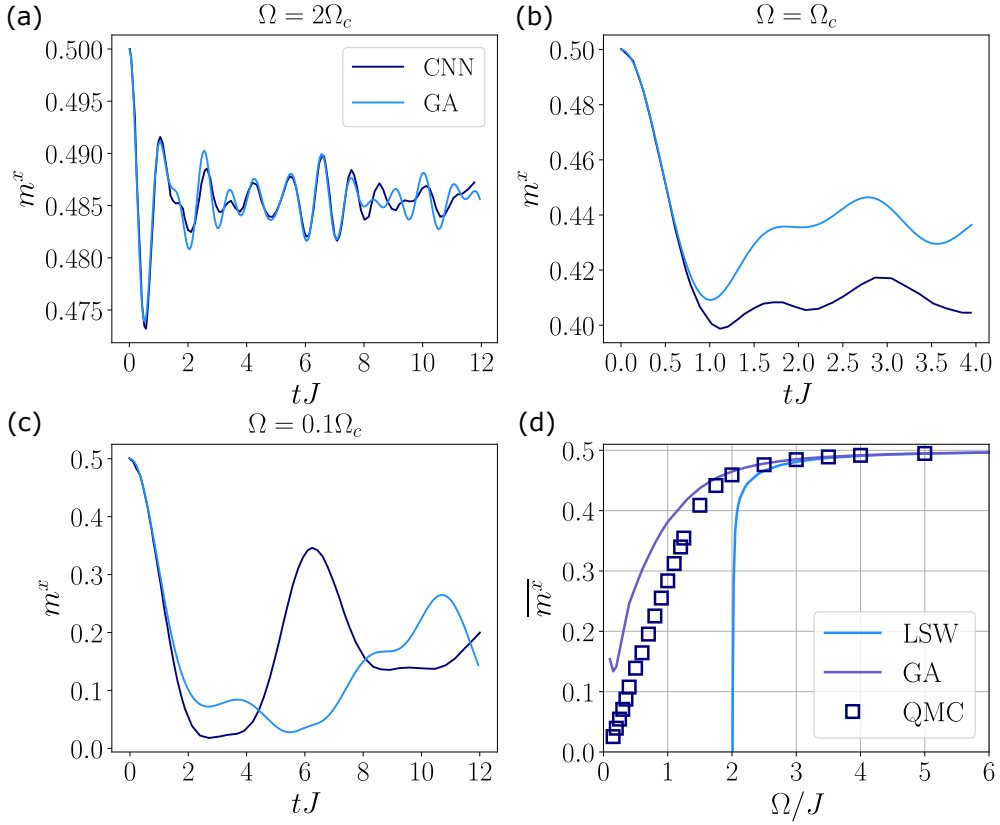


Figure 5.6: Transverse magnetization of the square lattice of size $N = 8 \times 8$ - As a function of time, the transverse magnetization, both for the Gaussian Ansatz and the CNN Ansatz, is represented for (a) $\Omega = 2\Omega_c$, (b) $\Omega = \Omega_c$ and (c) $\Omega = 0.1\Omega_c$. (d) compares the magnetization averaged over a time window of width $20J$ with linear spin-wave theory and quantum Monte Carlo results (QMC).

5.3.2 Quenching from the field-polarized state

We will start our discussion by studying quenches in which the system is initialized from the x -polarized state. As for the Ising chain, our purpose here is twofold: we aim at reproducing the non-equilibrium dynamics of the system, as well as describing its post-quench thermalization. To this end, we will compare the calculations led with the Gaussian Ansatz with results obtained by other means, namely quantum Monte Carlo simulations for the thermalization [16] and a accurate time-dependent variational study based on a neural network Ansatz (the convolutional neural network, thereafter referred to as CNN) reported in Ref. [49]

The evolution of the transverse magnetization is represented on Fig. 5.6 for three different values of the transverse field, all computed for a square lattice of size $N = 8 \times 8$ with periodic boundary conditions. The evolution of m^x for a transverse field $\Omega = 2\Omega_c$, with $\Omega_c/JS = 1.52219(1)$, is shown on Fig.5.6 (a) and exhibits a good agreement between the Gaussian Ansatz and the neural network Ansatz (which was itself successfully compared to iPEPS calculations). The near overlap of the two curves indicates that the Gaussian approach is able

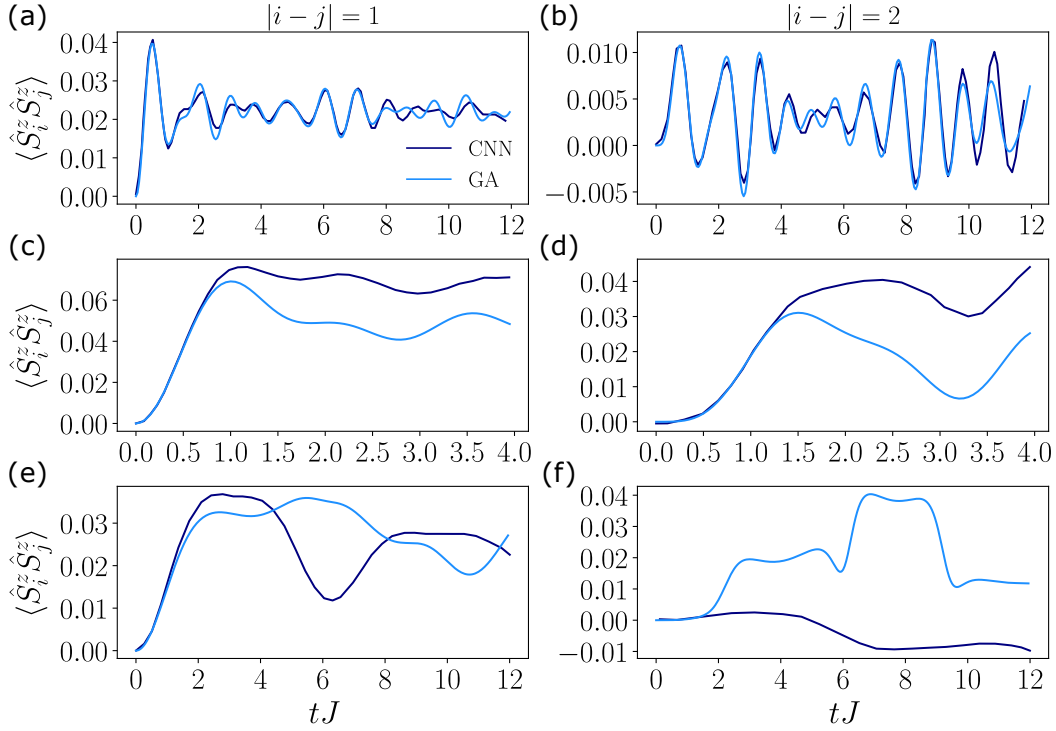


Figure 5.7: Spin-spin correlation functions along the z -axis as functions of time and position computed for a square system of size $N = 8 \times 8$ - The first column (a),(c) and (e) represents the correlation function at distance $|i - j| = 1$, while the second column (b), (d) and (f) shows them at distance $|i - j| = 2$. On the other hand, the first row (a) and (b) is at transverse field $\Omega = 2\Omega_c$, the second (c) and (d) accounts for $\Omega = \omega_c$ and the third row (e) and (f) are computed for $\Omega = 0.1\Omega_c$.

to describe faithfully the post-quench evolution of the system in terms of the spectral content of the oscillations as well as their amplitudes. A good agreement is also exhibited by the data at $\Omega = \Omega_c$ as shown on Fig 5.6 (b), where one can observe oscillations of matching frequencies in the curves associated and long-time asymptotes with the two Ansätze, despite a disagreement in their amplitudes. The Gaussian Ansatz remains coherent with the neural network results, even for quenches as strong as the one shown on Fig. 5.6 (c) for $\Omega = 0.1\Omega_c$: indeed the magnetization is expected to experience a revival, which the Gaussian succeeds in reproducing albeit at a later time.

The agreement between the Gaussian Ansatz and the actual physical behaviour of the system is further confirmed by the time-averaged magnetization represented as a function of the transverse field on Fig. 5.6 (d) and compared with thermal equilibrium values (obtained via quantum Monte-Carlo) at an inverse temperature β such that $\langle \Psi_0 | \hat{\mathcal{H}} | \Psi_0 \rangle = \text{Tr}[e^{-\beta\mathcal{H}}\mathcal{H}]/\text{Tr}[e^{-\beta\mathcal{H}}]$. Such a temperature has been systematically mapped out by [16]. As the transverse field decreases, the Gaussian Ansatz predicts a progressive depolarization of the system, though at a slower rate than what shown by the thermal equilibrium values. The overall agreement between the Gaussian approach and the thermal equilibrium results

survives down to very low fields, where the Gaussian Ansatz fails to describe the full depolarization of the system, as a result of the high densities of quasiparticles generated by the quench.

To complete the picture of the dynamics given by the Gaussian Ansatz, we investigate the evolution of the off-diagonal terms of the covariance matrix encoded in the correlation function. Following the results of Ref. [49], we explore the evolution of the spin-spin correlations along the z spin components, $\langle \hat{S}_i^z \hat{S}_j^z \rangle$, which is expressed in terms of the b -bosonic operators as

$$\hat{S}_i^z \hat{S}_j^z \simeq \frac{S}{2} \left[\left(\hat{b}_i + \hat{b}_i^\dagger - \frac{1}{4S} \left(\hat{b}_i^\dagger \hat{b}_i \hat{b}_i + \hat{b}_i^\dagger \hat{b}_i^\dagger \hat{b}_i \right) \right) \left(\hat{b}_j + \hat{b}_j^\dagger - \frac{1}{4S} \left(\hat{b}_j^\dagger \hat{b}_j \hat{b}_j + \hat{b}_j^\dagger \hat{b}_j^\dagger \hat{b}_j \right) \right) \right], \quad (5.14)$$

and compare them with the results provided by the neural network Ansatz. This comparison is made on Fig. 5.7 and confirms the observation made on the behaviour of transverse magnetization: namely that the Gaussian Ansatz captures accurately the evolution of the covariance matrix for quenches at strong field (Fig. 5.7 (a)-(b)) and maintains this accuracy up to $\Omega \lesssim \Omega_c$ (Fig. 5.7 (c)-(d)). As shown in particular on Fig. 5.7 (e)-(f), for quenches at lower fields the correlations at $|i-j|=1$ show an overall agreement between the results of the Gaussian Ansatz and those of the CNN Ansatz, while the correlations at $|i-j|=2$ differ substantially for the smallest field $\Omega = 0.1\Omega_c$, but in this regime the accuracy of the CNN Ansatz is not fully controlled.

5.3.3 Quenching from the ferromagnetic state

In the following, we will focus our attention on quenches where the system is initially prepared in the ferromagnetic phase. Though the Hamiltonian is the same as the one previously encountered, it is more natural in that case to choose a different quantization axis, aligned with the direction set by the Ising couplings, namely

$$\hat{\mathcal{H}} = -\frac{1}{2} \sum_{i,j} J_{ij} \hat{S}_i^z \hat{S}_j^z - \Omega \sum_i \hat{S}_i^x. \quad (5.15)$$

The Holstein-Primakoff transformation applied to this choice of axes leads to a spin-wave Hamiltonian which displays terms with an odd number of bosonic operators,

$$\begin{aligned} \hat{\mathcal{H}} = & -\frac{1}{2} \sum_{i,j} J_{ij} S^2 - \Omega \sqrt{\frac{S}{2}} \sum_i (\hat{b}_i + \hat{b}_i^\dagger) + \frac{S}{2} \sum_{i,j} J_{ij} (\hat{b}_i^\dagger \hat{b}_i + \hat{b}_j^\dagger \hat{b}_j) \\ & + \frac{\Omega}{4S} \sqrt{\frac{S}{2}} \sum_i (\hat{b}_i^\dagger \hat{b}_i^\dagger \hat{b}_i + \hat{b}_i^\dagger \hat{b}_i \hat{b}_i) - \frac{1}{2} \sum_{i,j} J_{ij} \hat{b}_i^\dagger \hat{b}_i \hat{b}_j^\dagger \hat{b}_j + O(b^5). \end{aligned} \quad (5.16)$$

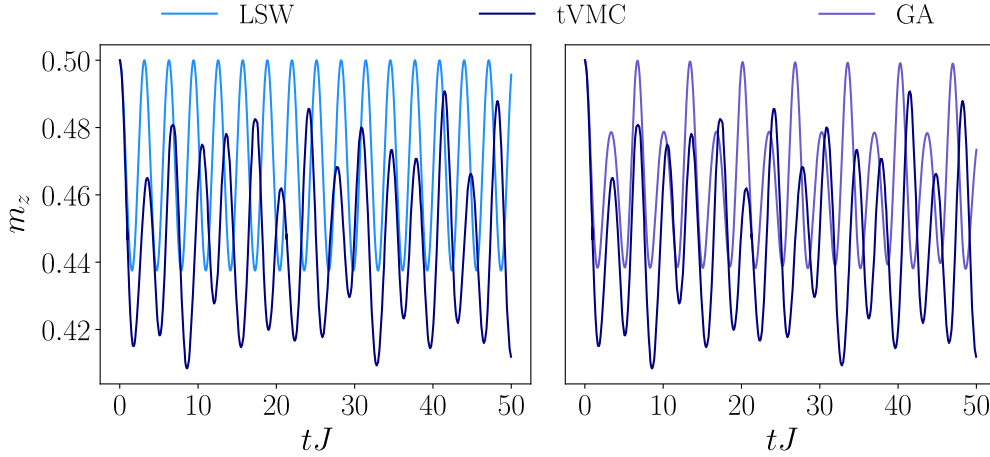


Figure 5.8: Evolution of the longitudinal magnetization for a square lattice of size $N = 6 \times 6$ initialized in the ferromagnetic state. Calculations are performed at $\Omega = J/2$. The left panel compares the LSW solution to results obtained through exact diagonalization (ED), while the right panel shows how the Gaussian Ansatz compares to the same results.

resulting in a non-vanishing bosonic mean-field $c_i = \langle \hat{b}_i \rangle$, while the covariance matrix elements $G_{ij} = \langle \hat{b}_i^\dagger \hat{b}_i \rangle - \langle \hat{b}_i^\dagger \rangle \langle \hat{b}_i \rangle$ and $F_{ij} = \langle \hat{b}_i \hat{b}_j \rangle - \langle \hat{b}_i \rangle \langle \hat{b}_j \rangle$ respectively are stationary and acquire a global rotating phase. A remarkable feature of this Hamiltonian is that at the quadratic order it does not contain any hopping or pair creation/annihilation term for the quasiparticles, the dynamics is then piloted by the mean-field c_i whose evolution is dictated by a Gross-Pitaevskii equation. As one can see in the full equations of motion given in Appendix D, taking into account terms of higher order in the Hamiltonian gives rise to effective mean-field assisted hopping and pairing terms, with the distinctive feature that fluctuations described by the covariance matrix feed back on the mean field dynamics.

This new framework, both for linear spin-wave and Gaussian approaches, is benchmarked by comparing the dynamics of the longitudinal magnetization

$$m^z = S - \frac{1}{N} \sum_i \langle \hat{b}_i^\dagger \hat{b}_i \rangle = S - \frac{1}{N} \sum_i (G_{ii} + |c_i|^2) \quad (5.17)$$

with exact diagonalization results from Ref. [16]. The result of these calculations is represented on Fig. 5.8 for a square system driven out of equilibrium by a transverse field of value $\Omega = J/2$. A first observation is that linear spin-wave theory describes single sinusoidal oscillations of the longitudinal magnetization which lack the more complex frequency structure of the exact results, and that overestimates as well the expected time-averaged magnetization. The corrections brought to linear spin-wave theory by the Gaussian Ansatz, however, lead to predictions closer to the actual spin dynamics, in that the fluctuations acquire a richer frequency spectrum.

In that regard, the Gaussian Ansatz shows a clear improvement compared to linear spin-wave theory. In order to further ascertain the quality of its predictions,

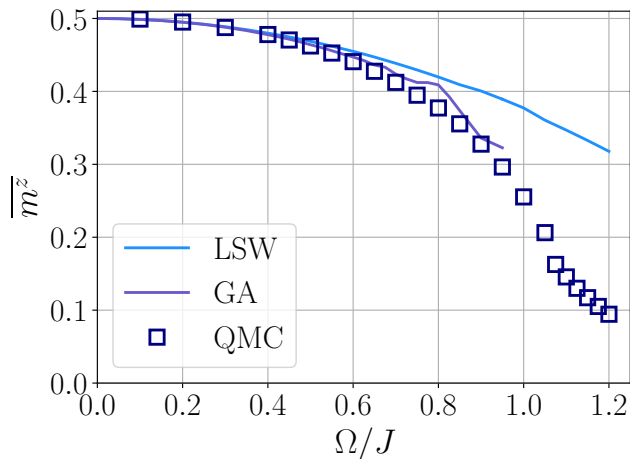


Figure 5.9: Time-average longitudinal magnetization as a function of the transverse field, computed for a square lattice of size $N = 6 \times 6$, computed for the linear spin-wave theory and the Gaussian approach and compared with quantum Monte Carlo simulations.

we shall compare the time-averaged value of the longitudinal magnetization $\overline{m^z}$ obtained via linear spin-wave theory and Gaussian Ansatz calculations with the thermal equilibrium states computed with Monte-Carlo simulations. The different results provided by these methods are summarized in Fig. 5.9, where one can see that the Gaussian Ansatz results are in good agreement with the ones provided by quantum Monte Carlo simulations up to fields $\Omega/J \sim 0.9$, namely past the critical value of $\Omega/J \sim 0.8$ at which the system is expected to exhibit a dynamical phase transition from ferromagnetism to paramagnetism in its asymptotic state [16]. Even though numerical instabilities prevent us from pushing the Gaussian Ansatz to larger quenches, these results suggest the possibility of investigating the dynamical phase transition by considering larger system sizes.

Conclusions and outlooks

*”Ainsi, sans arrêt ni faux pas, sans licol et sans étable,
sans mérites ni peines, tu parviendras, non point,
ami, au marais des joies immortelles,
Mais aux remous pleins d’ivresses du grand fleuve
Diversité.”*

Victor Segalen, ”Conseils au bon voyageur”, *Stèles*

Linear and non-linear Gaussian approaches to spin dynamics

Exotic dynamics in linearized quantum spin-models

In this thesis, we presented results regarding the equilibrium physics and dynamics of several many-body spin systems, relevant for quantum simulators that use the internal states of individually trapped atoms to mimic the behaviour of quantum spins. Using a simple bosonic Gaussian-state framework (linear spin-waves theory) explicated in Chapter 2 for the spin models of interest, we developed a set of tools aimed at revealing the spectrum of elementary excitations and the spatial structure of their associated eigenmodes.

The first case we treated in Chapter 3 was inspired by the ongoing experimental efforts to reproduce flat-band systems using the variety of different platforms, from photonic crystals to nanostructured electronic states; and by the geometrical tunability of arrays of atoms individually trapped with optical tweezers. Considering two mechanisms that can lead to band flatness - either an energy offset between two sublattices (as in the frustrated triangular lattice) or Aharonov-Bohm caging (as in the Lieb and kagome lattices) - we showed how the flat bands and their vanishing group velocities manifest in the post-quench dynamics of a quantum Ising model; and that, depending on the applied quench protocol, we could highlight overall interesting traits through the study of the dynamics. In particular, we proposed a diagnosis method (quench spectroscopy) that can provide an overall picture of the elementary excitation spectrum and of the spatial

structure over the unit cell of the magnetic lattice associated with each band. We illustrated this method in the case of the frustrated triangular lattice and evidenced the presence of a flat band in the spectrum of excitations. The second method we explored consists of locally applying a spin-flip and monitoring its evolution. If a fraction of the excitation propagates, the remaining fraction can remain trapped inside a localized state. We used this technique to highlight the Aharonov-Bohm caging effect in systems with perfectly flat bands, and we also showed that the existence of these localized modes was robust against the presence of van der Waals interactions. As a consequence, Aharonov-Bohm caging is a realistically observable phenomenon in the context of Rydberg-atom simulators.

The focus of Chapter 4 was set on another model inspired by the physics and flexibility of Rydberg-atom simulators. We considered a deformed square array of atoms where disorder is introduced in a controlled manner by displacing the optical tweezers, and we investigated how the introduction of disorder affects the long-range order of the ground state and the extended nature of the eigenstates. We found out that, due to the algebraic decay of the van der Waals interactions and how disorder is implemented into the model, the ferromagnetic long-range order of the system is preserved (and even strengthened) by the addition of disorder. On the other hand the excitation modes in the spectrum, which is decoupled from the ground state, experiences several regimes ranging from extended, to partially and then to fully localized. Furthermore, a scaling analysis of the eigenmodes reveals that in the mixed regime, where extended and localized eigenmodes coexist, the extended eigenmodes exhibit multifractal properties which result in anomalous propagation of the excitations. Effects of the anomalous diffusion can be captured in the algebraic growth of entanglement entropy and in the sub-ballistic diffusion of correlations. The multifractal nature of the eigenmodes can also be directly probed by performing a local quench on the system, as the local excess of magnetization develops at long times a profile with multifractal scaling properties.

Spin dynamics beyond linearization

Having explored the possibilities offered by a linearized theory of spin-wave systems for the study of exotic spin dynamics, we proposed in Chapter 5 a strategy to extend this framework to account for non-linearities by means of a Gaussian representation of quantum many-body states, consequently reducing the description of the whole system to two-point correlators. We have validated this approach in the case of the quantum Ising chain, admitting an exact solution in terms of fermionic excitations: the Gaussian Ansatz was able to accurately reproduce fine aspects of the dynamics, such as the spreading of correlations and the evolution of the average spin. Furthermore, the time-averaged quantities described by the Gaussian Ansatz bear striking similarities with those of the prethermalized states described by the integrable fermionic problem. Therefore, we conclude that the Gaussian Ansatz is a suitable tool to explore regimes of the dynamics of quantum spin systems, in which linear spin-wave theory breaks down.

We then applied the Gaussian Ansatz to a non-integrable model, with the two-fold goal of exploring its dynamical properties and its thermalization. We explored the dynamics of the transverse-field Ising model on the square lattice and compared the obtained results with quantum Monte Carlo simulations for the thermalized state, and with other numerical methods (exact diagonalization and variational approaches) for the non-equilibrium dynamics. The quality of the agreement between the Gaussian Ansatz and the other methods encourage us to try to apply this framework in the future to the study of other types of systems, either bosonic or fermionic, as we shall discuss in the following.

Gaussian state approaches to challenging problems of quantum dynamics

The accuracy showed by the Gaussian Ansatz approach in its description of the dynamics and relaxation of one- and two-dimensional interacting systems opens the perspective of further applying it to other challenging dynamical problems, where strong quenches or interactions play a pivotal role. Two examples of current interest, and generically tackled with exact diagonalization, are quantum dynamical phase transitions and discrete time crystals. The former are characterized by singularities in the evolution of the Loschmidt echo, defined as [48]

$$\lambda(t) = \lim_{N \rightarrow \infty} \frac{2}{N} \ln |\langle \Psi_0 | \Psi(t) \rangle|, \quad (6.1)$$

where $|\Psi_0\rangle$ is the initial state of a many-body state of N elements. A Gaussian description of the quantum-spin states offers the precious advantage of providing a general expression in terms of the covariance matrix of Gaussian states for the overlap between two states ($|\langle \Psi_0 | \Psi(t) \rangle|^2$) [10, 90]. The second example we mentioned is a dynamical regime born from the combination of several effects generically difficult to treat, namely interactions, disorder and a periodic driving. The interplay of these elements can lead to the spontaneous breaking of the discrete time-translational symmetry imposed by the driving and establish a new one instead [77]. As the Gaussian Ansatz provides a framework where the effects of interactions, disorder and a periodic driving can be readily implemented, one can hope to be able to observe the emergence of these effects in the dynamics.

Further applications of the Gaussian Ansatz can be found in addressing the questions left open in our study of flat-band systems and positionally disordered spin arrays. Indeed, as we stated several times, linear spin-wave theory provides an approximate image of spin systems in terms of integrable models, and therefore it is unable to describe properly thermalized states. The presence of non-linearities questions the stability of the effects we witnessed in flat-band systems, as non-linearities can induce in-band and inter-band scattering, and consequently they give a finite lifetime to localized excitations. In that case, are the flat-band effects robust against the introduction of non-linearities, and namely how stable is the quasiparticle population in a flat-band? Exploring these possibilities raises exciting questions regarding the relaxation and thermalization of a gas of interacting quasiparticles in a flat band.

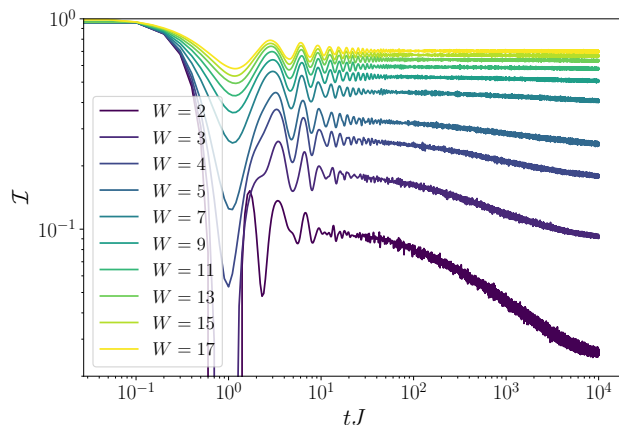


Figure 6.1: Spin imbalance as a function of time computed on a chain of $L = 48$ sites at values of disorder W ranging from $W = 2 - 17$.

The Gaussian Ansatz approach could also be applied to studying the so-called *many-body localization* (MBL). This physical phenomenon occurs in systems of strongly interacting particles in the presence of disorder, which would generically undergo Anderson localization in the absence of interactions [1]. While for weakly disordered systems interactions restore the extended and ergodic nature of the dynamics, strong disorder may instead lead to a transition toward localization. However, contrarily to an Anderson localized state, where disorder suppresses both the transport of matter and information, in many-body localized states only the transport of matter is blocked. Through an effect of residual interaction between localized degrees of freedom, entanglement entropy keeps increasing, though at a logarithmic pace [87]. Numerical investigations of many-body localization are usually led by using exact diagonalization algorithms with limitations on the size and dimensionality of the considered systems. The Gaussian Ansatz, albeit being approximate, offers the possibility of bypassing these difficulties and to explore the physics of large disordered interacting many-body systems. This possibility has been partially explored with a fermionic Gaussian approach of the canonical model used for the study of MBL, namely the one-dimensional XXZ spin model in a random longitudinal magnetic field [101], which after a Jordan-Wigner transformation can be mapped onto the following Hamiltonian for spinless fermions

$$\hat{\mathcal{H}} = \sum_i \left[-J(\hat{f}_i^\dagger \hat{f}_{i+1} + \hat{f}_{i+1}^\dagger \hat{f}_i) + 2U\hat{n}_i\hat{n}_{i+1} + h_i\hat{n}_i \right], \quad (6.2)$$

where h_i are random numbers chosen into the interval $[-W, W]$, and W quantifies the strength of disorder. Initializing the system in a state with staggered density $|\Psi_0\rangle = |010101\dots\rangle$, corresponding to a Néel state along the z -axis, the transition between the extended and localized regimes can be monitored via the relaxation in the population imbalance

$$\mathcal{I}(t) = \frac{1}{N} \sum_i (-1)^i \hat{n}_i. \quad (6.3)$$

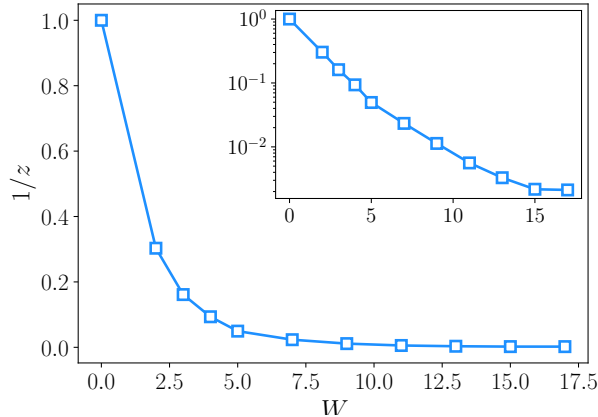


Figure 6.2: Dynamical exponent z as a function of the disorder parameter W , extracted from the evolution of spin imbalance.

The evolution of the imbalance computed with a fermionic Gaussian ansatz for several values of the disorder is represented in Fig. 6.1, and it shows an algebraic decay of imbalance $\mathcal{I}(t) \sim t^{1/z}$ for weakly disordered systems. We also observe that as disorder increasingly strengthens, the exponent z increases until the algebraic decay vanishes and imbalance relaxes toward a plateau at a size-independent finite value, therefore indicating that the system entered the many-body localized regime. This behaviour of the exponent z , extracted from the data represented in Fig. 6.1 is shown in Fig. 6.2. Suggesting the appearance of the MBL transition in the Gaussian Ansatz approach.

Describing the whole system only in terms of the two-point correlators also has the advantage of providing a straightforward access to correlations and entanglement entropy, and therefore offers a complementary point of view on the dynamical phase transition from extended to many-body localized dynamics beyond that offered by the imbalance. Such a study could then give access to a Gaussian image of this transition and its critical behaviour, and possibly give some insights on the controversial question about the existence of the MBL transitions in dimensions $D = 2$ and higher [99]. Such a study would also be relevant in the context of positionally disordered Rydberg atoms arrays, as a possible template for many-body localization in state-of-the-art quantum simulators.

Bibliography

- [1] Dmitry A. Abanin, Ehud Altman, Immanuel Bloch, and Maksym Serbyn. Colloquium: Many-body localization, thermalization, and entanglement. *Rev. Mod. Phys.*, 91:021001, May 2019.
- [2] Fabien Alet and Nicolas Laflorencie. Many-body localization: An introduction and selected topics. *Comptes Rendus Physique*, 19(6):498 – 525, 2018. Quantum simulation / Simulation quantique.
- [3] Alexander Altland and Ben D. Simons. *Condensed Matter Field Theory*. Cambridge University Press, 2006.
- [4] Juan Pablo Álvarez Zúñiga and Nicolas Laflorencie. Bose-glass transition and spin-wave localization for 2d bosons in a random potential. *Phys. Rev. Lett.*, 111:160403, Oct 2013.
- [5] M. H. Anderson, J. R. Ensher, M. R. Matthews, C. E. Wieman, and E. A. Cornell. Observation of Bose-Einstein Condensation in a Dilute Atomic Vapor. *Science*, 269(5221):198–201, July 1995. Publisher: American Association for the Advancement of Science Section: Reports.
- [6] P. W. Anderson. Absence of diffusion in certain random lattices. *Phys. Rev.*, 109:1492–1505, Mar 1958.
- [7] Alain Aspect, Philippe Grangier, and Gérard Roger. Experimental Tests of Realistic Local Theories via Bell’s Theorem. *Phys. Rev. Lett.*, 47(7):460–463, August 1981. Publisher: American Physical Society.
- [8] Assa Auerbach. *Interacting Electrons and Quantum Magnetism*. Springer-Verlag New York, 1994.
- [9] F. Baboux, L. Ge, T. Jacqmin, M. Biondi, E. Galopin, A. Lemaître, L. Le Gratiet, I. Sagnes, S. Schmidt, H. E. Türeci, A. Amo, and J. Bloch. Bosonic condensation and disorder-induced localization in a flat band. *Phys. Rev. Lett.*, 116:066402, Feb 2016.
- [10] Leonardo Banchi, Samuel L. Braunstein, and Stefano Pirandola. Quantum fidelity for arbitrary gaussian states. *Phys. Rev. Lett.*, 115:260501, Dec 2015.

- [11] Daniel Barredo, Vincent Lienhard, Sylvain de Léséleuc, Thierry Lahaye, and Antoine Browaeys. Synthetic three-dimensional atomic structures assembled atom by atom. *Nature*, 561(7721):79–82, September 2018. Number: 7721 Publisher: Nature Publishing Group.
- [12] Daniel Barredo, Sylvain de Léséleuc, Vincent Lienhard, Thierry Lahaye, and Antoine Browaeys. An atom-by-atom assembler of defect-free arbitrary two-dimensional atomic arrays. *Science*, 354(6315):1021–1023, November 2016. Publisher: American Association for the Advancement of Science Section: Report.
- [13] Federico Becca and Sandro Sorella. *Quantum Monte Carlo Approaches for Correlated Systems*. Cambridge University Press, 2017.
- [14] Hannes Bernien, Sylvain Schwartz, Alexander Keesling, Harry Levine, Ahmed Omran, Hannes Pichler, Soonwon Choi, Alexander S. Zibrov, Manuel Endres, Markus Greiner, Vladan Vuletić, and Mikhail D. Lukin. Probing many-body dynamics on a 51-atom quantum simulator. *Nature*, 551(7682):579–584, November 2017. Number: 7682 Publisher: Nature Publishing Group.
- [15] Jean-Paul Blaizot and Georges Ripka. *Quantum Theory of Finite Systems*. MIT Press, 1986.
- [16] B. Blaß and H. Rieger. Test of quantum thermalization in the two-dimensional transverse-field ising model. *Sci. Rep.*, 6:38185, 2016.
- [17] Immanuel Bloch, Jean Dalibard, and Wilhelm Zwerger. Many-body physics with ultracold gases. *Rev. Mod. Phys.*, 80:885–964, Jul 2008.
- [18] Thomas Botzung, Davide Vodola, Piero Naldesi, Markus Müller, Elisa Ercolessi, and Guido Pupillo. Algebraic localization from power-law couplings in disordered quantum wires. *Phys. Rev. B*, 100:155136, Oct 2019.
- [19] S. Bravyi, M. B. Hastings, and F. Verstraete. Lieb-robinson bounds and the generation of correlations and topological quantum order. *Phys. Rev. Lett.*, 97:050401, Jul 2006.
- [20] Antoine Browaeys and Thierry Lahaye. Many-body physics with individually controlled Rydberg atoms. *Nat. Phys.*, 16(2):132–142, February 2020. Number: 2 Publisher: Nature Publishing Group.
- [21] Pasquale Calabrese and John Cardy. Entanglement entropy and conformal field theory. *Journal of Physics A: Mathematical and Theoretical*, 42(50):504005, dec 2009.
- [22] Giuseppe Carleo and Matthias Troyer. Solving the quantum many-body problem with artificial neural networks. *Science*, 355(6325):602–606, February 2017. Publisher: American Association for the Advancement of Science Section: Research Articles.

-
- [23] A. Chandran and C. R. Laumann. Localization and symmetry breaking in the quantum quasiperiodic ising glass. *Phys. Rev. X*, 7:031061, Sep 2017.
- [24] Hitesh J. Changlani, Jesse M. Kinder, C. J. Umrigar, and Garnet Kin-Lic Chan. Approximating strongly correlated wave functions with correlator product states. *Phys. Rev. B*, 80:245116, Dec 2009.
- [25] Marc Cheneau, Peter Barmettler, Dario Poletti, Manuel Endres, Peter Schauß, Takeshi Fukuhara, Christian Gross, Immanuel Bloch, Corinna Kollath, and Stefan Kuhr. Light-cone-like spreading of correlations in a quantum many-body system. *Nature*, 481(7382):484–487, January 2012. Number: 7382 Publisher: Nature Publishing Group.
- [26] P. J. D. Crowley, A. Chandran, and C. R. Laumann. Quasiperiodic quantum ising transitions in 1d. *Phys. Rev. Lett.*, 120:175702, Apr 2018.
- [27] Luca D’Alessio, Yariv Kafri, Anatoli Polkovnikov, and Marcos Rigol. From quantum chaos and eigenstate thermalization to statistical mechanics and thermodynamics. *Advances in Physics*, 65(3):239–362, 2016.
- [28] K. B. Davis, M. O. Mewes, M. R. Andrews, N. J. van Druten, D. S. Durfee, D. M. Kurn, and W. Ketterle. Bose-einstein condensation in a gas of sodium atoms. *Phys. Rev. Lett.*, 75:3969–3973, Nov 1995.
- [29] V. Dobrosavljevic, N. Trivedi, and J. M. Jr Valles. *Conductor Insulator Quantum Phase Transitions*. Oxford University Press, 2012.
- [30] Robert Drost, Teemu Ojanen, Ari Harju, and Peter Liljeroth. Topological states in engineered atomic lattices. *Nature Phys*, 13(7):668–671, July 2017. Number: 7 Publisher: Nature Publishing Group.
- [31] L.-M. Duan, E. Demler, and M. D. Lukin. Controlling spin exchange interactions of ultracold atoms in optical lattices. *Phys. Rev. Lett.*, 91:090402, Aug 2003.
- [32] A. Einstein, B. Podolsky, and N. Rosen. Can Quantum-Mechanical Description of Physical Reality Be Considered Complete? *Phys. Rev.*, 47(10):777–780, May 1935. Publisher: American Physical Society.
- [33] Ferdinand Evers and Alexander D. Mirlin. Anderson transitions. *Rev. Mod. Phys.*, 80:1355–1417, Oct 2008.
- [34] A.L. Fetter and J. D. Walecka. *Quantum Theory of Many-particle Systems*. McGraw-Hill Professional, 1971.
- [35] Alexander L Fetter. Nonuniform states of an imperfect bose gas. *Annals of Physics*, 70(1):67 – 101, 1972.
- [36] R.P. Feynman. Simulating physics with computers. *Int. J. Theor. Phys.*, 21:467–488, 1982.

- [37] Matthew P. A. Fisher, Peter B. Weichman, G. Grinstein, and Daniel S. Fisher. Boson localization and the superfluid-insulator transition. *Phys. Rev. B*, 40:546–570, Jul 1989.
- [38] Irénée Frérot, Piero Naldesi, and Tommaso Roscilde. Multispeed Prethermalization in Quantum Spin Models with Power-Law Decaying Interactions. *Phys. Rev. Lett.*, 120(5):050401, January 2018. Publisher: American Physical Society.
- [39] Irénée Frérot and Tommaso Roscilde. Area law and its violation: A microscopic inspection into the structure of entanglement and fluctuations. *Phys. Rev. B*, 92(11):115129, September 2015. Publisher: American Physical Society.
- [40] I. M. Georgescu, S. Ashhab, and Franco Nori. Quantum simulation. *Rev. Mod. Phys.*, 86:153–185, Mar 2014.
- [41] Thierry Giamarchi. *Quantum Physics in One Dimension*. Oxford University Press, 2004.
- [42] Roy J. Glauber. Coherent and Incoherent States of the Radiation Field. *Phys. Rev.*, 131(6):2766–2788, September 1963. Publisher: American Physical Society.
- [43] Markus Greiner, Olaf Mandel, Tilman Esslinger, Theodor W. Hänsch, and Immanuel Bloch. Quantum phase transition from a superfluid to a Mott insulator in a gas of ultracold atoms. *Nature*, 415(6867):39–44, January 2002. Number: 6867 Publisher: Nature Publishing Group.
- [44] Allan Griffin, Tetsuro Nikuni, and Eugene Zaremba. *Bose-Condensed Gases at Finite Temperatures*. Cambridge University Press, 2009.
- [45] Elmer Guardado-Sanchez, Peter T. Brown, Debayan Mitra, Trithep Devakul, David A. Huse, Peter Schauf, and Waseem S. Bakr. Probing the quench dynamics of antiferromagnetic correlations in a 2d quantum ising spin system. *Phys. Rev. X*, 8:021069, Jun 2018.
- [46] Philipp Hauke, Tommaso Roscilde, Valentin Murg, J. Ignacio Cirac, and Roman Schmied. Modified spin-wave theory with ordering vector optimization: frustrated bosons on the spatially anisotropic triangular lattice. *New J. Phys.*, 12(5):053036, May 2010. Publisher: IOP Publishing.
- [47] Louis-Paul Henry, Peter C. W. Holdsworth, Frédéric Mila, and Tommaso Roscilde. Spin-wave analysis of the transverse-field Ising model on the checkerboard lattice. *Phys. Rev. B*, 85(13):134427, April 2012. Publisher: American Physical Society.
- [48] Markus Heyl. Dynamical quantum phase transitions: a review. *Reports on Progress in Physics*, 81(5):054001, apr 2018.

-
- [49] Markus Heyl and Markus Schmitt. Quantum many-body dynamics in two dimensions with artificial neural networks. arXiv:1912.08828, 2019.
- [50] T. Holstein and H. Primakoff. Field Dependence of the Intrinsic Domain Magnetization of a Ferromagnet. *Phys. Rev.*, 58(12):1098–1113, December 1940. Publisher: American Physical Society.
- [51] Chen-Lung Hung, Victor Gurarie, and Cheng Chin. From cosmology to cold atoms: Observation of sakharov oscillations in a quenched atomic superfluid. *Science*, 341(6151):1213–1215, 2013.
- [52] S. V. Isakov and R. Moessner. Interplay of quantum and thermal fluctuations in a frustrated magnet. *Phys. Rev. B*, 68(10):104409, September 2003. Publisher: American Physical Society.
- [53] P. Jurcevic, B. P. Lanyon, P. Hauke, C. Hempel, P. Zoller, R. Blatt, and C. F. Roos. Quasiparticle engineering and entanglement propagation in a quantum many-body system. *Nature*, 511(7508):202–205, July 2014. Number: 7508 Publisher: Nature Publishing Group.
- [54] Henning Labuhn, Daniel Barredo, Sylvain Ravets, Sylvain de Léséleuc, Tommaso Macrì, Thierry Lahaye, and Antoine Browaeys. Tunable two-dimensional arrays of single Rydberg atoms for realizing quantum Ising models. *Nature*, 534(7609):667–670, June 2016. Number: 7609 Publisher: Nature Publishing Group.
- [55] C. Lanczos. *An iteration method for the solution of the eigenvalue problem of linear differential and integral operators*. National Bureau of Standards, 1950.
- [56] Elliott Lieb, Theodore Schultz, and Daniel Mattis. Two soluble models of an antiferromagnetic chain. *Annals of Physics*, 16(3):407 – 466, 1961.
- [57] Elliott H. Lieb. Two theorems on the Hubbard model. *Phys. Rev. Lett.*, 62(10):1201–1204, March 1989. Publisher: American Physical Society.
- [58] Elliott H. Lieb and Derek W. Robinson. The Finite Group Velocity of Quantum Spin Systems. In Bruno Nachtergaele, Jan Philip Solovej, and Jakob Yngvason, editors, *Statistical Mechanics: Selecta of Elliott H. Lieb*, pages 425–431. Springer, Berlin, Heidelberg, 2004.
- [59] Vincent Lienhard, Sylvain de Léséleuc, Daniel Barredo, Thierry Lahaye, Antoine Browaeys, Michael Schuler, Louis-Paul Henry, and Andreas M. Läuchli. Observing the Space- and Time-Dependent Growth of Correlations in Dynamically Tuned Synthetic Ising Models with Antiferromagnetic Interactions. *Phys. Rev. X*, 8(2):021070, June 2018. Publisher: American Physical Society.
- [60] Sylvain de Léséleuc, Vincent Lienhard, Pascal Scholl, Daniel Barredo, Sebastian Weber, Nicolai Lang, Hans Peter Büchler, Thierry Lahaye, and

- Antoine Browaeys. Observation of a symmetry-protected topological phase of interacting bosons with Rydberg atoms. *Science*, 365(6455):775–780, August 2019. Publisher: American Association for the Advancement of Science Section: Research Article.
- [61] Matteo Marcuzzi, Ji ří Minář, Daniel Barredo, Sylvain de Léséleuc, Henning Labuhn, Thierry Lahaye, Antoine Browaeys, Emanuele Levi, and Igor Lesanovsky. Facilitation dynamics and localization phenomena in rydberg lattice gases with position disorder. *Phys. Rev. Lett.*, 118:063606, Feb 2017.
- [62] Anton Mazurenko, Christie S. Chiu, Geoffrey Ji, Maxwell F. Parsons, Márton Kanász-Nagy, Richard Schmidt, Fabian Grusdt, Eugene Demler, Daniel Greif, and Markus Greiner. A cold-atom Fermi–Hubbard antiferromagnet. *Nature*, 545(7655):462–466, May 2017. Number: 7655 Publisher: Nature Publishing Group.
- [63] Raphaël Menu and Tommaso Roscilde. Quench dynamics of quantum spin models with flat bands of excitations. *Phys. Rev. B*, 98:205145, Nov 2018.
- [64] Raphaël Menu and Tommaso Roscilde. Anomalous diffusion and localization in a positionally disordered quantum spin array. *Phys. Rev. Lett.*, 124:130604, Apr 2020.
- [65] F Mezzacapo, N Schuch, M Boninsegni, and J I Cirac. Ground-state properties of quantum many-body systems: entangled-plaquette states and variational monte carlo. *New Journal of Physics*, 11(8):083026, aug 2009.
- [66] R. Moessner and S. L. Sondhi. Ising models of quantum frustration. *Phys. Rev. B*, 63(22):224401, May 2001. Publisher: American Physical Society.
- [67] Sebabrata Mukherjee, Alexander Spracklen, Debaditya Choudhury, Nathan Goldman, Patrik Öhberg, Erika Andersson, and Robert R. Thomson. Observation of a Localized Flat-Band State in a Photonic Lieb Lattice. *Phys. Rev. Lett.*, 114(24):245504, June 2015. Publisher: American Physical Society.
- [68] Naoto Nagaosa. *Quantum Field Theory in Condensed Matter Physics*. Springer, 1999.
- [69] Tsuneyoshi Nakayama and Kousuke Yakubo. *Fractal Concepts in Condensed Matter Physics*. Springer, 2003.
- [70] Rahul Nandkishore and David A. Huse. Many-body localization and thermalization in quantum statistical mechanics. *Annual Review of Condensed Matter Physics*, 6(1):15–38, 2015.
- [71] Tomi Ohtsuki and Tohru Kawarabayashi. Anomalous diffusion at the anderson transitions. *Journal of the Physical Society of Japan*, 66(2):314–317, 1997.

- [72] Don N. Page. Average entropy of a subsystem. *Phys. Rev. Lett.*, 71(9):1291–1294, August 1993. Publisher: American Physical Society.
- [73] B. Passaro, C. Sire, and V. G. Benza. Anomalous diffusion and conductivity in octagonal tiling models. *Phys. Rev. B*, 46:13751–13755, Dec 1992.
- [74] P. Pfeuty. The one-dimensional ising model with a transverse field. *Annals of Physics*, 57(1):79 – 90, 1970.
- [75] Marcos Rigol, Vanja Dunjko, and Maxim Olshanii. Thermalization and its mechanism for generic isolated quantum systems. *Nature*, 452(7189):854–858, April 2008. Number: 7189 Publisher: Nature Publishing Group.
- [76] Marcos Rigol, Vanja Dunjko, Vladimir Yurovsky, and Maxim Olshanii. Relaxation in a completely integrable many-body quantum system: An ab initio study of the dynamics of the highly excited states of 1d lattice hard-core bosons. *Phys. Rev. Lett.*, 98:050405, Feb 2007.
- [77] Krzysztof Sacha and Jakub Zakrzewski. Time crystals: a review. *Reports on Progress in Physics*, 81(1):016401, nov 2017.
- [78] J. Schachenmayer, B. P. Lanyon, C. F. Roos, and A. J. Daley. Entanglement growth in quench dynamics with variable range interactions. *Phys. Rev. X*, 3:031015, Sep 2013.
- [79] J. Schachenmayer, A. Pikovski, and A. M. Rey. Many-body quantum spin dynamics with monte carlo trajectories on a discrete phase space. *Phys. Rev. X*, 5:011022, Feb 2015.
- [80] Peter Schauss. Quantum simulation of transverse Ising models with Rydberg atoms. *Quantum Sci. Technol.*, 3(2):023001, January 2018. Publisher: IOP Publishing.
- [81] Max Schemmer, Aisling Johnson, and Isabelle Bouchoule. Monitoring squeezed collective modes of a one-dimensional bose gas after an interaction quench using density-ripple analysis. *Phys. Rev. A*, 98:043604, Oct 2018.
- [82] Ch Schneider, Diego Porras, and Tobias Schaetz. Experimental quantum simulations of many-body physics with trapped ions. *Reports on Progress in Physics*, 75(2):024401, jan 2012.
- [83] Ulrich Schollwöck. The density-matrix renormalization group in the age of matrix product states. *Annals of Physics*, 326(1):96–192, January 2011.
- [84] E. Schrödinger. Discussion of probability relations between separated systems. *Mathematical Proceedings of the Cambridge Philosophical Society*, 31(4):555–563, 1935.
- [85] Norbert Schuch, Ignacio Cirac, and David Pérez-García. Peps as ground states: Degeneracy and topology. *Annals of Physics*, 325(10):2153 – 2192, 2010.

- [86] Patrick Sebbah, Didier Sornette, and Christian Vanneste. Anomalous diffusion in two-dimensional anderson-localization dynamics. *Phys. Rev. B*, 48:12506–12510, Nov 1993.
- [87] Maksym Serbyn, Z. Papić, and Dmitry A. Abanin. Universal slow growth of entanglement in interacting strongly disordered systems. *Phys. Rev. Lett.*, 110:260601, Jun 2013.
- [88] Bill Sutherland. Localization of electronic wave functions due to local topology. *Phys. Rev. B*, 34(8):5208–5211, October 1986. Publisher: American Physical Society.
- [89] Bill Sutherland. *Beautiful Models: 70 Years of Exactly Solved Quantum Many-body Problems*. World Scientific Publishing Company, first edition edition, 2004.
- [90] Brian G. Swingle and Yixu Wang. Recovery map for fermionic gaussian channels. *Journal of Mathematical Physics*, 60(7):072202, 2019.
- [91] Shintaro Taie, Hideki Ozawa, Tomohiro Ichinose, Takuei Nishio, Shuta Nakajima, and Yoshiro Takahashi. Coherent driving and freezing of bosonic matter wave in an optical Lieb lattice. *Science Advances*, 1(10):e1500854, November 2015. Publisher: American Association for the Advancement of Science Section: Research Article.
- [92] Minoru Takahashi. Modified spin-wave theory of a square-lattice antiferromagnet. *Phys. Rev. B*, 40(4):2494–2501, August 1989. Publisher: American Physical Society.
- [93] Hal Tasaki. From Nagaoka’s Ferromagnetism to Flat-Band Ferromagnetism and Beyond An Introduction to Ferromagnetism in the Hubbard Model. *Prog Theor Phys*, 99(4):489–548, April 1998. Publisher: Oxford Academic.
- [94] Julien Vidal, Rémy Mosseri, and Benoit Douçot. Aharonov-Bohm Cages in Two-Dimensional Structures. *Phys. Rev. Lett.*, 81(26):5888–5891, December 1998. Publisher: American Physical Society.
- [95] Louis Villa, Julien Despres, and Laurent Sanchez-Palencia. Unraveling the excitation spectrum of many-body systems from quantum quenches. *Phys. Rev. A*, 100:063632, Dec 2019.
- [96] J. Villain, R. Bidaux, J.-P. Carton, and R. Conte. Order as an effect of disorder. *J. Phys. France*, 41(11):1263–1272, November 1980. Publisher: Société Française de Physique.
- [97] Matthias Vojta. Excitation spectra of disordered dimer magnets near quantum criticality. *Phys. Rev. Lett.*, 111:097202, Aug 2013.
- [98] Thomas Vojta. Disorder in quantum many-body systems. *Annual Review of Condensed Matter Physics*, 10(1):233–252, 2019.

- [99] T.B. Wahl, A. Pal, and S.H. Simon. Signatures of the many-body localized regime in two dimensions. *Nature Phys.*, 15:164–169, 2019.
- [100] G. H. Wannier. Antiferromagnetism. The Triangular Ising Net. *Phys. Rev.*, 79(2):357–364, July 1950. Publisher: American Physical Society.
- [101] Simon A. Weidinger, Sarang Gopalakrishnan, and Michael Knap. Self-consistent hartree-fock approach to many-body localization. *Phys. Rev. B*, 98:224205, Dec 2018.
- [102] E. Wigner. On the quantum correction for thermodynamic equilibrium. *Phys. Rev.*, 40:749–759, Jun 1932.
- [103] J X Zhong and R Mosseri. Quantum dynamics in quasiperiodic systems. *Journal of Physics: Condensed Matter*, 7(44):8383–8404, oct 1995.

Linear spin-wave theory of the transverse field Ising model

We present in the following the general theoretical framework of the linear spin-wave theory for any model described by a transverse-field Ising model. Let us consider an organized ensemble of spins N on a regular lattice, each labeled by a couple of integers (l, p) denoting respectively the magnetic unit cell and the position. The general form taken by the Hamiltonian of the transverse-field Ising model is then

$$\hat{\mathcal{H}} = \frac{1}{2} \sum_{lp, l'p'} J_{pp'}^{ll'} S_{lp}^z S_{l'p'}^z - \Omega \sum_{lp} S_{lp}^x. \quad (\text{A.1})$$

Linear spin-wave theory hinges on a treatment of quantum fluctuations around the mean-field state of the Hamiltonian in terms of linear bosonic operators (following the Holstein-Primakoff transformation), or in other words the system is approximated in terms of a collection of coupled harmonic oscillators.

The first step of this strategy is to identify the mean-field state, namely finding the set of angles $\{\theta_p\}$ that minimize the mean-field energy

$$E_{\text{MF}} = \frac{S^2}{2} \sum_{lp, l'p'} J_{pp'}^{ll'} \cos \theta_p \cos \theta_{p'} - S \sum_{lp} (\Omega \sin \theta_p + H \cos \theta_p). \quad (\text{A.2})$$

The second step of the LSW approach consists in rotating the spin axes in the Hamiltonian around the y -axis so that their orientation matches the one of the mean-field state. The linearized bosonic Hamiltonian then reads,

$$\hat{\mathcal{H}} \simeq E_{\text{MF}} + \sum_{lp} h_p \hat{b}_{lp}^\dagger \hat{b}_{lp} + \frac{S}{4} \sum_{lp, l'p'} J_{pp'}^{ll'} \sin \theta_p \sin \theta_{p'} \left(\hat{b}_{lp} + \hat{b}_{lp}^\dagger \right) \left(\hat{b}_{l'p'} + \hat{b}_{l'p'}^\dagger \right), \quad (\text{A.3})$$

where the local chemical potential term is expressed as

$$h_p = S \sum_{l'p'} J_{pp'}^{ll'} \cos \theta_p \cos \theta_{p'} - \Omega \sin \theta_p - \Delta \cos \theta_p. \quad (\text{A.4})$$

Chapter A. Linear spin-wave theory of the transverse field Ising model

Under this form, the bosonic Hamiltonian can be rewritten as a quadratic form of operators, like in Eq. (2.9), where the matrix elements of $\mathcal{A}_{pp'}^{ll'}$ are written as

$$(\mathcal{A}_{pp'}^{ll'})_{ij} = (J_{pp'}^{ll'})_{ij} - h_p \delta_{ll'} \delta_{pp'} \delta_{ij}. \quad (\text{A.5})$$

Using the translational invariance of the system, one can perform a Fourier transform of the quadratic form in order to bring it into the compact form of Eq. 2.10, where $\mathcal{A}_{\mathbf{k}}$ is a $2n \times 2n$ block matrix

$$\mathcal{A}_{\mathbf{k}} = \begin{pmatrix} A_{\mathbf{k}} & B_{\mathbf{k}} \\ B_{\mathbf{k}} & A_{\mathbf{k}} \end{pmatrix}, \quad (\text{A.6})$$

with matrix elements given by

$$\begin{cases} (B_{\mathbf{k}})_{pp'} = \frac{S}{2} \sin \theta_p \sin \theta_{p'} \sum_l e^{i\mathbf{k} \cdot \mathbf{r}_l} J_{pp'}^{0l}, \\ (A_{\mathbf{k}})_{pp'} = (B_{\mathbf{k}})_{pp'} - h_p \delta_{pp'} \end{cases}. \quad (\text{A.7})$$

The application of the Bogoliubov transformation on $\mathcal{A}_{\mathbf{k}}$ as outlined in Sec. 2.1.3 then leads to the eigenfrequencies of the spectrum of elementary excitations $\omega_{\mathbf{k}}^{(r)}$ and to the eigenmodes.

Modified spin-wave theory

This appendix provides the detailed equations of the treatment of the transverse-field Ising model via modified spin-wave theory. The MSW approach starts, like the LSW one, with the mean-field approximation of the following spin model,

$$\hat{\mathcal{H}} = -\frac{1}{2} \sum_{i,j} J_{ij} \hat{S}_i^z \hat{S}_j^z - \Omega \sum_i \hat{S}_i^x. \quad (\text{B.1})$$

By treating the spins as classical ones ($S \rightarrow \infty$), one can determine the classical spin angles $\theta, \phi = 0$) which minimize the classical energy. This set of classical angles define a local rotation of spins around the y -axis,

$$\begin{cases} S_i^z = \cos \theta S_i^{z'} - \sin \theta S_i^{x'} \\ S_i^x = \cos \theta S_i^{x'} + \sin \theta S_i^{z'} \end{cases}, \quad (\text{B.2})$$

which transform the spin Hamiltonian in the following manner

$$\begin{aligned} \hat{\mathcal{H}} &= \frac{1}{2} \sum_{i,j} J_{ij} \left(\cos^2 \theta \hat{S}_i^{z'} \hat{S}_j^{z'} + \sin^2 \theta \hat{S}_i^{x'} \hat{S}_j^{x'} \right) \\ &+ \frac{1}{2} \sum_{i,j} J_{ij} \cos \theta \sin \theta \left(\hat{S}_i^{z'} \hat{S}_j^{x'} + \hat{S}_i^{x'} \hat{S}_j^{z'} \right) \\ &- \sum_i [\Omega \cos \theta \hat{S}_i^{x'} + \Omega \sin \theta \hat{S}_i^{z'}]. \end{aligned} \quad (\text{B.3})$$

Unlike the previously considered case, we will not further proceed by applying the Holstein-Primakoff spin-boson transformation, but rather use the alternative transformation proposed by Dyson and Maleev

$$\begin{aligned} \hat{S}_i^+ &= \hat{b}_i \\ \hat{S}_i^- &= \hat{b}_i^\dagger (2S - \hat{b}_i^\dagger \hat{b}_i) \\ \hat{S}_i^z &= S - \hat{b}_i^\dagger \hat{b}_i, \end{aligned} \quad (\text{B.4})$$

which, despite being non-hermitian, reproduce the $SU(2)$ spin algebra. This transformation has the advantage of giving rise to a finite number of non-linear terms (up to 6th order) in terms of the b -bosons. However we will limit ourselves to the quartic order in this study, leading to an expansion of the Hamiltonian as

$$\hat{\mathcal{H}} = E_{\text{MF}} + \hat{\mathcal{H}}^{(2)} + \hat{\mathcal{H}}^{(3)} + \hat{\mathcal{H}}^{(4)} + O(b^5), \quad (\text{B.5})$$

where the different parts of the bosonic Hamiltonian are

$$\begin{aligned} \hat{\mathcal{H}}^{(2)} = & -\frac{1}{2} \sum_{i,j} J_{ij} [-2S \cos^2 \theta \hat{b}_i^\dagger \hat{b}_i + \frac{1}{4} \sin^2 \theta (2S \hat{b}_i^\dagger + \hat{b}_i)(2S \hat{b}_j^\dagger + \hat{b}_j)] \\ & + \Omega \sum_i \sin \theta \hat{b}_i^\dagger \hat{b}_i, \end{aligned} \quad (\text{B.6})$$

$$\hat{\mathcal{H}}^{(3)} = -\frac{1}{4} \sum_{i,j} J_{ij} \cos \theta \sin \theta \left[\hat{b}_i^\dagger \hat{b}_i \hat{b}_j + \hat{b}_i \hat{b}_j^\dagger \hat{b}_j + 2S(\hat{b}_i^\dagger \hat{b}_i \hat{b}_j^\dagger + \hat{b}_i^\dagger \hat{b}_j^\dagger \hat{b}_j) \right], \quad (\text{B.7})$$

and

$$\begin{aligned} \hat{\mathcal{H}}^{(4)} = & -\frac{1}{2} \sum_{i,j} J_{ij} \left[\cos^2 \theta \hat{b}_i^\dagger \hat{b}_i \hat{b}_j^\dagger \hat{b}_j - \frac{1}{4} \sin^2 \theta \left(\hat{b}_i \hat{b}_j^\dagger \hat{b}_j^\dagger \hat{b}_j + \hat{b}_i^\dagger \hat{b}_i^\dagger \hat{b}_i \hat{b}_j \right) \right. \\ & \left. + 2S \left(\hat{b}_i^\dagger \hat{b}_j^\dagger \hat{b}_j^\dagger \hat{b}_j + \hat{b}_i^\dagger \hat{b}_i^\dagger \hat{b}_i \hat{b}_j^\dagger \right) \right]. \end{aligned} \quad (\text{B.8})$$

The strategy of MSW theory consists then in minimizing the free energy $\mathcal{F} = \langle \mathcal{H} \rangle - TS$ parametrized by the set of parameters $\{\theta_{\mathbf{k}}, \omega_{\mathbf{k}}, c\}$ defined in the main text. The evaluation of the different contributions of the energy using the Gaussian nature of the state leads to non-linear expressions in terms of the Green functions G_{ij} , F_{ij} and of the mean field c :

$$\begin{aligned} E^{(2)} = & \left[S \sum_{i,j} J_{ij} \cos^2 \theta + N \Omega \sin \theta \right] \left(G(0) - \frac{1}{2} + c^2 \right) \\ & - \frac{1}{8} \sum_{ij} J_{ij} \sin^2 \theta \left[(1 + 4S^2) F_{ij} + 2S (G_{ij} + G_{ji}) + (1 + 2S)^2 c^2 \right], \end{aligned} \quad (\text{B.9})$$

where $J_{\mathbf{k}} = (1/N) \sum_j e^{i\mathbf{k} \cdot \mathbf{r}_j} J_{0j}$ is the Fourier transform of the coupling matrix. We can note that the contribution of the quadratic Hamiltonian corresponds to the results provided by the linear spin-wave theory. The contributions of the higher orders are

$$E^{(3)} = -\frac{1}{2} \sum_{i,j} J_{ij} \cos \theta \sin \theta (1 + 2S) \left[\left(\left(G(0) - \frac{1}{2} \right) + F_{ij} + \text{Re}(G_{ij}) \right) c + c^3 \right] \quad (\text{B.10})$$

for the third order contribution

$$E_I^{(4)} = -\frac{1}{2} \sum_{i,j} J_{ij} \cos^2 \theta \left[\left(G(0) - \frac{1}{2} \right)^2 + F_{ij}^2 + G_{ij} G_{ji} \right. \\ \left. + c^2 (2G(0) - 1 + 2F_{ij} + 2\text{Re}(G_{ij})) + c^4 \right] \quad (\text{B.11})$$

for the Ising interactions and

$$E_{HC}^{(4)} = \frac{1}{4} \sum_{i,j} J_{ij} \sin^2 \theta [(2G(0) - 1)(G_{ij} + 2SF_{ij}) + F(0)(F_{ij} + 2SG_{ij}) \\ + c^2 ((2 + 2S)G_{ij} + (1 + 4S)F_{ij} + (1 + 2S)(2G(0) - 1 + F(0))) \\ + c^4(1 + 2S)] \quad (\text{B.12})$$

for the terms stemming from the hardcore constraint.

The minimization of the free energy then leads to self-consistent equations for the Green functions

$$\begin{cases} G_{ij} = \frac{1}{N} \sum_{\mathbf{k}} e^{-i\mathbf{k}\cdot(\mathbf{r}_i - \mathbf{r}_j)} \frac{A_{\mathbf{k}}}{\omega_{\mathbf{k}}} \left(n_{\mathbf{k}} + \frac{1}{2} \right) \\ F_{ij} = \frac{1}{N} \sum_{\mathbf{k}} e^{-i\mathbf{k}\cdot(\mathbf{r}_i - \mathbf{r}_j)} \frac{B_{\mathbf{k}}}{\omega_{\mathbf{k}}} \left(n_{\mathbf{k}} + \frac{1}{2} \right) \end{cases}, \quad (\text{B.13})$$

where $n_{\mathbf{k}} = 1/(\exp(\beta\omega_{\mathbf{k}}) - 1)$, with the frequency $\omega_{\mathbf{k}} = \sqrt{A_{\mathbf{k}}^2 - B_{\mathbf{k}}^2}$ and the coefficients $A_{\mathbf{k}}$ and $B_{\mathbf{k}}$ are expressed as the sums of several contributions coming from the different terms of the Hamiltonian,

$$\begin{cases} A_{\mathbf{k}} = A_{\mathbf{k}}^{(2)} + A_{\mathbf{k}}^{(3)} + A_{I,\mathbf{k}}^{(4)} + A_{HC,\mathbf{k}}^{(4)} \\ B_{\mathbf{k}} = B_{\mathbf{k}}^{(2)} + B_{\mathbf{k}}^{(3)} + B_{I,\mathbf{k}}^{(4)} + B_{HC,\mathbf{k}}^{(4)} \end{cases}, \quad (\text{B.14})$$

namely

$$\begin{cases} A_{\mathbf{k}}^{(2)} = \Omega \sin \theta + S \cos^2 \theta J_{\mathbf{k}=0} - \frac{S}{2} \sin^2 \theta J_{\mathbf{k}} \\ B_{\mathbf{k}}^{(2)} = \frac{1}{8} \sin^2 \theta (1 + 4S^2) J_{\mathbf{k}} \end{cases}, \quad (\text{B.15})$$

$$\begin{cases} A_{\mathbf{k}}^{(3)} = -\frac{1}{2} \cos \theta \sin \theta (1 + 2S) c (J_{\mathbf{k}=0} + J_{\mathbf{k}}) \\ B_{\mathbf{k}}^{(3)} = \frac{1}{2} \cos \theta \sin \theta (1 + 2S) c J_{\mathbf{k}} \end{cases}, \quad (\text{B.16})$$

$$\begin{cases} A_{I,\mathbf{k}}^{(4)} = -\frac{1}{N} \sum_{i,j} J_{ij} \cos^2 \theta \left[\left(G(0) - \frac{1}{2} + c^2 \right) + \text{Re} \left(e^{i\mathbf{k}\cdot(\mathbf{r}_i - \mathbf{r}_j)} (G_{ij} + c^2) \right) \right] \\ B_{I,\mathbf{k}}^{(4)} = \frac{1}{N} \sum_{i,j} J_{ij} \cos^2 \theta \left[e^{i\mathbf{k}\cdot(\mathbf{r}_i - \mathbf{r}_j)} (F_{ij} + c^2) \right] \end{cases}, \quad (\text{B.17})$$

$$\begin{aligned}
 A_{HC,\mathbf{k}}^{(4)} = & \frac{1}{4} \sum_{i,j} J_{ij} \sin^2 \theta \left[\frac{2}{N} ((G_{ij} + c^2) + 2S(F_{ij} + c^2)) \right. \\
 & \left. + \frac{1}{N} e^{-i\mathbf{r}\cdot(\mathbf{r}_i - \mathbf{r}_j)} ((2G(0) - 1 + 2c^2) + 2S(F(0) + c^2)) \right], \tag{B.18}
 \end{aligned}$$

and finally

$$\begin{aligned}
 B_{HC,\mathbf{k}}^{(4)} = & -\frac{1}{4} \sum_{i,j} J_{ij} \sin^2 \theta \left[\frac{1}{N} ((F_{ij} + c^2) + 2S(G_{ij} + c^2)) \right. \\
 & \left. + \frac{1}{N} e^{-i\mathbf{r}\cdot(\mathbf{r}_i - \mathbf{r}_j)} (2S(2G(0) - 1 + 2c^2) + (F(0) + c^2)) \right]. \tag{B.19}
 \end{aligned}$$

As for c , it is the solution of the equation

$$\begin{aligned}
 0 = & - \sum_{i,j} J_{ij} \left[-2S \cos^2 \theta + \frac{1}{4} \sin^2 \theta (1 + 2S)^2 \right] c + 2N\Omega \sin \theta c \tag{B.20} \\
 & - \frac{1}{2} \sum_{i,j} J_{ij} \cos \theta \sin \theta (1 + 2S) \left[\left(\left(G(0) - \frac{1}{2} \right) + F_{ij} + \text{Re}(G_{ij}) \right) + 3c^2 \right] \\
 & - \sum_{i,j} J_{ij} \cos^2 \theta [2c^3 + c(G(0) - 1 + 2F_{ij} + G_{ij} + G_{ji})] \\
 & + \frac{1}{4} \sum_{i,j} J_{ij} \sin^2 \theta [2c((2 + 2S)G_{ij} + (1 + 4S)F_{ij} + (1 + 2S)(2G(0) - 1 + F(0)) + 4c^3)].
 \end{aligned}$$

Quench spectroscopy

This section is dedicated to the study of the time evolution of the momentum-dependent structure factor, providing the demonstration of Eq. (3.10) and the explicit expression of the prefactors $f_{pp'}$, $g_{pp'}^{rr'}$, $h_{pp'}^{rr'}$, $\bar{g}_{pp'}^{rr'}$ and $\bar{h}_{pp'}^{rr'}$. Following the convention taken in Eq. (3.9), the correlation function in \mathbf{k} -space is expressed as

$$\begin{aligned}
 S_{pp'}^{xx}(\mathbf{k}, t) \simeq & \sin \theta_p \sin \theta_{p'} \sum_q \left(\langle b_{-\mathbf{k}+\mathbf{q},p}^\dagger b_{-\mathbf{k}+\mathbf{q},p'} \rangle \langle b_{\mathbf{q},p} b_{\mathbf{q},p'}^\dagger \rangle \right. \\
 & + \langle b_{-\mathbf{k}+\mathbf{q},p}^\dagger b_{\mathbf{k}-\mathbf{q},p'}^\dagger \rangle \langle b_{\mathbf{q},p} b_{-\mathbf{q},p'} \rangle \Big) \\
 & + \frac{s}{2} \cos \theta_p \cos \theta_{p'} \left(\langle b_{-\mathbf{k},p}^\dagger b_{-\mathbf{k},p'} \rangle + \langle b_{\mathbf{k},p} b_{\mathbf{k},p'}^\dagger \rangle \right. \\
 & \left. + \langle b_{-\mathbf{k},p}^\dagger b_{\mathbf{k},p'}^\dagger \rangle + \langle b_{\mathbf{k},p} b_{-\mathbf{k},p'} \rangle \right). \tag{C.1}
 \end{aligned}$$

Given the diluteness of the quasi-particle gas, we can safely neglect the quartic terms, and restrict our attention to the quadratic terms only. Notice that the numerical calculation leading to Fig. 3.11 includes the quartic terms as well; the success of our analysis based uniquely on the quadratic terms confirms the weakness of the quartic terms.

The time-Fourier transform of these terms can be explicitly computed, revealing the spectral information we are searching for. Indeed, using the Bogoliubov transformation twice leads to an expression of the bosonic excitation operator $b_{\mathbf{k},p}$ in terms of oscillating functions,

$$\begin{aligned}
 b_{\mathbf{k},p}(t) = & \sum_{r,s} \left[(u_{\mathbf{k},p}^{(r)*} u_{\mathbf{k},s}^{(r)} - v_{\mathbf{k},p}^{(r)} v_{\mathbf{k},s}^{(r)*}) \cos(\omega_{\mathbf{k}}^{(r)} t) \right. \\
 & \left. - i (u_{\mathbf{k},p}^{(r)*} u_{\mathbf{k},s}^{(r)} + v_{\mathbf{k},p}^{(r)} v_{\mathbf{k},s}^{(r)*}) \sin(\omega_{\mathbf{k}}^{(r)} t) \right] b_{\mathbf{k},s}(0) \\
 & + \left[(u_{\mathbf{k},p}^{(r)*} v_{\mathbf{k},s}^{(r)} - v_{\mathbf{k},p}^{(r)} u_{\mathbf{k},s}^{(r)*}) \cos(\omega_{\mathbf{k}}^{(r)} t) \right. \\
 & \left. - i (u_{\mathbf{k},p}^{(r)*} v_{\mathbf{k},s}^{(r)} + v_{\mathbf{k},p}^{(r)} u_{\mathbf{k},s}^{(r)*}) \sin(\omega_{\mathbf{k}}^{(r)} t) \right] b_{-\mathbf{k},s}^\dagger(0). \tag{C.2}
 \end{aligned}$$

As a result, the time dependence of the structure factor is provided by a sum of oscillating functions, as summarized in Eq. (3.10), with the following prefactors:

$$\begin{aligned}
 f_{\mathbf{k},pp'} &= \frac{S}{2} \cos \theta_p \cos \theta_{p'} (\delta_{pp'} \\
 &+ \sum_r \left[2 \left(u_{\mathbf{k},p}^{(r)*} u_{\mathbf{k},p'}^{(r)} |\mathbf{v}_{\mathbf{k}}^{(r)}|^2 + v_{\mathbf{k},p}^{(r)} v_{\mathbf{k},p'}^{(r)*} |\mathbf{u}_{\mathbf{k}}^{(r)}|^2 \right) \right. \\
 &- \left(v_{\mathbf{k},p}^{(r)} u_{\mathbf{k},p'}^{(r)} ((\mathbf{u}_{\mathbf{k}}^r \cdot \mathbf{u}_{\mathbf{k}}^r) + (\mathbf{v}_{\mathbf{k}}^r \cdot \mathbf{v}_{\mathbf{k}}^r))^* \right. \\
 &\left. \left. + u_{\mathbf{k},p}^{(r)*} v_{\mathbf{k},p'}^{(r)*} ((\mathbf{u}_{\mathbf{k}}^r \cdot \mathbf{u}_{\mathbf{k}}^r) + (\mathbf{v}_{\mathbf{k}}^r \cdot \mathbf{v}_{\mathbf{k}}^r)) \right) \right], \tag{C.3}
 \end{aligned}$$

for the time-independent part of the structure factor,

$$\begin{aligned}
 g_{pp'}^{rr'}(\mathbf{k}) &= \frac{S}{2} \cos \theta_p \cos \theta_{p'} \left[-2 \left(v_{\mathbf{k},p}^{(r)} u_{\mathbf{k},p'}^{(r')} (\mathbf{u}_{\mathbf{k}}^{(r)} \cdot \mathbf{v}_{\mathbf{k}}^{(r')})^* \right) \right. \\
 &+ v_{\mathbf{k},p}^{(r')} u_{\mathbf{k},p'}^{(r)} (\mathbf{u}_{\mathbf{k}}^{(r')} \cdot \mathbf{v}_{\mathbf{k}}^{(r)})^* \\
 &+ u_{\mathbf{k},p}^{(r)*} v_{\mathbf{k},p'}^{(r')*} (\mathbf{v}_{\mathbf{k}}^{(r)} \cdot \mathbf{u}_{\mathbf{k}}^{(r')}) + u_{\mathbf{k},p}^{(r')} v_{\mathbf{k},p'}^{(r)*} (\mathbf{v}_{\mathbf{k}}^{(r')} \cdot \mathbf{u}_{\mathbf{k}}^{(r)}) \\
 &+ \left((\mathbf{u}_{\mathbf{k}}^{(r)} \cdot \mathbf{v}_{\mathbf{k}}^{(r)*} + \mathbf{v}_{\mathbf{k}}^{(r)} \cdot \mathbf{u}_{\mathbf{k}}^{(r)*}) (u_{\mathbf{k},p}^{(r)*} u_{\mathbf{k},p'}^{(r')} + v_{\mathbf{k},p}^{(r')} v_{\mathbf{k},p'}^{(r)*}) \right. \\
 &\left. \left. + (\mathbf{v}_{\mathbf{k}}^{(r)*} \cdot \mathbf{u}_{\mathbf{k}}^{(r')} + \mathbf{v}_{\mathbf{k}}^{(r')} \cdot \mathbf{u}_{\mathbf{k}}^{(r)*}) (u_{\mathbf{k},p}^{(r')} u_{\mathbf{k},p'}^{(r)} + v_{\mathbf{k},p}^{(r)} v_{\mathbf{k},p'}^{(r')}) \right) \right], \tag{C.4}
 \end{aligned}$$

and

$$\begin{aligned}
 h_{pp'}^{rr'}(\mathbf{k}) &= \frac{S}{2} \cos \theta_p \cos \theta_{p'} \left[2 \left(u_{\mathbf{k},p}^{(r)*} u_{\mathbf{k},p'}^{(r')} (\mathbf{v}_{\mathbf{k}}^{(r)} \cdot \mathbf{v}_{\mathbf{k}}^{(r')})^* \right) \right. \\
 &+ u_{\mathbf{k},p}^{(r')} u_{\mathbf{k},p'}^{(r)} (\mathbf{v}_{\mathbf{k}}^{(r')} \cdot \mathbf{v}_{\mathbf{k}}^{(r)*}) \\
 &+ v_{\mathbf{k},p}^{(r)} v_{\mathbf{k},p'}^{(r')*} (\mathbf{u}_{\mathbf{k}}^{(r)*} \cdot \mathbf{u}_{\mathbf{k}}^{(r')}) + v_{\mathbf{k},p}^{(r')} v_{\mathbf{k},p'}^{(r)*} (\mathbf{u}_{\mathbf{k}}^{(r')} \cdot \mathbf{u}_{\mathbf{k}}^{(r)}) \\
 &- \left((\mathbf{u}_{\mathbf{k}}^{(r)} \cdot \mathbf{u}_{\mathbf{k}}^{(r')} + \mathbf{v}_{\mathbf{k}}^{(r)} \cdot \mathbf{v}_{\mathbf{k}}^{(r')})^* (v_{\mathbf{k},p}^{(r)} u_{\mathbf{k},p'}^{(r')} + v_{\mathbf{k},p}^{(r')} u_{\mathbf{k},p'}^{(r)}) \right. \\
 &\left. \left. + (\mathbf{u}_{\mathbf{k}}^{(r)} \cdot \mathbf{u}_{\mathbf{k}}^{(r')} + \mathbf{v}_{\mathbf{k}}^{(r)} \cdot \mathbf{v}_{\mathbf{k}}^{(r')}) (u_{\mathbf{k},p}^{(r)} v_{\mathbf{k},p'}^{(r')} + u_{\mathbf{k},p}^{(r')} v_{\mathbf{k},p'}^{(r)})^* \right) \right], \tag{C.5}
 \end{aligned}$$

are the amplitude of the cosine parts of the structure factor, while

$$\begin{aligned}
 \bar{g}_{pp'}^{rr'}(\mathbf{k}) &= \frac{S}{2} \cos \theta_p \cos \theta_{p'} \left[2 \left(v_{\mathbf{k},p}^{(r)} u_{\mathbf{k},p'}^{(r')} (\mathbf{u}_{\mathbf{k}}^{(r)} \cdot \mathbf{v}_{\mathbf{k}}^{(r')})^* \right) \right. \\
 &- u_{\mathbf{k},p}^{(r)*} v_{\mathbf{k},p'}^{(r')*} (\mathbf{v}_{\mathbf{k}}^{(r)} \cdot \mathbf{u}_{\mathbf{k}}^{(r')}) \\
 &+ v_{\mathbf{k},p}^{(r')} u_{\mathbf{k},p'}^{(r)} (\mathbf{v}_{\mathbf{k}}^{(r')} \cdot \mathbf{u}_{\mathbf{k}}^{(r)})^* - u_{\mathbf{k},p}^{(r)*} v_{\mathbf{k},p'}^{(r')*} (\mathbf{v}_{\mathbf{k}}^{(r')} \cdot \mathbf{u}_{\mathbf{k}}^{(r)}) \\
 &- \left((\mathbf{u}_{\mathbf{k}}^{(r)} \cdot \mathbf{v}_{\mathbf{k}}^{(r')})^* (u_{\mathbf{k},p}^{(r)*} u_{\mathbf{k},p'}^{(r')} - v_{\mathbf{k},p}^{(r')} v_{\mathbf{k},p'}^{(r)*}) \right. \\
 &+ (\mathbf{u}_{\mathbf{k}}^{(r')} \cdot \mathbf{v}_{\mathbf{k}}^{(r)*}) (u_{\mathbf{k},p}^{(r')} u_{\mathbf{k},p'}^{(r)} - v_{\mathbf{k},p}^{(r)} v_{\mathbf{k},p'}^{(r')}) \\
 &+ \left((\mathbf{u}_{\mathbf{k}}^{(r)*} \cdot \mathbf{v}_{\mathbf{k}}^{(r')}) (u_{\mathbf{k},p}^{(r)*} u_{\mathbf{k},p'}^{(r)} - v_{\mathbf{k},p}^{(r)} v_{\mathbf{k},p'}^{(r')})^* \right. \\
 &\left. \left. + (\mathbf{u}_{\mathbf{k}}^{(r')} \cdot \mathbf{v}_{\mathbf{k}}^{(r)}) (u_{\mathbf{k},p}^{(r')} u_{\mathbf{k},p'}^{(r)} - v_{\mathbf{k},p}^{(r')} v_{\mathbf{k},p'}^{(r)*}) \right) \right], \tag{C.6}
 \end{aligned}$$

and

$$\begin{aligned}
\bar{h}_{pp'}^{rr'}(\mathbf{k}) = & \frac{s}{2} \cos \theta_p \cos \theta_{p'} \left[2 \left(u_{\mathbf{k},p}^{(r)*} u_{\mathbf{k},p'}^{(r')} (\mathbf{v}_{\mathbf{k}}^{(r)} \cdot \mathbf{v}_{\mathbf{k}}^{(r')*}) \right. \right. \\
& - v_{\mathbf{k},p}^{(r)} v_{\mathbf{k},p'}^{(r')*} (\mathbf{u}_{\mathbf{k}}^{(r)*} \cdot \mathbf{u}_{\mathbf{k}}^{(r')}) \\
& - u_{\mathbf{k},p}^{(r')*} u_{\mathbf{k},p'}^{(r)} (\mathbf{v}_{\mathbf{k}}^{(r')} \cdot \mathbf{v}_{\mathbf{k}}^{(r)*}) + v_{\mathbf{k},p}^{(r')} v_{\mathbf{k},p'}^{(r)*} (\mathbf{u}_{\mathbf{k}}^{(r')*} \cdot \mathbf{u}_{\mathbf{k}}^{(r)}) \left. \right) \\
& - \left((\mathbf{v}_{\mathbf{k}}^{(r)} \cdot \mathbf{v}_{\mathbf{k}}^{(r')})^* (v_{\mathbf{k},p}^{(r)} u_{\mathbf{k},p'}^{(r')} - v_{\mathbf{k},p}^{(r')} u_{\mathbf{k},p'}^{(r)}) \right. \\
& - (\mathbf{u}_{\mathbf{k}}^{(r')} \cdot \mathbf{u}_{\mathbf{k}}^{(r)}) (u_{\mathbf{k},p}^{(r)*} v_{\mathbf{k},p'}^{(r')*} - u_{\mathbf{k},p}^{(r')} v_{\mathbf{k},p'}^{(r)*}) \left. \right) \\
& + \left((\mathbf{u}_{\mathbf{k}}^{(r)} \cdot \mathbf{u}_{\mathbf{k}}^{(r')})^* (u_{\mathbf{k},p}^{(r)} v_{\mathbf{k},p'}^{(r')} - u_{\mathbf{k},p}^{(r')} v_{\mathbf{k},p'}^{(r)}) \right. \\
& \left. \left. - (\mathbf{v}_{\mathbf{k}}^{(r)} \cdot \mathbf{v}_{\mathbf{k}}^{(r')}) (v_{\mathbf{k},p}^{(r)} u_{\mathbf{k},p'}^{(r')} - v_{\mathbf{k},p}^{(r')} u_{\mathbf{k},p'}^{(r)*}) \right) \right]. \tag{C.7}
\end{aligned}$$

are the prefactors for the sine parts. We notice that the \bar{g} and \bar{h} coefficients are purely imaginary, resulting in a real expression in Eq. (3.10).

Gaussian Ansatz approach of the transverse field Ising model

This Appendix provides the expression of the equations of motion for the mean fields c_i and the two-point correlators G_{ij} and F_{ij} for two choices of the quantization axes.

D.1 Quenching from the field-polarized state

The equations of motion for the Hamiltonian given at Eq. (5.4) are the following

$$\begin{aligned}
 \frac{d}{dt}G_{ij} = & i \left(-\frac{S}{2} \sum_k J_{ik} (G_{kj} + F_{kj}) + \frac{S}{2} \sum_k J_{jk} (G_{ki} + F_{ki}) \right. & (D.1) \\
 & - \frac{1}{8} \sum_k J_{ik} [2(F_{ki}^* + G_{ki}^*)F_{ij} + (2G_{ii} + 2G_{kk} + F_{ii}^* + F_{kk}^*)F_{kj} \\
 & + 4\text{Re}(F_{ki} + G_{ki})G_{ij} + (2G_{ii} + 2G_{kk} + F_{ii}^* + F_{kk}^*)G_{kj}] \\
 & + \frac{1}{8} \sum_k J_{jk} [2(F_{kj} + G_{kj})F_{ji}^* + (2G_{jj} + 2G_{kk} + F_{jj} + F_{kk})F_{ki} \\
 & \left. + 4\text{Re}(F_{ki} + G_{ki})G_{ji}^* + (2G_{jj} + 2G_{kk} + F_{jj} + F_{kk}^*)G_{ki}^* \right]
 \end{aligned}$$

and

$$\begin{aligned}
 \frac{d}{dt}F_{ij} = & i \left(\frac{S}{2} \sum_k J_{ik} (G_{kj} + F_{kj}) + \frac{S}{2} \sum_k J_{jk} (G_{ki} + F_{ki}) - 2\Omega F_{ij} + \frac{S}{2} J_{ij} \right) & (D.2) \\
 & + \frac{1}{8} \sum_k J_{ik} [2(F_{ki} + G_{ki})G_{ij} + (2G_{ii} + 2G_{kk} + F_{ii} + F_{kk})G_{kj} \\
 & + 4\text{Re}(F_{ki} + G_{ki})F_{ij} + (2G_{ii} + 2G_{kk} + F_{ii} + F_{kk}^*)F_{kj}] \\
 & + \frac{1}{8} \sum_k J_{jk} [2(F_{kj} + G_{kj})G_{ji} + (2G_{jj} + 2G_{kk} + F_{jj} + F_{kk})G_{ki} \\
 & + 4\text{Re}(F_{kj} + G_{kj})F_{ji} + (2G_{jj} + 2G_{kk} + F_{jj} + F_{kk}^*)F_{ki}]
 \end{aligned}$$

$$+ \frac{1}{4} \sum_k J_{jk} (F_{kj} + G_{kj}) \delta_{ij} + \frac{1}{8} J_{ij} (2G_{ii} + 2G_{jj} + F_{jj} + F_{ii}) \Big)$$

D.2 Quenching from the ferromagnetic state

The equations of motion derived from Eq. (5.16) are

$$\begin{aligned} \frac{d}{dt} c_i = i \Big(& \Omega \sqrt{\frac{S}{2}} + S \sum_k J_{ik} c_i - \frac{\Omega}{4S} \sqrt{\frac{S}{2}} (2G_{ii} + F_{ii} + 2|c_i|^2 + c_i^2) \\ & + \sum_k J_{ik} [G_{kk} c_i + G_{ki} c_k + F_{ki} c_k^* + |c_k|^2 c_i] \Big), \end{aligned} \quad (\text{D.3})$$

$$\begin{aligned} \frac{d}{dt} G_{ij} = i \Big(& -S \sum_k J_{ik} G_{ij} + -S \sum_k J_{jk} G_{ji}^* \\ & + \frac{\Omega}{2S} \sqrt{\frac{S}{2}} [(c_i + c_i^*) G_{ij} + c_i^* F_{ij} - (c_j + c_j^*) G_{ji}^* + c_j F_{ji}^*] \\ & - \sum_k J_{ik} [(G_{kk} + |c_k|^2) G_{ij} + (F_{ik}^* + c_i^* c_k^*) F_{kj} + (G_{ik} + c_i^* c_k) G_{kj}] \\ & + \sum_k J_{jk} [(G_{kk} + |c_k|^2) G_{ji}^* + (F_{jk} + c_j c_k) F_{ki}^* + (G_{jk}^* + c_j c_k^*) G_{ki}^*] \Big) \end{aligned} \quad (\text{D.4})$$

and

$$\begin{aligned} \frac{d}{dt} F_{ij} = i \Big(& S \sum_k J_{ik} F_{ij} + -S \sum_k J_{jk} F_{ji} \\ & - \frac{\Omega}{2S} \sqrt{\frac{S}{2}} [(c_i + c_i^*) F_{ij} + c_i F_{ij} + (c_j + c_j^*) F_{ji} + c_j G_{ji} + c_j \delta_{ij}] \\ & + \sum_k J_{ik} [(G_{kk} + |c_k|^2) F_{ij} + (F_{ik} + c_i c_k) G_{kj} + (G_{ik}^* + c_i c_k^*) F_{kj}] \\ & + \sum_k J_{jk} [(G_{kk} + |c_k|^2) F_{ji} + (F_{jk} + c_j c_k) G_{ki} + (G_{jk}^* + c_j c_k^*) F_{ki}] \\ & + J_{ij} (F_{ij} + c_i c_j). \end{aligned} \quad (\text{D.5})$$

$$+ J_{ij} (F_{ij} + c_i c_j). \quad (\text{D.6})$$